The Use of Computed Tomography Images in Monte Carlo Treatment Planning

Magdalena Bazalova

Doctor of Philosophy

Department of Physics

McGill University

Montreal,Quebec

2008-22-08

A thesis submitted to McGill University in partial fulfillment of the requirements of the degree of Doctor of Philosophy.

DEDICATION

To Franta who greatly supported me in Montreal.

ACKNOWLEDGEMENTS

First of all, I would like to acknowledge my supervisor, Dr. Frank Verhaegen. He introduced me to research in medical physics and was an excellent tutor throughout my PhD study. He was always available to discuss my research and to answer all my questions. He taught me how to write scientific papers and enabled me to present my work at international conferences. His corrections of this thesis are greatly appreciated.

I would like to thank to all members of the McGill Medical Physics Unit, especially to the director, Dr. Ervin Podgoršak. After ten years of studying at four universities, his radiation physics course was one of the best classes I ever took. Dr. Podgoršak expressed interest in my research and was available to discuss my future career.

I would like to thank to Dr. Jan Seuntjens, Dr. François DeBlois and Dr. Wamied Abdel-Rahman who always provided help and listened to my concerns. Robin van Gils is thanked for the phantoms he built and Dr. Slobodan Devic for teaching me how to operate a CT scanner. My special thanks goes to the program administrator Margery Knewstubb.

Fabio Cury, MD is thanked for patient related issues and Dr. Gabriela Stroian for contouring organs in the hip prosthesis study. Dr. Lise Roy-Lacroix and Eric Vigneault, MD enabled me to study dual-energy CT with patients. Joe Larkin helped me solve my technical problems. I also appreciate the help from Hatchig Ibisoglu regarding the Picker PQ5000 specifications. I would like to thank to Yves Lammothe

and Paul Klahr from Philips, regarding the ACQSim CT specifications.

I would like to acknowledge various scientists from all over the world for their fruitful discussions, namely Dr. Mehran Yazdi, Dr. Catherine Coolens, Dr. John Roeske, Dr. Jeffrey Williamson and Dr. Jean-François Carrier for their comments on the metal streaking artifact study and the dual-energy CT studies.

I would like to thank all McGill Medical Physics students. Emily H. was there to answer all my questions when I started my project, Emily P. helped me with Matlab and Geneviève with modifications of the EGSnrc/DOSXYZnrc code. Justin, Erika and Danielle answered my numerous English-related questions. Andrew, Arman, Derek and Monica were very supportive of me and my research throughout my entire PhD study.

My PhD study would not have been successful without Franta Kastanek, Chris Furstoss, Joe Perl and Dr. Luc Beaulieu. Franta, a psychologist, helped me to overcome the PhD preliminary exam and made my life in Canada very enjoyable. As a non-physicist, he read my entire thesis and corrected grammatical errors. Chris patiently answered all my brachytherapy questions and helped me with MCNPX dose calculations. His help with the French version of the thesis abstract is appreciated. Joe greatly supported me in my research and introduced me to many other researchers. Luc, the co-author of all my papers, always let me know that my research was relevant. Most importantly, all of the above mentioned listened to me when I needed to be listened to.

The work has been supported by Grant No. 206358 from the Natural Science and Engineering Research Council of Canada (NSERC). The CdTe detector used in

the CT x-ray spectral measurements was acquired with a grant from the Research Institute of the McGill University Health Center. Dr. Frank Verhaegen is a Research Scientist supported by the Fonds de Recherche en Santé du Québec (FRSQ).

Na závěr bych chtěla poděkovat ve svém rodném jazyce rodičům a bratru Davidovi, kteří ve mě vždy věřili a statečně se smířili s tím, že po určitou dobu budu žít za oceánem, šest tisíc kilometrů daleko od Moravské Třebové.

ABSTRACT

Monte Carlo (MC) dose calculations cannot accurately assess the dose delivered to the patient during radiotherapy unless the patient anatomy is well known. This thesis focuses on the conversion of patient computed tomography (CT) images into MC geometry files.

Metal streaking artifacts and their effect on MC dose calculations are first studied. A correction algorithm is applied to artifact-corrupted images and dose errors due to density and tissue mis-assignment are quantified in a phantom and a patient study. The correction algorithm and MC dose calculations for various treatment beams are also investigated using phantoms with real hip prostheses. As a result of this study, we suggest that a metal artifact correction algorithm should be a part of any MC treatment planning. By means of MC simulations, scatter is proven to be a major cause of metal artifacts.

The use of dual-energy CT (DECT) for a novel tissue segmentation scheme is thoroughly investigated. First, MC simulations are used to determine the optimal beam filtration for an accurate DECT material extraction. DECT is then tested on a CT scanner with a phantom and a good agreement in the extraction of two material properties, the relative electron density ρ_e and the effective atomic number Z is found. Compared to the conventional tissue segmentation based on ρ_e-differences, the novel tissue segmentation scheme uses differences in both ρ_e and Z. The phantom study demonstrates that the novel method based on ρ_e and Z information works well and makes MC dose calculations more accurate.

This thesis demonstrates that DECT suppresses streaking artifacts from brachytherapy seeds. Brachytherapy MC dose calculations using single-energy CT images with artifacts and DECT images with suppressed artifacts are performed and the effect of artifact reduction is investigated. The patient and canine DECT studies also show that image noise and object motion are very important factors in DECT. A solution for reduction of motion in DECT is proposed.

In conclusion, this thesis strengthens the link between CT and MC dose calculations by means of artifact reduction and DECT tissue segmentation.

ABRÉGÉ

Les calculs de dose Monte Carlo (MC) ne peuvent précisément déterminer la dose délivrée au patient, à moins de bien connaître son anatomie. Cette thèse se concentre sur la conversion des images tomographiques du patient en fichier de géométrie Monte Carlo.

Les artefacts métalliques et leur effet sur les calculs de dose MC sont étudiés. Un algorithme de correction est appliqué sur les images avec artefacts et les erreurs de dose dues au mauvais assignement des densités et tissus sont quantifiées dans un fantôme et une étude de patient. L'algorithme de correction est aussi testé sur des fantômes avec de réelles prothèses de hanches et l'effet de correction sur les calculs de dose MC est étudié. En tant que résultat de cette étude, nous suggérons qu'un algorithme de correction des artefacts métalliques soit intégré à tout plan de traitement MC. Par le biais de simulations MC, le diffusé est prouvé être une cause majeure des artefacts métalliques.

L'utilisation d'un scanner double énergie pour une méthode novatrice de segmentation de tissu est minutieusement étudiée. Tout d'abord, les simulations MC sont utilisées pour déterminer la filtration optimale de faisceau pour une extraction précise du matériau en scanner double énergie. La méthode à double énergie est ensuite testée sur un scanner avec un fantôme et un bon accord dans l'extraction des propriétés des deux matériaux, la densité électronique relative ρ_e et le nombre effectif atomique Z est trouvé. Comparé à la segmentation conventionnelle des tissus réalisée sur la base des différents ρ_e, la méthode novatrice de segmentation de tissu

utilise les différences entre ρ_e et Z à la fois. L'étude du fantôme démontre que cette méthode basée sur les informations de ρ_e et Z marche bien et rend les calculs MC plus précis.

La thèse démontre que la méthode à double énergie supprime les artefacts métalliques dus aux grains de curiethérapie. Les calculs des dose MC de curiethérapie utilisant des images scanner de simple énergie avec artefacts et des images à double énergie avec suppression d'artefacts sont effectués et l'effet de réduction des artefacts est étudié. L'étude à partir des images de patient et d'images canines obtenues avec le scanner double énergie montre aussi que le bruit des images et le mouvement des objets sont des facteurs très importants avec la technique à double énergie. Une solution pour la réduction du mouvement en scanner double énergie est proposée.

En conclusion, cette thèse améliore le lien entre images CT et les calculs de dose MC par le moyen d'un algorithme de correction d'artefacts et de la méthode novatrice de segmentation.

TABLE OF CONTENTS

LIST OF TABLES

LIST OF FIGURES

STATEMENT OF ORIGINALITY

To the best of my knowledge, the methods, results and conclusions presented in this thesis have not been previously published. Conversion of computed tomography (CT) images into Monte Carlo (MC) geometry files, the main topic of the thesis, was studied by several research groups. However, an extensive study like the one presented here was never conducted.

Many correction methods for streaking artifacts have been developed since the early years of computed tomography (CT). Until now, however, no previous study investigated the effects of the correction algorithms on MC dose calculations. The effect of scatter and beam hardening on metal artifact creation using MC simulations was studied for the first time in this thesis.

MC models of CT x-ray tubes were built in the past, mainly for an accurate assessment of CT dose. These models were mostly validated with half-value layer measurements. A paper published in this thesis is the first to present the validation of a MC CT x-ray tube with the challenging spectral measurements using a CdTe detector.

Dual-energy CT (DECT) material extraction is a well known method for determination of the effective atomic number and relative electron density of a material. However, DECT analysis was done only approximatively using the mean energies of the two CT x-ray beams. A method making use of the full x-ray spectra is proposed here.

Moreover, DECT is used for an improved tissue segmentation for MC dose calculations. This original method for tissue segmentation is proven to work very well and has certainly never been published before.

CONTRIBUTION OF AUTHORS

The thesis consists of five published papers. The manuscripts were written by me, however, help from other co-authors was greatly appreciated.

The work presented in the paper entitled 'Correction of CT artifacts and its influence on Monte Carlo dose calculations' was initiated by Dr. Frank Verhaegen. The work was mainly done by myself, although Steven Palefsky coded the first lines of the artifact correction algorithm. Fruitful discussions with Dr. Luc Beaulieu improved the manuscript that was also reviewed by the other co-authors.

Dr. Luc Beaulieu, Dr. Catherine Coolens and Dr. Peter Childs contributed by discussions to the paper entitled 'Monte Carlo dose calculations for phantoms with hip prostheses'. Dr. Coolens also provided us with the real hip implants. Fabio Cury, MD contoured the hypothetical organs. The manuscript was review by all the co-authors.

The 'Monte Carlo simulation of a computed tomography x-ray tube' study was carried out by myself and my supervisor. Dr. Frank Verhaegen advised me how to take the spectral and half-value layer measurements and carefully revised the manuscript.

The papers entitled 'Tissue segmentation in Monte Carlo treatment planning: a simulation study using dual-energy CT images' and 'Dual-energy CT-based material extraction for tissue segmentation in Monte Carlo dose calculations' were done in collaboration with Dr. Jean-François Carrier and Dr. Luc Beaulieu. Both had previously shortly worked on dual-energy CT and their discussions about the method were an important part of this work. They both reviewed my manuscripts. Dr. Frank

Verhaegen, as my PhD advisor, also carefully reviewed both papers and significantly contributed to the quality of the publications.

CHAPTER 1
Introduction

"When you're diagnosed, I think everything changes."

Lance Armstrong, professional cyclist and cancer survivor

1.1 Cancer and its treatment

Cancer, an uncontrolled growth and spread of abnormal (or tumor) cells, is one of the worldwide leading causes of death [1]. In Canada alone, 73,800 people are estimated to die from cancer and an estimated 166,400 new cancer cases will occur in 2008 [2]. Cancer can affect every organ in the human body. In terms of incidence, the most common cancer types worldwide (excluding non-melanoma skin cancers) are lung, breast and colorectal cancer [3]. According to the World Health Organization, a third of cancer cases worldwide could be cured if detected early and treated adequately [1].

Cancer can be treated with a number of treatment methods out of which three currently prevail: surgery, chemotherapy and radiation therapy. While the goal of surgery is the removal of the tumor (or the entire organ), chemotherapy uses drugs that prevent cancer cells from spreading to other parts of the body. Radiation therapy, on the other hand, uses ionizing radiation to kill cancer cells and shrink tumors.

About half of all cancer patients will receive radiotherapy, either alone or in combination with other treatment modalities, mostly with surgery or chemotherapy [4].

Radiation therapy is delivered in the form of external beam radiation therapy where the tumor is irradiated from an external source (a linear accelerator or linac) and/or brachytherapy where a radiation source is inserted inside or close to the area requiring treatment. External beam radiotherapy is the most frequently used radiotherapy type [4].

1.2 Radiotherapy treatment planning

Radiotherapy uses radiation to kill tumor cells by deposition of energy in the tumor site while sparing surrounding healthy tissue. The energy E deposited by the radiation in a unit mass of tissue m is called the absorbed dose, $D = \mathrm{d}E/\mathrm{d}m$, and is the source of biological response exhibited by the irradiated tissues. The goal of radiotherapy is to deliver a lethal dose prescribed by a physician to the tumor killing the cancer cells while minimally irradiating the healthy tissue and any critical organs. Currently, it is impossible to deliver dose to the tumor alone, therefore in order to minimize dose to healthy tissue, radiotherapy treatment has to be carefully planned and optimized.

A number of radiation types can be used for radiotherapy: photons in the megavoltage (MV), orthovoltage or kilovoltage (kV) ranges, electrons, neutrons, protons or heavier ions. However, 75% of radiotherapy patients are irradiated with photons and 15% of patients receive treatment with electrons. A photograph of a medical linear accelerator used for electron and photon external beam radiotherapy is shown in

figure 1-2.1. Cancer patients are usually irradiated in a prone position from various angles, as specified by the treatment plan.

Figure 1-2.1: A linear accelerator.

1.2.1 Imaging and organ delineation for radiotherapy

In order to plan the dose delivered to a patient accurately, the exact location of the tumor and the patient anatomy have to be determined. Presently, a number of three-dimensional (3D) imaging modalities exist, such as computed tomography (CT), positron-emission tomography (PET) and single photon emission computed tomography (SPECT), ultrasound (US) and magnetic resonance imaging (MRI). While PET and SPECT are mostly used for target localization, US cannot be used for imaging body parts with air/tissue and bone/tissue interfaces. MR images, on the other hand, have a very good contrast, but they are impractical for routine use for radiotherapy planning due to image distortion and long acquisition times. Therefore, CT is currently the choice of imaging technique for radiotherapy treatment planning (figure 1-2.2).

Figure 1-2.2: A CT simulator.

During the treatment planning process, CT images are used by radiation oncologists for tumor contouring and delineation of any organs that need to be spared during the treatment (or organs at risk - OAR). In order to include any invisible microscopical disease in the tumor volume and to account for patient positioning errors and patient motion during the treatment, margins are usually added to the tumor volume and the so called planning target volume (PTV) is created. During the treatment planning phase, the entire PTV is then considered to be the target that needs to be irradiated with a lethal dose that is prescribed by the physician. Maximum allowable absorbed doses to all OARs are also given by the physician. Following this, dosimetrists have to find an optimal treatment plan for each individual patient. This includes the choice of radiation type and beam arrangement so that all dose constraints given by the physician are fulfilled. For this purpose, dosimetrists use computerized treatment planning systems (TPS) employing various dose calculation algorithms that calculate dose distributions according to the beam arrangement given by the dosimetrist.

1.2.2 Beam arrangement and plan evaluation

Treatment planning for radiotherapy is a complex task, as demonstrated in figure 1-2.3 where a treatment plan for a prostate patient using an 18 MV photon beam is shown. Figure 1-2.3a represents the energy absorption of the 18 MV photon beam in water (a tissue substitute) as a function of depth; the percentage depth dose (PDD) curve of the beam is plotted. The maximum energy absorption occurs at about 3.5 cm which makes irradiation of deep-seated tumors difficult. In order to spare healthy tissue, treatment of deep-seated tumors with MV photon beams requires a multiple-beam arrangement, as demonstrated in figure 1-2.3b. Using such a setup, the dose to healthy tissue is spread out around the patient and the tumor volume, the prostate drawn in red, receives the highest dose. The dose to the OAR, the rectum drawn in blue, delivered on the basis of a satisfactory treatment plan should be minimal and certainly within the prescribed limits.

To maximize the dose to the tumor and to minimize the dose to the critical organs, each beam used for treatment has to conform to the shape of the tumor. However, this is sometimes impossible to achieve with the standard linac components, such as collimators, blocks and wedges. In such cases, the challenging intensity modulated radiotherapy (IMRT) technique using multi-leaf collimators (MLC) is preferred [5–7].

Treatment plans are often evaluated using dose volume histograms (DVH). Each point of a cumulative DVH for an organ represents the percentage of the organ volume V receiving at least dose D. Ideally, 100% of the tumor volume receives the lethal dose prescribed by the physician, which is also the maximum dose $D_{\max}$ and any

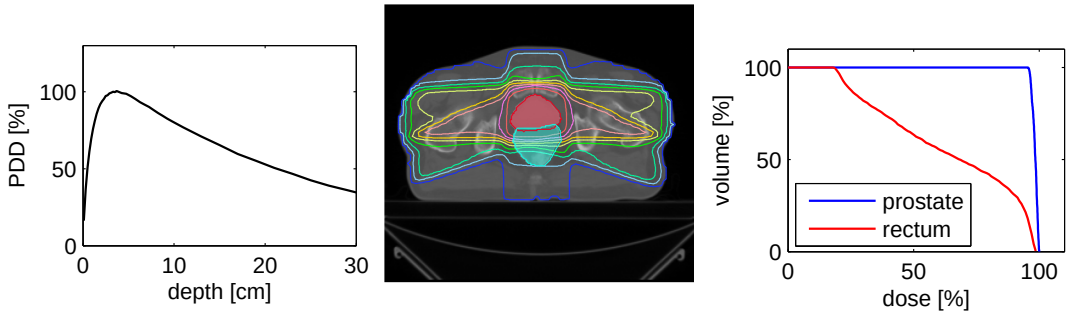

a) b) c)

Figure 1-2.3: The PDD for a typical 18 MV photon beam (a). Dose distribution of a prostate patient calculated for a five 18 MV photon beam setup (b) and DVH for the prostate and rectum (c).

OAR receives zero dose. Unfortunately, this is currently impossible to achieve and a satisfactory plan has to be found during the plan optimization process. A realistic DVH example for the prostate (the PTV) and the rectum (the OAR) calculated for the plan shown in figure 1-2.3b is presented in figure 1-2.3c.

Many researchers attempted to evaluate treatment plans in terms of tumor control probability and treatment related toxicity of normal tissues [8–10]. It has been shown that changes in dose of 7% to 15% can either reduce local tumor control significantly or increase the rate of normal tissue complication [11]. It is believed that planned dose distributions have to conform to the tumor shape as closely as possible and that the dose to the tumor tissue is uniform [12]. It is therefore essential that clinically used treatment planning systems calculate the planned absorbed dose to a patient with a high degree of accuracy.

1.2.3 Dose calculation accuracy

A number of commercial treatment planning systems are available. Each of them calculates the dose to the patient with a different degree of accuracy [13]. Clinical TPS have to be fast and therefore often use approximative calculation methods. However, all TPS should follow the recommendations of the International Commission of Radiation Units and Measurements (ICRU); the accuracy of dose calculation should be within 2% in low dose gradients or within 2 mm spatially in regions with high dose gradients [14]. However, it has been shown that current algorithms and their implementations into commercial treatment planning systems often result in larger deviations [15].

Potentially the most accurate treatment plan can be calculated using the Monte Carlo (MC) method [16–18]. However, MC methods in radiotherapy are relatively challenging because accurate models of linear accelerators and the radiation properties of patient tissues have to be known. Nevertheless, MC-based TPS can take into account tissue inhomogeneities and different tissue properties derived from CT images. The drawback of MC-based TPS is that they are computationally demanding and therefore relatively slow. However, with the fast progress in the field of information technology, in few years the issue of computer speed might be solved. It is believed that accurate MC-based treatment planning systems will be widely used in the future.

MC-based TPS compared to the conventional TPS have their own specifics, such as modeling of the accelerator head, conversion of patient CT images into MC geometry files, the use of variance reduction techniques, etc. Therefore, a thorough

understanding of these aspects of MC-based TPS is essential, especially when MC-based TPS are implemented clinically.

Once a satisfactory treatment plan has been created, it is equally important to accurately deliver the planned dose. Patient positioning errors [19], changes in patient anatomy and tumor shape between treatment planning and the treatment itself [20], tumor motion during treatment [21] and linac calibration [22] are just few examples of factors that influence the accuracy of dose delivery. If serious mistakes are made during radiotherapy treatment, life-threating injuries and patient deaths due to overexposure might occur [23–25].

When treatment plans are correctly calculated and a lethal dose to the tumor is accurately delivered and normal tissue spared, cancer patients might live longer with a better quality of life. Ultimately, radiation therapy can cure cancer and save human lives.

1.3 Thesis objectives

Radiotherapy treatment outcomes are related to the dose received during radiotherapy treatments. As described in the previous section, Monte Carlo (MC) method is potentially the most accurate method for determination of the absorbed dose delivered to patients during radiotherapy. However, this is only true if accurate models of treatment machines are built and accurate patient anatomies are used for dose calculations. The main objective of the thesis is to accurately derive patient anatomies and tissue properties for MC dose calculations which is currently done on the basis of patient CT images.

Chapter 2 of the thesis presents the general background information on CT technology and MC techniques in radiotherapy. Literature review showing the work on the conversion of CT images to MC geometry files done by other research groups is given in chapter 3.

Reduction of CT artifacts, that under certain circumstances appear in CT images, is closely related to MC dose calculations. One of the most severe and relatively frequently occurring type of CT artifacts are metal streaking artifacts. Therefore, a metal artifact correction algorithm and its effect on MC dose calculations is presented in chapter 4. In the same chapter, causes of metal streaking artifacts are studied. The topic of metal artifact correction is further explored in chapter 5 where dose calculations for three common hip prosthesis materials are studied.

Chapter 6 deals with MC simulation of a CT x-ray tube. The simulated x-ray spectra are further used in chapter 7 where the topic of dual-energy CT (DECT) material extraction for MC dose calculations is introduced. The feasibility of DECT material extraction is shown by MC simulations. The effect of DECT on material segmentation for MC dose calculation for an orthovoltage photon beam is presented. DECT material extraction is applied to measured CT images of a tissue-equivalent phantom and MC dose calculations for various treatments beams are studied in chapter 8. The potential improvement of dose calculations for human tissues is also investigated.

Chapter 9 of the thesis focuses on practical aspects of DECT including metal artifact reduction for brachytherapy seeds, patient motion issues and noise in CT

images. Finally, the results of the thesis are summarized and discussed in the last chapter where future work is also proposed.

REFERENCES

[1] World Health Organization. The World Health Organization's Fight Against Cancer: Strategies That Prevent, Cure and Care. Geneva, Switzerland, 2007.

[2] Canadian Cancer Society/National Cancer Institute of Canada. Canadian Cancer Statistics 2008. Toronto, Canada, 2008.

[3] B.W. Stewart and P. Kleihues, editors. *World Cancer Report*. IARCPress, Lyon, France, 2003.

[4] National Cancer Institute. Radiation Therapy for Cancer: Questions and Answers (Fact Sheet 7.1), 2008.

[5] T. Bortfeld. IMRT: a review and preview. *Phys. Med. Biol.*, 51:R363–R379, 2006.

[6] M.J. Zelefsky, Z. Fuks, L. Happersett, H.J. Lee, C.C. Ling, C.M. Burman, M. Hunt, T. Wolfe, ES Venkatraman, A. Jackson, et al. Clinical experience with intensity modulated radiation therapy (IMRT) in prostate cancer. *Radiother. Oncol.*, 55:241–249, 2000.

[7] E.J. Hall and C.S. Wuu. Radiation-induced second cancers: the impact of 3D-CRT and IMRT. *Int. J. Radiat. Oncol. Biol. Phys.*, 56:83–88, 2003.

[8] D.J. Brenner. Dose, volume, and tumor-control predictions in radiotherapy. *Int. J. Radiat. Oncol. Biol. Phys.*, 26:171–9, 1993.

[9] A. Niemierko and M. Goitein. Implementation of a model for estimating tumor control probability for an inhomogeneously irradiated tumor. *Radiother. Oncol.*, 29:140–7, 1993.

[10] W.A. Tomé and J.F. Fowler. On cold spots in tumor subvolumes. *Med. Phys.*, 29:1590–1598, 2002.

[11] A. Dutreix. When and how can we improve precision in radiotherapy? *Radiother. Oncol.*, 2:275–92, 1984.

[12] A. Brahme. Dosimetric Precision Requirements in Radiation Therapy. *Acta Oncol.*, 23:379–391, 1984.

[13] B. Fraass, K. Doppke, M. Hunt, G. Kutcher, G. Starkschall, R. Stern, and J. Van Dyke. American Association of Physicists in Medicine Radiation Therapy Committee Task Group 53: Quality assurance for clinical radiotherapy treatment planning. *Med. Phys.*, 25:1773–1829, 1998.

[14] J. Van Dyk, R.B. Barnett, J.E. Cygler, and P.C. Shragge. Commissioning and quality assurance of treatment planning computers. *Int. J. Radiat. Oncol. Biol. Phys.*, 26:261–73, 1993.

[15] J. Venselaar, H. Welleweerd, and B. Mijnheer. Tolerances for the accuracy of photon beam dose calculations of treatment planning systems. *Radiother. Oncol.*, 60:191–201, 2001.

[16] C.M. Ma, E. Mok, A. Kapur, T. Pawlicki, D. Findley, S. Brain, K. Forster, and A.L. Boyer. Clinical implementation of a Monte Carlo treatment planning system. *Med. Phys.*, 26:2133–2143, 1999.

[17] J.J. DeMarco, T.D. Solberg, and J.B. Smathers. A CT-based Monte Carlo simulation tool for dosimetry planning and analysis. *Med. Phys.*, 25:1–11, 1998.

[18] J.S. Li, T. Pawlicki, J. Deng, S.B. Jiang, E. Mok, and C.M. Ma. Validation of a Monte Carlo dose calculation tool for radiotherapy treatment planning. *Phys.*

Med. Biol, 45:2969–85, 2000.

[19] V. Rudat, M. Flentje, D. Oetzel, M. Menke, W. Schlegel, and M. Wannenmacher. Influence of the positioning error on 3D conformal dose distributions during fractionated radiotherapy. *Radiother. Oncol.*, 33:56–63, 1994.

[20] J.L. Barker, A.S. Garden, K.K. Ang, J.C. O'Daniel, H. Wang, L.E. Court, W.H. Morrison, D.I. Rosenthal, K.S.C. Chao, S.L. Tucker, et al. Quantification of volumetric and geometric changes occurring during fractionated radiotherapy for head-and-neck cancer using an integrated CT/linear accelerator system. *Int. J. Radiat. Oncol. Biol. Phys.*, 59:960–970, 2004.

[21] H. Shirato, Y. Seppenwoolde, K. Kitamura, R. Onimura, and S. Shimizu. Intrafractional tumor motion: lung and liver. *Semin. Radiat. Oncol.*, 14:10–18, 2004.

[22] P.R. Almond, P.J. Biggs, B.M. Coursey, W.F. Hanson, M.S. Huq, R. Nath, and D.W.O. Rogers. AAPMs TG-51 protocol for clinical reference dosimetry of high-energy photon and electron beams. *Med. Phys.*, 26:1847–1870, 1999.

[23] International Atomic Energy Agency. Accidental Overexposure of Radiotherapy Patients in San Jose. Vienna, Austria, 1998.

[24] International Atomic Energy Agency. Investigation of an accidental exposure of radiotherapy patients in Panama. Vienna, Austria, 2001.

[25] C.N. de Oliveira. *Accidental Overexposure of Radiotherapy Patients in Bialystok*. International Atomic Energy Agency, 2004.

CHAPTER 2
Materials and Methods

This chapter gives the general background information concerning the materials and methods used in the thesis which mainly focuses on Monte Carlo dose calculations and their improvements. More specifically, the thesis deals with the transition from patient anatomy defined by computed tomography images into patient geometry data as they are needed for MC dose calculations. Therefore, the introduction to computed tomography with its main principles is presented, followed by the description of Monte Carlo methods in radiotherapy.

2.1 Computed tomography

Computed tomography (CT) is an important tool in diagnostic imaging and cancer therapy. In diagnostic imaging, it is used for anatomical imaging, such as brain imaging (bleeding in the brain, aneurysm, brain tumors and injuries), thorax imaging (lung cancer and emphysema) and abdominal imaging and for functional imaging, such as for cardiac imaging or for multiphase study of the liver. In cancer therapy, which is the subject of this thesis, CT images are used for treatment planning.

The history of CT dates back to 1972 when the first clinical examinations were done by G. N. Hounsfield [1]. However, calculation of the absorption distribution was described earlier by A. M. Cormack [2] on the basis of the mathematical algorithm developed by J. H. Radon [3]. In 1979, the contribution of G. N. Hounsfield and A. M. Cormack to diagnostic imaging was recognized by the Nobel Prize in Medicine.

Currently, CT scanners are compact systems consisting of a CT gantry and a CT table. Typically, an x-ray tube inside the gantry rotates around a patient as the CT table translates through the CT bore. The attenuation of the x-rays within the patient is measured by a detector system which is also located in the gantry. The detector signal is then sent to a reconstruction computer where CT images are reconstructed and displayed [4].

Short overviews of CT history, scanner components and reconstruction techniques are given in the next sections.

2.1.1 CT generations

As the technology advanced, more and more sophisticated CT geometries were developed since the early 1970s. The main goals of each new CT generation were one or more of the following: reduction of scan time, improvement of image quality and reduction of cost. Four CT generations are commonly described, as depicted in figure 2-1.1.

The *first generation* and *second generation* CT scanners (figure 2-1.1a and 2-1.1b) from the early 1970s used very narrow x-ray beams and small detectors and required long image acquisition times. Therefore, these two generations were in clinical use for only a few years.

Technological advances in detection of ionizing radiation in mid 1970s allowed for construction of larger detector systems. This is reflected in the *third generation* CT scanners (figure 2-1.1c) where a large fan beam is detected by a large detector arc. These two rotate simultaneously and therefore the third generation is called the 'rotate/rotate' generation.

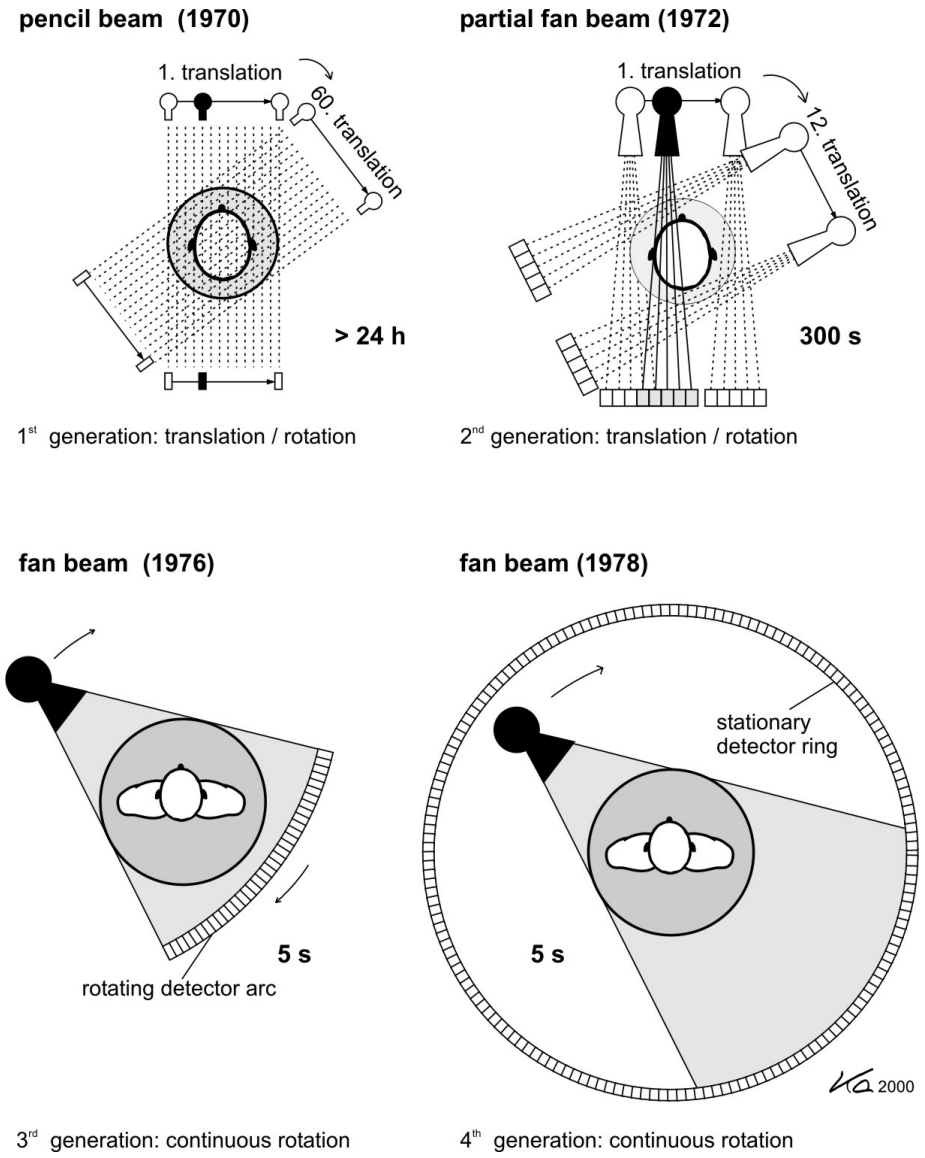

Figure 2-1.1: CT generations [4]

Since the third generation CT scanners require rotation of a bulky system and are also prone to artifacts caused by malfunctioning of even a single detector, *fourth generation* CT scanners (figure 2-1.1d) were developed in the late 1970s. The detector

ring covers 360° and is stationary. This generation is also called the 'rotate only' generation.

Until 1997, all CT scanners were able to acquire only a single CT image during a 360° tube rotation. In 1998, the first four-slice CT systems were introduced which significantly decreased the scan times. Since then, third-generation multi-detector CT (MDCT) scanners are widely used.

2.1.2 CT scanner components

The x-ray tube, the filtration and collimation of the x-ray beam, the compensator (also called the 'bow-tie' filter) and the detector ring form the main components of a CT scanner (figure 2-1.2). These components, specifically designed for the use in a CT scanner, will be briefly described in the following sections.

The CT *x-ray tube* is essentially similar to other diagnostic x-ray tubes. However, it has to operate at high tube voltages, typically between 80–140 kVp, for relatively long scan times (30–60 s) and high current settings (20–400 mA). Large heat capacities of anode discs are therefore required. A new tube design of so called 'rotating envelope vacuum vessel' [5] will allow for a more effective heat dissipation with a reduced x-ray tube mass. Typically, CT scanners offer two focal spot sizes, between 0.5 and 1.2 mm. An example of two CT spectra at 80 and 140 kVp is given in figure 2-1.3a. The characteristic peaks of tungsten can be clearly recognized.

The linear attenuation coefficient for soft tissue as a function of photon energy is plotted in figure 2-1.3b. The graph demonstrates that for diagnostic x-rays, low energy photons are attenuated preferably over high energy photons. This fact results

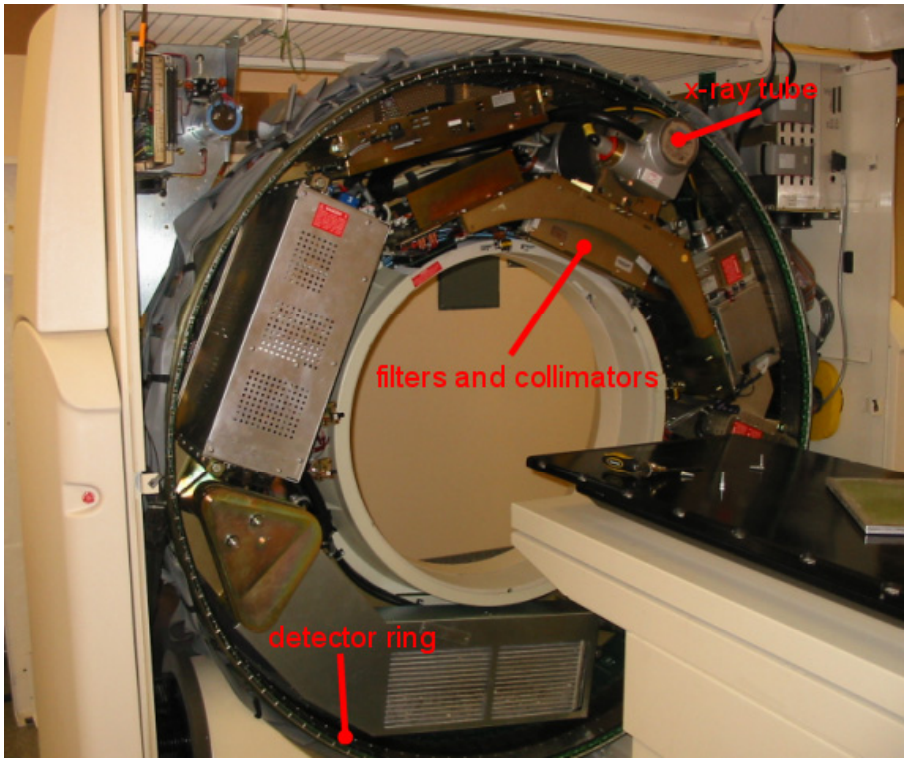

Figure 2-1.2: A fourth-generation ACQSim CT (Philips, Eindhoven, The Netherlands) without the cover.

in so called 'beam hardening' effect. As a polyenergetic beam passes through material, the mean energy of the beam shifts toward high energies (figure 2-1.3c). The shift in the mean energy of the 80 kVp spectrum as the beam passes through 15 and 30 cm of soft tissue is evident. Beam hardening is more pronounced for materials with a high atomic number Z.

The slice thickness, field of view (FOV) and partially beam quality are defined by *collimation and filtration*. The collimators in the direction of the CT table movement (in the z-axis) define the slice thickness, usually between 0.1 and 10 mm. The collimators in the xy plane define the FOV, typically between 6 and 48 cm. The

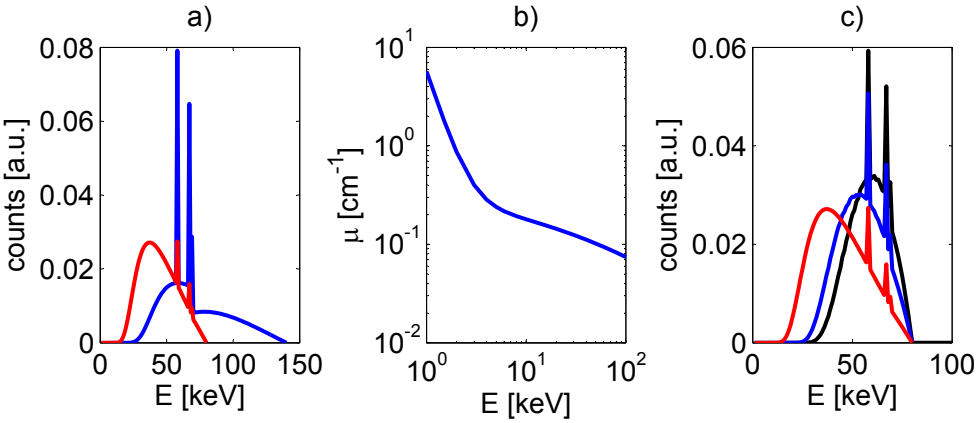

Figure 2-1.3: An example of a CT x-ray spectrum (a) for an 80 kVp beam filtered with a 2 mm thick Al filter (red line) and for a 140 kVp beam filtered with a 10 mm thick Al filter (blue line). The linear attenuation coefficient for soft tissue (b). Beam hardening demonstration (c) for the 80 kVp beam (red line) after it passes through 15 cm (blue line) and 30 cm of soft tissue (black line).

inherent filtration of CT x-ray tubes is not sufficient to filter out photons with low energies that significantly increase the dose to patient but never reach the detector ring and therefore do not contribute to image formation. These low-energy photons are removed by additional flat filters which are usually made of aluminum and 5–10 mm thick.

To ensure a relatively uniform signal at the detector ring, a *compensator* (or bow-tie filter, beam-shaper) is inserted into the beam. It hardly reduces the beam intensity at the center at all but it significantly attenuates the beam at the edges of the compensator. Typically, two compensator sizes are available for body scans and head scans. Compensators are made of low-Z materials minimizing beam hardening.

The *detector ring* is one of the most challenging parts of the entire CT system. Currently, solid state scintillation detectors, such as $CdWO_4$ or CsI, are preferred.

These detectors transform the incident x-ray intensity into a corresponding electrical signal. The signal is then amplified, converted from an analog to a digital signal and transferred to a reconstruction computer. In the next section, the currently used reconstruction technique is briefly described.

2.1.3 Image reconstruction

CT images are matrices of voxels where each voxel is represented by the Hounsfield Units (HU) of the material. The HU definition is the following:

$$\mathrm{HU} = 1000 \left(\frac{\mu}{\mu_{\mathrm{w}}} - 1 \right), \tag{2-1.1}$$

where μ and μ_{w} are the linear attenuation coefficients of a material and water, respectively. However, the quantity directly measured by CT detectors is the intensity of x-rays attenuated by the scanned object, I. If attenuation measurements are taken at many x-ray tube positions, the CT image of the object can be reconstructed.

More specifically, intensity measurements used for reconstruction techniques are stored as the so called sinograms (see figure 2-1.4b). Each point of a sinogram corresponding to the reading of a detector d at a projection angle Θ is defined as:

$$p(d, \Theta) = -\ln I / I_0, \tag{2-1.2}$$

where I and I_0 are the intensity of a ray attenuated by the scanned object and an unattenuated ray, respectively. For an inhomogeneous object represented by a 2D matrix of attenuation coefficients $\mu(x, y)$ scanned with a polyenergetic spectrum of photon energies E between 0 and E_{max}, the intensity I along a particular ray can be expressed as:

$$I = \int_0^{E_{\max}} I_0(E) \cdot e^{-\int_0^d \mu(x,y)\mathrm{d}s} \mathrm{d}E, \tag{2-1.3}$$

where s is the line along the ray. The aim of any reconstruction technique is to find the two dimensional (2D) distribution $\mu(x, y)$ from a certain number of projections $p(d, \Theta)$. The most current CT scanners apply filtered back-projection (FBP) which will be briefly described in the next section[a] .

Filtered back-projection

In filtered back-projection, the measured data are first filtered in order to remove $1/r$ blurring associated with simple back-projection [8]. This can be done by either convolving the raw data with a filter of choice in the spatial domain or by multiplication of the corresponding Fourier transforms in the Fourier domain. The latter is preferred due to the shorter calculation time. Reconstruction computers usually offer various filters, such as the Lak filter, the Shepp-Logan, or the Hamming filter [8] which have more straightforward names in clinical CT scanners, such as 'bone filter' or 'soft filter'. A test tomographic image (the Shepp-Logan head phantom) and its sinogram are presented in figures 2-1.4a and 2-1.4b. The sinogram filtered by the Shepp-Logan filter is shown in figure 2-1.4c.

After the data are filtered, they are uniformly distributed across the image along the projection lines (or back-projected) as demonstrated in figure 2-1.4d. Note

[a] The measured fan beam data have to be either converted to the corresponding parallel beam data [6], as done in the thesis, or a modified version of FBP for fan beam geometry has to be applied [7].

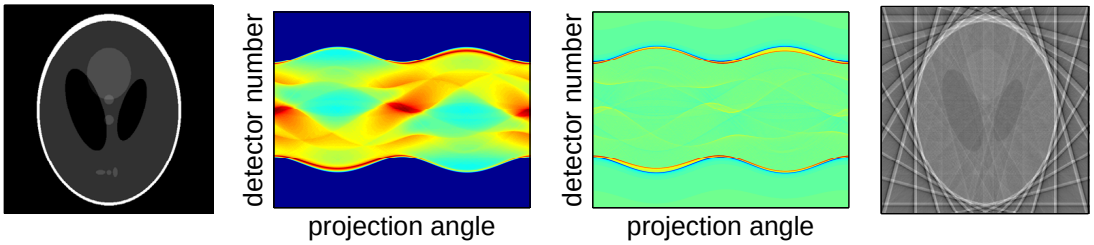

a) b) c) d)

Figure 2-1.4: The Shepp-Logan head phantom (a) with a non-filtered sinogram created from 360 projections over 360°. The same sinogram filtered with the Shepp-Logan filter which is a low-frequency band-pass filter (c) and a back-projected image reconstructed from only 24 projections (d).

that only 24 projections were used for the reconstruction. A number of streaks appear in the image which is due to the filtration in combination with the small number of projection angles. The streaks can be removed by using a larger number of projections, nevertheless, the shape of the head phantom can be seen quite clearly with only 24 projections[b] .

Recent CT scanners reconstruct images from 2400–4800 projections per 360°. The number of readings per projection angle strongly depends on the selected FOV and the number of detectors and their temporal resolution.

CT scanners can operate in an axial mode where the CT table is stationary during the x-ray tube rotation or in a helical (or spiral) mode. In the helical mode, the table moves with a constant speed through the gantry as the x-ray tube spins

[b] Figure 2-1.4 was created with a MATLAB (The Mathworks, Natick, MA) graphical user interface which was developed for teaching purposes of CT image reconstruction.

around the patient. This makes the image acquisition faster, however, an additional step in image reconstruction is needed [8]. Attenuation data have to be interpolated to an arbitrary slice position.

2.1.4 Data storage

CT images are most often stored in so called DICOM (Digital Imaging and Communications in Medicine) file format [9]. The image files consist of a header that contains patient specific information, such as the name of the patient, the date of birth, etc., equipment specific information, such as the scanner manufacturer and the hospital name and image parameters. The image matrix size, bits allocated and stored for each pixel, the slice position and thickness are just examples of image parameters of a DICOM file header.

Usually, the memory allocated for each pixel of a DICOM image is 16 bits. However, these 16 bits are not always used and usually HU are stored only as 12-bit values for further image processing, such as volume rendering. This obviously affects the range of CT numbers that can be stored. If CT images are stored as 12-bit numbers, the HU scale can extend only over 4096 values. Taking into account that the HU of air is -1000, the maximum HU stored as a 12-bit number can then be only 3095. This causes problems when high density objects with HU often larger than 15,000, such as metals, are present in patient bodies. The HU of these objects cannot be retrieved correctly from DICOM files.

If needed, raw data from the scanner can be saved and transferred to a PC for further processing. The raw data file contains detector signals at each x-ray tube position, detector calibration data and air calibration data. The structure and

encoding of raw data files vary significantly between manufacturers. The raw data files are crucial for user-specific image reconstruction as demonstrated in the thesis.

2.2 Monte Carlo dose calculations

In radiation therapy, the absorbed dose delivered to patients during a treatment is the primary physical quantity available for the treatment outcome analysis. Since treatment plans have to be optimized (i.e. the dose calculations have to be re-run) by changing the beam arrangement, clinical dose calculation algorithms have to be relatively fast. They also have to be reasonably accurate, it is believed that the dose should be calculated with a 2% accuracy [10], so that the clinical outcome can be reliably related to the calculated dose distribution. The goal of the modern dose calculation techniques is to find a compromise between 'high accuracy' and 'high speed'.

For an accurate calculation of the dose distribution in a patient, the actual beam used for the treatment and the patient geometry have to be known with a reasonable accuracy. Therefore in general, dose calculations consist of two parts:

- modeling of the linac radiation output,
- transport of energy in the patient geometry.

Depending on the dose calculation algorithm, these two steps are performed at various levels of approximation. Two main approaches for dose calculations are currently in use: *model-based* methods, such as the pencil beam or superposition algorithms and the more sophisticated and accurate *Monte Carlo* method.

This thesis focuses on Monte Carlo dose calculations (MCDC) and therefore more details about Monte Carlo particle transport will be given in the following

sections. It has to be noted, however, that some work done for MCDC might also be applicable to the model-based algorithms, such as the results from the CT artifact reduction studies presented in chapters 4 and 5.

The Monte Carlo (MC) method is any method which solves a problem by generating suitable random numbers and observing that fraction of the numbers obeying some property or properties. The method is useful for obtaining numerical solutions to problems which are too complicated to solve analytically.

In radiotherapy, particle transport in treatment machines and consequent energy deposition in patients (i.e. dose delivery) can be simulated using pseudo-random processes controlled by statistical distributions. A number of validated MC codes have been used in radiotherapy, such as the EGS codes [11, 12], MCNP [13], Geant [14], VMC++ [15] and Penelope [16]. Each of them models the physics of particle transport in a different way and with different accuracies for each particle type and energy. The physics and some of the common features of MC codes in radiotherapy will be described.

2.2.1 Photon and electron transport

Photons with energies encountered in radiotherapy interact with matter via four main processes: coherent (Rayleigh) scattering, photoelectric absorption, incoherent (Compton) scattering and pair-production. In the latter three processes, photon energy is partially or completely transferred to either an electron or an electron-positron pair. Most of the photon interactions cause a significant change in the energy and the direction of the photon.

Electrons undergo a large number of elastic interactions (conserving their energy) when they travel through matter. They lose their energy by two main processes: inelastic collisions with atoms and molecules and radiative interactions. Inelastic collisions are followed by either ionization or excitation. Ionization results in the emission of secondary electrons (or δ electrons) and excitations relax by the emission of gamma rays or Auger electrons, both with characteristic energies. Therefore, photon and electron interactions are often referred to as coupled electron-photon showers.

In MC methods in radiotherapy, particles (e.g. photons which are the subject of our work) are created with a specific position, energy and direction derived from the source definition of the treatment machine. A new position of each particle is determined on the basis of the particle type, energy and the medium through which the particles are transported. The interaction type at the new position is calculated from the interaction probability distribution and a new energy and direction of the photon is determined. If new particles in this interaction are created (such as electrons in Compton effect), their paths are also followed. Eventually, the photons are absorbed by the medium either by photoelectric effect or by pair production. Or, the photon energy is deposited locally and the history is terminated when particles slow down to a certain predefined energy.

This 'event-by-event' particle transport is relatively fast for neutral particles. The energy loss and flight direction change for majority of interactions is significant, therefore, the number of interactions is relatively low and analog simulations are applied. However, charged particles undergo a large number of interactions with a small change in flight direction and for the sake of calculation time, it is not practical

to follow their histories on the 'event-by-event' basis. The so called 'condensed history' (CH) schemes are applied for the transport of charged particles.

Analog simulations

After a photon is sampled from the source distribution, the analog simulation consist of four main steps that are repeated until the particle is locally absorbed or leaves the geometry:

- The distance r to the next interaction is selected. This is calculated using the linear attenuation coefficient μ of the medium at the given photon energy and a random number ξ from the inverval between 0 and 1 by $r = -\frac{\ln(1-\xi)}{\mu}$.
- The particle is transported to the next interaction site taking into account geometry constrains using basic ray tracing.
- The interaction type is selected taking into account the cross-sections of all possible interactions.
- The selected interaction is simulated by sampling energy/direction changes from the differential cross-section of the selected process.

Condensed history simulations

In condensed history simulations, introduced by Berger [17], many 'small-effect' interactions are grouped into relatively few condensed-history steps. Two classes of CH schemes are defined in the paper by Berger. Class I treats electrons with all energies with the CH algorithm. Class II, on the other hand, simulates electrons above a predefined threshold explicitly, i.e. analog simulations are applied. Electrons with an energy above the threshold undergo the so called 'catastrophic' collisions in

which Bremsstrahlung photons and secondary electrons with energies larger than a predefined thresholds are created.

2.2.2 EGS codes

The EGS (Electron-Gamma-Shower) codes (BEAM [18] and DOSXYZnrc [19]) were developed in NRC (National Research Council, Ottawa, ON) on the basis of the EGS4 codes [20] originally written at SLAC (Stanford Linear Accelerator, Stanford, CA). The EGS codes are very popular among radiotherapy researchers and were also used throughout this thesis where photon and electron radiotherapy beams and photon diagnostic beams are simulated.

BEAM

The BEAM code [18] is mainly used for MC simulation of accelerator heads resulting in a distribution of particles at the exit window of a linac. This so called 'phase space' file (phsp) contains the information about the charge (Q), energy (E), position (x, y), direction (u, v, w) and weight (wt) of each particle. In order to calculate the dose delivered to a patient during treatment on a specific linac, the phsp file has to represent the real particle distribution as closely as possible.

The simulation geometry in BEAM is defined by means of component modules (CM). These predefined geometries comprise the standard components of a linac, such as the target, the jaws, the flattening filter, etc. which helps the user to relatively easily define the geometry of any linac. In the thesis, BEAM is used for simulation of a diagnostic CT x-ray tube. The geometry of the simulation consisted of the following CMs: the XTUBE , the SLABs CM for simulation of the inherent filtration and the

JAWS CM defining the FOV and the slice thickness. More details are given in chapter 6.

DOSXYZnrc

Throughout the thesis, unless specified otherwise, dose distributions in phantoms and patients are calculated with the EGSnrc/ DOSXYZnrc code [19]. The simulation geometry and the beam arrangement are entered into the calculation. The phantom/patient 3D voxelized geometries are usually created on the basis of CT images. The absorbed dose per incident particle (history) and the statistical uncertainty of each voxel of the geometry are the outputs of each dose calculation.

In order to define the beam geometry for dose calculations, various source models can be used in the DOSXYZnrc code. Throughout the thesis, the code was used with four different source models: parallel rectangular beam incident from the front for simulation of detector responses; a point source incident from the front and phase-space source incident from any angle for simulations of a CT scanner (chapters 4 and 7) and finally parallel rectangular beam incident from any angle for phantom and patient dose calculations (chapters 4, 5, 7 and 8).

The simulations of the CT scanner were performed in a modified version of the DOSXYZnrc code [21]. In this version of the code, phsp files are rotated by the projection angle and photons undergoing scatter are tagged. Phsp files created by primary and scattered photons can therefore be distinguished. The round detector ring was simulated by curving the phsp plane, i.e. by finding intersections of interpolated photon tracks with the detector ring.

Material definition

Cross-section data for each material used in a simulation have to be created. The PEGS4 stand-alone program is run for each medium of the simulation. The program interpolates the cross-sectional data of the material by means of piecewise linear fits. The elemental composition, the density and a number of parameters have to be set, such as the photon and electron energy cutoffs for the fits, Rayleigh scatter on/off, density effect, etc.

The parameters of the material cross-section file name have to be in agreement with parameters of the actual simulation. For example, if low-energy photon interactions are the subject of a study, Rayleigh scatter should be included in both the simulation and the PEGS4 program. Other parameters that can be switched on during the actual MC simulation are bound Compton scattering and atomic relaxations, e.g.

Calculation time

The MC method in radiotherapy has the advantage that it is the most accurate method to calculate the dose distribution within a patient. However, MC methods are generally very demanding on CPU time, especially if detailed calculations are needed. Various methods to reduce the calculation time without compromising the results can be applied. It has to be noted that any of these techniques have to be first tested to evaluate their effect on the final result of the simulation.

Two parameters that influence the calculation time and have to be set for each simulation are the electron and photon cutoff energies, ECUT and PCUT, respectively. If the total energy of an electron/photon after an interaction falls below

ECUT/PCUT, then the particle's history is terminated and the energy is deposited locally. Depending on the problem, ECUT and PCUT can be set accordingly. For example, for a simulation of an x-ray tube filtered with 11 mm of aluminum, the PCUT can be set to 0.02 MeV because 20 keV photons hardly penetrate the filter at all. ECUT can therefore be set to 0.531 MeV (the cutoff energy includes the rest mass of the electron). On the other hand, if one is interested in detailed dosimetry effects in submillimeter voxels, ECUT and PCUT have to be sufficiently low. In BEAM, ECUT and PCUT can be different for different CMs.

A number of variance reduction techniques can be applied in the EGS codes. One of them, used in the thesis for the simulation of a CT x-ray tube, is the Bremsstrahlung splitting technique. In order to speed up the x-ray tube calculations, directional Bremsstrahlung splitting (DBS) was used. The number of Bremsstrahlung photons was set to 2000, meaning that each Bremsstrahlung process produces 2000 photons with a weight of 1/2000. Photons that are not aimed into a user-defined field are discarded. With DBS, the efficiency of the calculation was increased by a factor of 3000 compared to simulations with no Bremsstrahlung splitting [22].

REFERENCES

[1] G.N. Hounsfield. Computerized transverse axial scanning (tomography). *Brit. J. Radiol.*, 46:1016–1022, 1973.

[2] A.M. Cormack. Representation of a Function by Its Line Integrals, with Some Radiological Applications. *J. Appl. Phys.*, 34:2722–2727, 1963.

[3] J. Radon. On determination of functions by their integral values along certain multiplicities. *Ber. der Sachsische Akademie der Wissenschaften Leipzig (Germany)*, 69:262–277, 1917.

[4] W. Kalender. *Computed Tomography*. Publics Corporate Publishing, Erlangen (Germany), second edition, 2005.

[5] P. Schardt, J. Deuringer, J. Freudenberger, E. Hell, W. Knüpfer, D. Mattern, and M. Schild. New x-ray tube performance in computed tomography by introducing the rotating envelope tube technology. *Med. Phys.*, 31:2699–2706, 2004.

[6] X. Pan. Optimal noise control in and fast reconstruction of fan-beam computed tomography image. *Med. Phys.*, 26:689–697, 1999.

[7] B.K. Horn. Fan-beam reconstruction algorithms. *Proc. IEEE*, 67:1616–1623, 1977.

[8] J.T. Bushberg. *The Essential Physics of Medical Imaging*. Lippincott Williams & Wilkins, 2002.

[9] B. Revet. DICOM Cook Book, for Implementations in Modalities. *Philips Medical Systems, Eindhoven, Netherlands*, 1997.

[10] J. Van Dyk, R.B. Barnett, J.E. Cygler, and P.C. Shragge. Commissioning and quality assurance of treatment planning computers. *Int. J. Radiat. Oncol. Biol. Phys.*, 26:261–73, 1993.

[11] I. Kawrakow and D.W.O. Rogers. The EGSnrc Code System: Monte Carlo simulation of electron and photon transport. *NRCC Report PIRS-701*, 2006.

[12] D.W.O. Rogers, I. Kawrakow, J.P. Seuntjens, and B.R.B. Walters. NRC User Codes for EGSnrc. *NRCC Report PIRS-702 rev B*, 2005.

[13] J.F. Briesmeister et al. MCNP-A General Monte Carlo N-Particle Transport Code, Version 4C. *Los Alamos National Laboratory report LA-12625*, 1997.

[14] S. Agostinelli, J. Allison, K. Amako, J. Apostolakis, H. Araujo, P. Arce, M. Asai, D. Axen, S. Banerjee, G. Barrand, et al. Geant4a simulation toolkit. *Nucl. Instrum. Meth. A*, 506:250–303, 2003.

[15] I. Kawrakow. VMC++, electron and photon Monte Carlo calculations optimized for Radiation Treatment Planning. *Advanced Monte Carlo for Radiation Physics, Particle Transport Simulation and Applications: Proceedings of the Monte Carlo 2000 Meeting Lisbon*, pages 229–236, 2001.

[16] F. Salvat, J.M. Fernandez-Varea, and J. Sempau. PENELOPE, a code system for Monte Carlo simulation of electron and photon transport. *Workshop Proceedings, Issy-les-Moulineaux, France, ISBN*, 2003.

[17] M.J. Berger. Monte Carlo calculation of the penetration and diffusion of fast charged particles. *Methods in Computational Physics*, 1:135–215, 1963.

[18] D.W.O. Rogers, B.A. Faddegon, G.X. Ding, C.M. Ma, J. Wei, and T.R. Mackie. BEAM: A Monte Carlo code to simulate radiotherapy treatment units. *Med.*

Phys., 22:503–524, 1995.

[19] B.R.B. Walters and D.W.O. Rogers. DOSXYZnrc Users Manual. *NRCC Report No. PIRS 794 rev B*, 2007.

[20] W.R. Nelson, H. Hirayama, and D.W.O. Rogers. The EGS4 Code System. *SLAC-265, Stanford Linear Accelerator Center (Dec. 1985)*, 1985.

[21] G. Jarry, S.A. Graham, D.J. Moseley, D.J. Jaffray, J.H. Siewerdsen, and F. Verhaegen. Characterization of scattered radiation in kV CBCT images using Monte Carlo simulations. *Med. Phys.*, 33:4320–4329, 2006.

[22] E. Mainegra-Hing and I. Kawrakow. Efficient x-ray tube simulations. *Med. Phys.*, 33:2683–2690, 2006.

CHAPTER 3
The role of CT images in Monte Carlo dose calculations

The use of CT images for MC dose calculations is presented in this chapter. First, spectral measurements of CT x-ray tubes are described. The quality of CT x-rays directly influences the image quality and is therefore closely related to the conversion of CT images into material properties. Subsequently, the difficulties of the conversion of CT images into MC geometry files are described. An introduction to possible solutions, the main topic of the dissertation, is given. This chapter serves as background information and a literature review for the rest of the thesis which consists mainly of papers published in peer-reviewed journals.

3.1 CT x-ray spectra

Diagnostic CT x-ray tubes produce kilovoltage x-rays by impinging accelerated electrons on a tungsten target. The mean energies of the x-ray spectra vary between 40–100 keV depending on the tube voltage and beam filtration. As mentioned in the previous chapter, beam hardening is an important effect in CT. The effect is one of the causes of image artifacts in CT (see section 3.4) and is usually taken into account in the image reconstruction process on clinical CT scanners. In order to correct for beam hardening and for other quantitative studies in the field of CT, the knowledge of x-ray spectral properties is key.

Spectral measurements of CT x-rays are not a trivial task, mainly due to the high flux of the x-ray tube and the CT scanner geometry. A very small collimator has

to be used for a direct spectral measurement, however, the alignment of the whole system [1] and the collimator choice [2] are crucial.

An alternative approach to measurement of CT x-ray spectra is the reduction of the high photon flux by Compton scatter. The Compton scatter setup for spectral diagnostic x-ray tube measurements was introduced in medical physics by Yaffe *et al.* [3] and used a number of times in the past by other authors [4–7].

Semiconductor detectors are mostly used for spectral measurements of diagnostic x-rays. High purity germanium (HP-Ge) needing a large cooling system [8–10] and more convenient smaller cadmium zinc telluride (CdZnTe) and cadmium telluride (CdTe) [11] detectors are widely used. The disadvantage of these detectors is that their signal has to be corrected for the detector response. This is usually done with the so called 'stripping method' [1, 11, 12].

X-ray spectra can also be calculated by MC simulations. Whereas Boone *et al.* [13], Schmidt and Kalender [14] and DeMarco *et al.* [15] simulated x-ray spectra for estimation of patient dose from CT examinations; other authors extensively studied dose and scattered radiation in cone beam CT (CBCT) using MC simulations [16–18].

Several analytical programs exist that can also be used to estimate spectra from a CT x-ray tube. Usually, the tube voltage, voltage ripple, anode material and angle are entered into these programs. The calculation of x-ray spectra with analytical programs is very fast at the expense of accuracy. Boone and Seibert [19] presented the TASMIP code that uses interpolations to spectra measured by Fewell [20]. Another program, Spektr [21], a computational tool for x-ray spectra production, is also based on TASMIP. Poludniowski and Evans [22, 23] studied penetration characteristics of

electrons into x-ray targets and calculated the Bremsstrahlung and characteristic parts of x-ray spectra[a] .

3.2 CT-to-density conversion

For Monte Carlo treatment planning (MCTP) performed in the commonly used EGSnrc/ DOSXYZnrc code [24], each voxel of patient CT images, acquired prior treatment planning, has to be converted into mass density (ρ) and material type. Since CT images are represented by means of linear attenuation coefficients (μ), this means that μ of each voxel has to be converted into a ρ and a material type. However, there is no direct relationship between μ and ρ for human tissues scanned in kilovoltage CT scanners.

As already mentioned, the mean energy of CT x-ray beams varies between 40–100 keV. In this energy range for human tissues with effective atomic numbers (Z) between 5 and 14, attenuation of x-ray beams consists of a combination of the photoelectric effect, Compton scatter and coherent scatter. Whereas Compton effect and coherent scattering are independent of Z, photoelectric effect depends strongly on Z. Therefore, assignment of ρ to μ is not straightforward.

For megavoltage (MV) CT that makes use of a MV treatment beam for imaging, the problem of assignment ρ to measured μ is overcome [25–27]. This is due to the fact that Compton effect is the dominant interaction type for MV beams which scales with ρ and is Z independent. On the other hand, soft tissue contrast is significantly

[a] An educational graphical user interface for x-ray production based on this method was developed at the Medical Physics Unit of McGill University.

reduced in the MV energy range, therefore MVCT is not very practical for treatment planning.

The commonly used method for conversion of CT images into ρ-maps is done with a (ρ, HU) calibration curve. It is created by scanning a set of tissue-equivalent materials with known ρ which are plotted against the measured HU. The calibration curve consisting of piecewise linear fits to the data is then created. It is important that a suitable set of tissue-equivalent materials for this conversion step is chosen. Moreover, a unique calibration curve has to be created for each CT scanner and each tube voltage [28].

A lot of effort has been done to ensure a correct (ρ, HU) conversion scheme is used. Constantinou *et al.* [28] presented a CT calibration phantom and showed that calibration curves are scanner specific. A stoichiometric calibration using tissue substitutes is presented in the paper by Schneider *et al.* [29] where both the measured HU of tissue substitutes and the chemical composition of real tissues are used to predict HU for human tissues. Later on, Schneider *et al.* [30] simplified the method by introducing interpolation functions into the problem. Elemental weights of human tissues were derived with a reasonable accuracy. An accurate elemental composition was shown to have an effect on electron beam dose calculation results using the EGS4 code [31].

In 1999, Thomas [32] investigated the susceptibility of incorrect ρ assignment on dose calculation results using a simple 1D scaling method for a 6 MV photon beam. Thomas concluded that if no calibration data for a given CT scanner are available

and therefore a default calibration curve is used, no significant dose calculation errors are introduced.

Kanematsu *et al.* [33] proposed a polybinary calibration that approximates body tissues to mixtures of muscle, air, fat and bone and created a calibration curve based on the same principle, constructed from four tissue substitutes - water, air, ethanol and a potassium phosphate solution. More recently, Verhaegen and Devic [34] studied the effect of calibration curves, created with calcium and ethanol solutions, on MC dose calculations. Large dose calculation errors were reported in this paper, up to 10% when the EGSnrc/DOSXYZnrc default CTCREATE [24] calibration curve is used. They also pointed out the unsuitability of Teflon as a calibration material.

A problem of assigning of HU to ρ arises when metallic foreign objects inside human bodies are scanned. Hip prostheses, dental fillings, brachytherapy seeds or surgical clips are just few examples. The fact that CT images are usually stored as 12-bit numbers limits the extent of available HU scale (see section 2.1.4). During the treatment planning stage, correct densities of the metals cannot be assigned on the basis of the limited HU scale and thus the accuracy of dose calculations might be severely affected.

Coolens *et al.* [35] offer a solution to the limited CT scale for hip prosthesis patients by utilization of an extended CT scale. In their paper, the HU are scaled down by a factor of 10 and the HU scale is extended accordingly. Coolens *et al.* concluded that using appropriate windowing and leveling, the dimensions of hip prostheses can be extracted with a reasonable accuracy. The method of downscaling

the HU scale was originally introduced by Klotz *et al.* [36] and later tested by Link *et al.* [37].

3.3 CT-to-material conversion

The conversion of CT numbers into material types is also an important step in MCTP. Usually, a set of material types is assigned to a set of HU ranges. These ranges are defined in a number of ways.

The simplest and in most cases probably the least accurate method to assign materials to HU is the use of the default EGSnrc/DOSXYZnrc CTCREATE subroutine [24]. Many authors used the CTCREATE ramp [38–41] where only 4 tissue types are assigned (air, lung, tissue and bone). Such coarse material segmentation, especially with the default HU ranges, can cause serious dose calculation errors [34].

DuPlessis *et al.* [42] presented a study in which they derived a number of human tissues that are needed for an accurate assessment of dose from an 8 MV photon beam. They concluded that if the dose is to be calculated within 1%, 57 tissue subsets have to be defined with a HU bin width of 30 HU. The percentage depth dose (PDD) curves of the 8 MV photon beam are used to quantify dose differences between various tissue types. DuPlessis *et al.* conclude that a similar study has to be performed for each treatment beam.

A multi-center CT-to-material conversion study was carried out in 2007 and the results were summarized in the paper by Vanderstraeten *et al.* [43]. They show that for a 6 MV photon beam dose calculations, the following tissue segmentation is needed: air, lung, adipose, tissue and 10 bone bins. If the 10 bone bins are combined

into a single bone type, dose errors in bone tissue can be as high as 10% for the 6 MV photon beam.

3.4 CT artifacts

CT artifacts, i.e. any discrepancy between the measured HU and the true attenuation coefficient, can significantly influence image quality. CT artifacts can cause misdiagnosis and patient dose miscalculation if not properly treated. They can be patient, scanner or physics based. Metal streaking artifacts (see figure 3-4.1) are relatively frequently seen due to dental fillings and hip prosthesis and are one of the most severe types of artifacts that cannot be completely avoided.

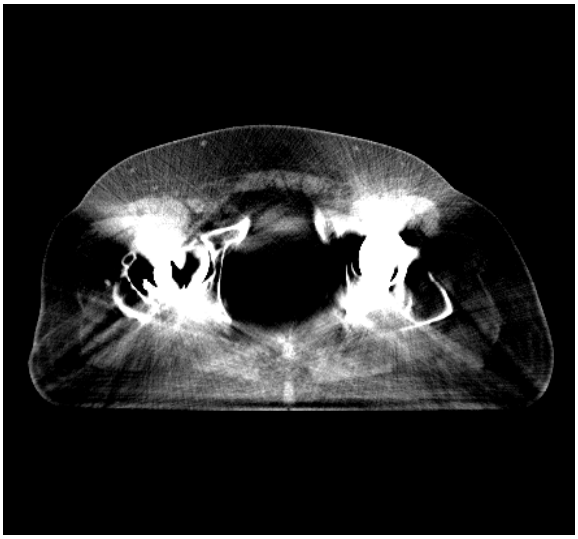

Figure 3-4.1: CT image of pelvis of a prostate patient with bilateral hip prosthesis. Window at 400 HU, level at 50 HU.

In the past two decades, metal artifact reduction (MAR) techniques have been studied extensively. Pawlicki and Ma [44] investigated the effect of metal streaking artifacts on treatment planning for head and neck patients. They used the simplest

approach for metal artifact reduction in which artifact corrupted voxels are identified visually and their CT numbers modified manually.

As early as in 1987, Kalender *et al.* [45] introduced the so called sinogram interpolation method. The method consists of identification of projections pertaining to the high-Z materials causing the artifacts and the consequent filling in of these corrupted projections. In the paper by Kalender *et al.*, the missing projections are defined semiautomatically and linear interpolation for sinogram filling is used. Roeske et al. [46] presented a study in which metal streaking artifacts are corrected by cubic spline interpolation for a phantom and gynecology patients with the Fletcher-Suit metal applicator. Yazdi *et al.* [47] presented a more elaborate approach taking into account the neighboring projections during the interpolation stage.

Hsieh [48] presented an adaptive filtering technique for streaking artifact reduction but he did not apply the algorithm for MAR. Metal streaking artifacts can also be reduced by various iterative algorithms, such as the iterative deblurring [49–52] and the maximum likelihood algorithm [53].

Watzke and Kalender [54] attempted to improve MAR by combining and proper directional weighting of two MAR techniques, linear interpolation of reprojected metal traces and multi-dimensional adaptive filtering of raw data. They concluded that minor new artifacts introduced by the linear interpolation method are diminished when the technique is combined with the adaptive filtering algorithm.

More recently, Bal *et al.* [55] presented a tissue-class model by applying a segmentation of the original image into different material classes using a clustering algorithm. Projections corresponding to the metals are in-painted using a linear

interpolation. Jackowski *et al.* [56] introduced a maximum intensity projection algorithm for cranial CT data to identify a burned person with the use of dental information. Kim and Tomé [57] investigated the effect of metal streaking artifacts and four different MAR techniques on normal tissue complication probability (NTCP) and tumor control probability (TCP) for head and neck patients. They conclude that metal artifacts, especially due to dental fillings, have an impact on the estimates of TCP and NTCP.

3.5 Dual-energy CT

An alternative method for CT-to-density and CT-to-material conversion, extensively investigated in this thesis, is the use of dual-energy CT (DECT). The main concept of DECT is to scan an object with two significantly different x-ray tube voltages, thus obtaining two different attenuation coefficients of each voxel, μ_1 and μ_2. Knowing the properties of the two x-ray spectra and relating the measured μ_1 and μ_2 on the basis of a parameterization of the linear attenuation coefficient, the Z and ρ or the electron density, ρ_e, of each voxel can be calculated. These quantities can then be used for an improved CT-to-density and CT-to-material conversion.

The idea of DECT was independently introduced by two groups in 1976. It was Rutherford *et al.* [58] and Alvarez and Macovski [59] who suggested obtaining two different material properties from two CT scans by the means of splitting the attenuation coefficient into the photoelectric and Compton component. Both groups parameterize μ as a function of energy (E), Z and ρ_e, however, whereas Rutherford *et al.* work in the image domain, Alvarez and Macovski decompose the photoelectric and the Compton attenuation parts directly in the projection space.

After the introduction of DECT, various authors presented their studies in the field of DECT material extraction. Russell *et al.* [60] in their paper conclude that the use of DECT can demonstrate change in brain tissue composition after irradiation with a 4 MeV beam that cannot be quantified by single-energy CT measures. Later on, Heismann *et al.* [61] presented their own algorithm for material extraction using the so called ρZ projection technique.

X-ray tubes in commercial CT scanners produce polychromatic x-rays causing problems in the DECT analysis, such as beam hardening. Some authors use monoenergetic radiation for DECT. While Rizescu *et al.* [62] use a ^{192}Ir source, Torikoshi *et al.* [63] and Tsunoo *et al.* [64] make use of synchrotron radiation. Kirby *et al.* [65] presented a study where they also used synchrotron radiation for DECT material extraction of low-Z materials.

More recently, Williamson *et al.* [66] studied two approaches for the reconstruction of Z and ρ from DECT images - a parametric fit model (PFM) and a basis vector model (BVM) based on the assumption that attenuation coefficients of any biological substance can be approximated by a linear combination of mass attenuation coefficients of two dissimilar basis substances. By means of mathematical simulations they showed that the BVM technique is more promising in realizing DECT material extraction.

If DECT is performed in two consecutive scans, patient motion between the two scans might occur. As a result, the two CT image sets might not be mutually registered and DECT material extraction might not be possible. Therefore, extensive research on patient motion reduction specifically for DECT has been done. Until now,

two main paths have been followed. Siemens (Siemens Medical Solutions, Forchheim, Germany) presented a dual-source CT scanner where two acquisition systems with an angular offset of 90° are mounted onto the rotating gantry [67–69]. Kalender *et al.* [70] and Vetter *et al.* [71], on the other hand, presented a CT scanner with rapid kVp switching. Both techniques make possible to simultaneously scan at two kVp settings and therefore reduce patient motion during DECT scanning.

REFERENCES

[1] S. Miyajima, K. Imagawa, and M. Matsumoto. An alignment method for mammographic X-ray spectroscopy under clinical conditions. *Brit. J. Radiol.*, 75:763–766, 2002.

[2] Y. Kodera, H.P. Chan, and K. Doi. Effect of collimators on the measurement of diagnostic x-ray spectra. *Phys. Med. Biol.*, 28:841–852, 1983.

[3] M. Yaffe, K.W. Taylor, and H.E. Johns. Spectroscopy of diagnostic x rays by a Compton-scatter method. *Med. Phys.*, 3:328–334, 1976.

[4] G. Matscheko and G.A. Carlsson. Compton spectroscopy in the diagnostic X-ray energy range: I. Spectrometer design. *Phys. Med. Biol.*, 34:199–208, 1989.

[5] G. Matscheko and R. Ribberfors. A Compton scattering spectrometer for determining x-ray photon energy spectra. *Phys. Med. Biol.*, 32:577–594, 1987.

[6] G. Matscheko, G.A. Carlsson, and R. Ribberfors. Compton spectroscopy in the diagnostic x-ray energy range. II. Effects of scattering material and energy resolution. *Phys. Med. Biol.*, 34:199–208, 1989.

[7] K. Maeda, M. Matsumoto, and A. Taniguchi. Compton-scattering measurement of diagnostic x-ray spectrum using high-resolution Schottky CdTe detector. *Med. Phys.*, 32:1542–1547, 2005.

[8] M.S. Nogueira, H.C. Mota, and L.L. Campos. (HP) Ge Measurement of spectra for diagnostic X-Ray beams. *Rad. Prot. Dos.*, 111:105–110, 2004.

[9] M. Bhat, J. Pattison, G. Bibbo, and M. Caon. Diagnostic x-ray spectra: A comparison of spectra generated by different computational methods with a measured spectrum. *Med. Phys.*, 25:114–120, 1998.

[10] C.S. Chen, K. Doi, C. Vyborny, H.P. Chan, and G. Holje. Monte Carlo simulation studies of detectors used in the measurement of diagnostic x-ray spectra. *Med. Phys.*, 7:627–635, 1980.

[11] S. Miyajima. Thin CdTe detector in diagnostic x-ray spectroscopy. *Med. Phys.*, 30:771–777, 2003.

[12] S.M. Seltzer. Calculated response of intrinsic germanium detectors to narrow beams of photons with energies up to 300 keV. *Nucl. Instrum. Methods*, 188:133–51, 1981.

[13] J.M. Boone, V.N. Cooper III, W.R. Nemzek, J.P. McGahan, and J.A. Seibert. Monte Carlo assessment of computed tomography dose to tissue adjacent to the scanned volume. *Med. Phys.*, 27:2393–2407, 2000.

[14] B. Schmidt and W.A. Kalender. A fast voxel-based Monte Carlo method for scanner-and patient-specific dose calculations in computed tomography. *Physica Medica*, 18:43–53, 2002.

[15] J.J. DeMarco, C.H. Cagnon, D.D. Cody, D.M. Stevens, C.H. McCollough, J. O'Daniel, and M.F. McNitt-Gray. A Monte Carlo based method to estimate radiation dose from multidetector CT (MDCT): cylindrical and anthropomorphic phantoms. *Phys. Med. Biol.*, 50:3989–4004, 2005.

[16] J.C.L. Chow, M.K.K. Leung, M.K. Islam, B.D. Norrlinger, and D.A. Jaffray. Evaluation of the effect of patient dose from cone beam computed tomography on prostate IMRT using Monte Carlo simulation. *Med. Phys.*, 35:52–60, 2008.

[17] G.X. Ding, D.M. Duggan, and C.W. Coffey. Characteristics of kilovoltage x-ray beams used for cone-beam computed tomography in radiation therapy. *Phys.*

Med. Biol, 52:1595–1615, 2007.

[18] G. Jarry, S.A. Graham, D.J. Moseley, D.J. Jaffray, J.H. Siewerdsen, and F. Verhaegen. Characterization of scattered radiation in kV CBCT images using Monte Carlo simulations. *Med. Phys.*, 33:4320–4329, 2006.

[19] J.M. Boone and J.A. Seibert. An accurate method for computer-generating tungsten anode x-ray spectra from 30 to 140 kV. *Med. Phys.*, 24:1661–1670, 1997.

[20] T.R. Fewell, R.E. Shuping, and K.R. Hawkins. Handbook of Computed Tomography X-Ray Spectra. *NTIS, SPRINGFIELD, VA, 1981, 112*, 1981.

[21] J.H. Siewerdsen, A.M. Waese, D.J. Moseley, S. Richard, and D.A. Jaffray. Spektr: A computational tool for x-ray spectral analysis and imaging system optimization. *Med. Phys.*, 31:3057–3067, 2004.

[22] G.G. Poludniowski and P.M. Evans. Calculation of x-ray spectra emerging from an x-ray tube. Part I. Electron penetration characteristics in x-ray targets. *Med. Phys.*, 34:2164–2174, 2007.

[23] G.G. Poludniowski. Calculation of x-ray spectra emerging from an x-ray tube. Part II. X-ray production and filtration in x-ray targets. *Med. Phys.*, 34:2175–2186, 2007.

[24] B.R.B. Walters and D.W.O. Rogers. DOSXYZnrc Users Manual. *NRCC Report No. PIRS 794 rev B*, 2007.

[25] K.M. Langen, S.L. Meeks, D.O. Poole, T.H. Wagner, T.R. Willoughby, P.A. Kupelian, K.J. Ruchala, J. Haimerl, and G.H. Olivera. The use of megavoltage CT (MVCT) images for dose recomputations. *Phys. Med. Biol.*, 50:4259–76,

2005.

[26] O. Morin, J. Chen, M. Aubin, A. Gillis, J.F. Aubry, S. Bose, H. Chen, M. Descovich, P. Xia, and J. Pouliot. Dose calculation using megavoltage cone-beam CT. *Int. J. Radiat. Oncol. Biol. Phys.*, 67:1201–1210, 2007.

[27] M. Yang, G. Virshup, R. Mohan, C.C. Shaw, X.R. Zhu, and L. Dong. Improving accuracy of electron density measurement in the presence of metallic implants using orthovoltage computed tomography. *Med. Phys.*, 35:1932–1941, 2008.

[28] C. Constantinou, J.C. Harrington, and L.A. DeWerd. An electron density calibration phantom for CT-based treatment planning computers. *Med. Phys.*, 19:325–327, 1992.

[29] U. Schneider, E. Pedroni, and A. Lomax. The calibration of CT Hounsfield units for radiotherapy treatment planning. *Phys. Med. Biol.*, 41:111–124, 1996.

[30] W. Schneider, T. Bortfeld, and W. Schlegel. Correlation between CT numbers and tissue parameters needed for Monte Carlo simulations of clinical dose distributions. *Phys. Med. Biol.*, 45:459–478, 2000.

[31] W.R. Nelson, H. Hirayama, and D.W.O. Rogers. The EGS4 Code System. *SLAC-265, Stanford Linear Accelerator Center (Dec. 1985)*, 1985.

[32] S.J. Thomas. Relative electron density calibration of CT scanners for radiotherapy treatment planning. *Brit. J. Radiol.*, 72:781–786, 1999.

[33] N. Kanematsu, N. Matsufuji, R. Kohno, S. Minohara, and T. Kanai. A CT calibration method based on the polybinary tissue model for radiotherapy treatment planning. *Phys. Med. Biol.*, 48:1053–1064, 2003.

[34] F. Verhaegen and S. Devic. Sensitivity study for CT image use in Monte Carlo treatment planning. *Phys. Med. Biol.*, 50:937–946, 2005.

[35] C. Coolens and P.J. Childs. Calibration of CT Hounsfield units for radiotherapy treatment planning of patients with metallic hip prostheses: the use of the extended CT-scale. *Phys. Med. Biol.*, 48:1591–1603, 2003.

[36] E. Klotz, W. Kalender, R. Sokiranski, and D. Felsenberg. Algorithms for the reduction of CT artefacts caused by metallic implants. *SPIE Conference on Medical Imaging IV: PACS System Design and Evaluation. Part 2*, pages 642–650, 1990.

[37] T.M. Link, W. Berning, S. Scherf, U. Joosten, A. Joist, K. Engelke, and H.E. Daldrup-Link. CT of Metal Implants: Reduction of Artifacts Using an Extended CT Scale Technique. *Journal of Computer Assisted Tomography*, 24:165–172, 2000.

[38] E. Buffard, R. Gschwind, L. Makovicka, and C. David. Monte Carlo calculations of the impact of a hip prosthesis on the dose distribution. *Nucl. Instrum. Meth. B*, 251:9–18, 2006.

[39] T. Knoos, E. Wieslander, L. Cozzi, C. Brink, A. Fogliata, D. Albers, H. Nystrom, and S. Lassen. Comparison of dose calculation algorithms for treatment planning in external photon beam therapy for clinical situations. *Phys. Med. Biol.*, 51:5785–807, 2006.

[40] A.M. Bergman, K. Bush, M.-P. Milette, I. A. Popescu, K. Otto, and C. Duzenli. Direct aperture optimization for IMRT using Monte Carlo generated beamlets. *Med. Phys.*, 33:3666–3679, 2006.

[41] C.M. Ma, E. Mok, A. Kapur, T. Pawlicki, D. Findley, S. Brain, K. Forster, and AL Boyer. Clinical implementation of a Monte Carlo treatment planning system. *Med. Phys.*, 26:2133–2143, 1999.

[42] F.C.P du Plessis, C.A. Willemse, M.G. Lötter, and L. Goedhals. The indirect use of CT numbers to establish material properties needed for Monte Carlo calculation of dose distributions in patients. *Med. Phys.*, 25:1195–1201, 1998.

[43] B. Vanderstraeten, P.W. Chin, M. Fix, A. Leal, G. Mora, N. Reynaert, J. Seco, M. Soukup, E. Spezi, W. De Neve, et al. Conversion of CT numbers into tissue parameters for Monte Carlo dose calculations: a multi-centre study. *Phys. Med. Biol.*, 52:539–562, 2007.

[44] T. Pawlicki and C.M. Ma. Effect of CT Streaking Artifacts in Monte Carlo Dose Distributions for Head and Neck Cancer. *XIII. ICCR Heidelberg Germany*, pages 414–416, 2000.

[45] W.A. Kalender, R. Hebel, and J. Ebersberger. Reduction of CT artifacts caused by metallic implants. *Radiology*, 164:576–577, 1987.

[46] J.C. Roeske, C. Lund, C.A. Pelizzari, X. Pan, and A.J. Mundt. Reduction of computed tomography metal artifacts due to the Fletcher-Suit applicator in gynecology patients receiving intracavitary brachytherapy. *Brachytherapy*, 2:207–214, 2003.

[47] M. Yazdi, L. Gingras, and L. Beaulieu. An adaptive approach to metal artifact reduction in helical computed tomography for radiation therapy treatment planning: experimental and clinical studies. *Int. J. Radiat. Oncol. Biol. Phys.*, 62:1224–1231, 2005.

[48] J. Hsieh. Adaptive streak artifact reduction in computed tomography resulting from excessive x-ray photon noise. *Med. Phys.*, 25:2139–2147, 1998.

[49] D. Xia, J.C. Roeske, L. Yu, C.A. Pelizzari, A.J. Mundt, and X. Pan. A hybrid approach to reducing computed tomography metal artifacts in intracavitary brachytherapy. *Brachytherapy*, 4:18–23, 2005.

[50] D.L. Snyder, T.J. Schultz, and J.A. O'Sullivan. Deblurring subject to nonnegativity constraints. *IEEE T. Signal Process.*, 40:1143–1150, 1992.

[51] G. Wang, D.L. Snyder, J.A. O'Sullivan, and M.W. Vannier. Iterative Deblurring for CT Metal Artifact Reduction. *IEEE T. Med. Imaging*, 15:657–664, 1996.

[52] P.J. Keall, L.B. Chock, R. Jeraj, J.V. Siebers, and R. Mohan. Image reconstruction and the effect on dose calculation for hip prostheses. *Med. Dos.*, 28:113–117, 2003.

[53] B. De Man, J. Nuyts, P. Dupont, G. Marchal, and P. Suetens. An Iterative Maximum-Likelihood Polychromatic Algorithm for CT. *IEEE T. Med. Imaging*, 20:999–1008, 2001.

[54] O. Watzke and W.A. Kalender. A pragmatic approach to metal artifact reduction in CT: merging of metal artifact reduced images. *Eur. Radiol.*, 14:849–856, 2004.

[55] M. Bal and L. Spies. Metal artifact reduction in CT using tissue-class modeling and adaptive prefiltering. *Med. Phys.*, 33:2852–2859, 2006.

[56] C. Jackowski, E. Aghayev, M. Sonnenschein, R. Dirnhofer, and M.J. Thali. Maximum intensity projection of cranial computed tomography data for dental identification. *International Journal of Legal Medicine*, 120:165–167, 2006.

[57] Y. Kim and W.A. Tomé. On the radiobiological impact of metal artifacts in head-and-neck IMRT in terms of tumor control probability (TCP) and normal tissue complication probability (NTCP). *Medical and Biological Engineering and Computing*, 45:1045–1051, 2007.

[58] R.A. Rutherford, B.R. Pullan, and I. Isherwood. Measurement of Effective Atomic Number and Electron Density Using an EMI Scanner. *Neuroradiology*, 11:15–21, 1976.

[59] R.E. Alvarez and A. Macovski. Energy-selective reconstructions in X-ray computerised tomography. *Phys. Med. Biol.*, 21:733–744, 1976.

[60] L.B. Russell, J.R. Fike, C.E. Cann, and C. Süsskind. Dual energy CT scanning for analysis of brain damage due to X-irradiation. *Annals of Biomedical Engineering*, 12:15–28, 1984.

[61] B.J. Heismann, J. Leppert, and K. Stierstorfer. Density and atomic number measurements with spectral x-ray attenuation method. *J. Appl. Phys.*, 94:2073–2079, 2003.

[62] C. Rizescu, C. Beşliu, and A. Jipa. Determination of local density and effective atomic number by the dual-energy computerized tomography method with the ^{192}Ir radioisotope. *Nucl. Instrum. Meth. A*, 465:584–599, 2001.

[63] M. Torikoshi, T. Tsunoo, M. Sasaki, M. Endo, Y. Noda, Y. Ohno, T. Kohno, K. Hyodo, K. Uesugi, and N. Yagi. Electron density measurement with dual-energy x-ray CT using synchrotron radiation. *Phys. Med. Biol.*, 48:673–685, 2003.

[64] T. Tsunoo, M. Torikoshi, Y. Ohno, M. Endo, M. Natsuhori, T. Kakizaki, N. Yamada, N. Ho, N. Yagi, and K. Uesugi. Measurement of electron density and effective atomic number using dual-energy X-ray CT. *Nuclear Science Symposium Conference Record, 2004 IEEE*, 6, 2004.

[65] B.J. Kirby, J.R. Davis, J.A. Grant, and M.J. Morgan. Extracting material parameters from x-ray attenuation: a CT feasibility study using kilovoltage synchrotron x-rays incident upon low atomic number absorbers. *Phys. Med. Biol.*, 48:3389–3409, 2003.

[66] J.F. Williamson, S. Li, S. Devic, B.R. Whiting, and F.A. Lerma. On two-parameter models of photon cross sections: Application to dual-energy CT imaging. *Med. Phys.*, 33:4115–4129, 2006.

[67] T.G. Flohr. First performance evaluation of a dual-source CT (DCST) system. *Eur. Radiol.*, 16:256–68, 2006.

[68] T.R.C. Johnson, B. Krauß, M. Sedlmair, M. Grasruck, H. Bruder, D. Morhard, C. Fink, S. Weckbach, M. Lenhard, B. Schmidt, T. Flohr, M.F. Reiser, and C.R. Becker. Material differentiation by dual energy CT: initial experience. *Eur. Radiol.*, 17:1510–1517, 2007.

[69] Y. Kyriakou and W.A. Kalender. Intensity distribution and impact of scatter for dual-source CT. *Phys. Med. Biol.*, 52:6969–6989, 2007.

[70] W.A. Kalender, W.H. Perman, J.R. Vetter, and E. Klotz. Evaluation of a prototype dual-energy computed tomographic apparatus. I. Phantom studies. *Med. Phys.*, 13:334–339, 1986.

[71] J.R. Vetter, W.H. Perman, W.A. Kalender, R.B. Mazess, and J.E. Holden. Evaluation of a prototype dual-energy computed tomographic apparatus. II. Determination of vertebral bone mineral content. *Med. Phys.*, 13:340–343, 1986.

CHAPTER 4
Correction of CT artifacts and its influence on Monte Carlo dose calculations

Currently, the dose delivered to a patient during radiotherapy is determined on the basis of the patient computed tomography (CT) images. In order to calculate the dose accurately, the exact patient anatomy has to be known. However, if the CT images contain artifacts, the interpretation of the patient anatomy might be incorrect. CT artifacts can cause not only misdiagnosis but they can also result in dose calculation errors.

For dose calculation algorithms taking tissue inhomogeneities into account, CT numbers are converted into electron densities. The conversion of incorrect CT numbers due to artifacts might affect dose calculation outcomes. Dose calculation errors depend on the extent of the artifacts, the beam used for treatment and the dose calculation algorithm.

In this chapter, a thorough study on metal streaking artifacts and their impact on Monte Carlo dose calculations is presented. The study, published in *Medical Physics*, describes a sinogram interpolation correction algorithm which is applied on in-house built head and pelvic phantoms and a prostate patient with bilateral hip replacement. The effect of the correction on tissue segmentation and Monte Carlo dose calculations is studied. The effect of material mis-assignment due to artifacts is investigated.

It is important to understand the causes of CT artifacts so that the formation of artifacts is, if at all possible, suppressed or prevented. By using Monte Carlo simulations of a CT scanner, the role of beam hardening and scatter in metal artifact creation is investigated.

Authors: M. Bazalova, S. Palefsky, L.Beaulieu and F. Verhaegen

Published in: *Medical Physics* **34** 2119-2132, 2007

Awarded by: 2007 Sylvia Fedoruk Prize

Abstract

Computed tomography (CT) images of patients having metallic implants or dental fillings exhibit severe streaking artifacts. These artifacts may disallow tumor and organ delineation and compromise dose calculation outcomes in radiotherapy. We used a sinogram interpolation metal streaking artifact correction algorithm on several phantoms of exact-known compositions and on a prostate patient with two hip prostheses. We compared original CT images and artifact-corrected images of both. To evaluate the effect of the artifact correction on dose calculations, we performed Monte Carlo dose calculation in the EGSnrc/DOSXYZnrc code. For the phantoms, we performed calculations in the exact geometry, in the original CT geometry and in the artifact-corrected geometry for photon and electron beams. The maximum errors in 6 MV photon beam dose calculation were found to exceed 25% in original CT images when the standard DOSXYZnrc/CTCREATE calibration is used but less than 2% in artifact-corrected images when an extended calibration is used. The

extended calibration includes an extra calibration point for a metal. The patient dose volume histograms of a hypothetical target irradiated by five 18 MV photon beams in a hypothetical treatment differ significantly in the original CT geometry and in the artifact-corrected geometry. This was found to be mostly due to miss-assignment of tissue voxels to air due to metal artifacts. We also developed a simple Monte Carlo model for a CT scanner and we simulated the contribution of scatter and beam hardening to metal streaking artifacts. We found that whereas beam hardening has a minor effect on metal artifacts, scatter is an important cause of these artifacts.

4.1 Introduction

The aim of cancer radiotherapy is to deliver a prescribed radiation dose to a defined tumor volume while minimizing the damage to the surrounding healthy tissue. An important step in cancer radiotherapy is the treatment planning. It is frequently done on the basis of CT (Computed Tomography) images. CT images are represented by Hounsfield units, defined as HU = $1000(\mu/\mu_{\mathrm{w}}\text{-}1)$, where μ and μ_{w} are the linear attenuation coefficients of a material and water, respectively. During the planning, the tumor and organs at risk are delineated and the dose to these structures and to normal tissue is determined. The treatment plan is then optimized until all dose requirements usually set by a physician are met.

Two approaches to calculate the dose delivered to patients are currently in use. Whereas in conventional treatment planning, the dose is calculated using a model in which patients consist of water (possibly considering electron density), in Monte Carlo Treatment Planning (MCTP), the CT image is segmented into a few materials (e.g. air, tissue, bone) and the dose is calculated taking these media into account.

In the ideal case, the MCTP leads to more accurate dose calculation [1]. However, due to potential artifacts in CT images, inaccuracies in assigning of HU might result in significant dose miscalculation in both treatment planning methods. Due to an additional miss-assignment of media in MCTP, this method can potentially lead to larger dose calculation errors than conventional treatment planning, which is the research topic of this paper.

The origins of CT artifacts, discrepancies between reconstructed HU in CT images and the true attenuation coefficients, are believed to be known [2]. Metal streaking artifacts appear when a high atomic number, high density material is present in a scanned object which might severely degrade image quality. For example, in between two hip prostheses in a patient's body there is practically no information about the patient's geometry which can be detrimental for treatment planning. Bright and dark streaks not only disallow tumor and organ delineation but might also cause dose miscalculation. As a result, there is a strong need to reduce CT artifacts in MCTP due to potential incorrect assignment of media. The purpose of this work is to investigate the effect of metal streaking artifact correction on CT image quality and Monte Carlo (MC) dose calculations.

Streaking artifact correction algorithms have been developing in recent years. The simplest approach that can be used for minor artifacts is to correct for discrepancies in the CT images themselves [3]. The more sophisticated approaches use three main techniques: filtered back-projection (FBP) on a modified sinogram [2–4], filtering techniques [5] and iterative algorithms [6–10].

Filtered back-projection on a modified sinogram artificially fills corrupted segments in sinograms that correspond to projections containing high density materials. Kalender *et al.* [4] used linear interpolation within each projection, while Roeske *et al.* [11] applied a cubic spline fit to correct for artifacts in images containing Fletcher-Suit applicator. Yazdi *et al.* [12] in their recent work also used neighboring projections at different angles to correct for metal artifacts in CT images of patients with hip prostheses.

Iterative algorithms can use different techniques, such as iterative deblurring [6–9] and the maximum likelihood algorithm [10]. Although iterative algorithms usually result in slightly better image quality, they need longer computation time which makes them currently impractical for clinical use.

In this paper, a FBP method on modified raw data is demonstrated that uses cubic interpolation of missing sinogram data. The correction algorithm is used on various cylindrical phantoms and on a prostate patient. The impact of the correction method on Monte Carlo dose calculation for both phantoms and the patient is determined. Moreover, scatter and beam hardening are briefly studied as potential causes to metal streaking artifacts.

4.2 Materials and methods

4.2.1 Scanning protocols and phantoms

A fourth generation single slice Picker PQ5000 CT scanner was used to acquire images of two cylindrical water phantoms (15 cm and 27 cm in diameter) simulating head and pelvis anatomies. The phantoms were scanned in axial mode at 120 kVp and 400 mAs. Both full field and half field sizes of the scanner were used, resulting

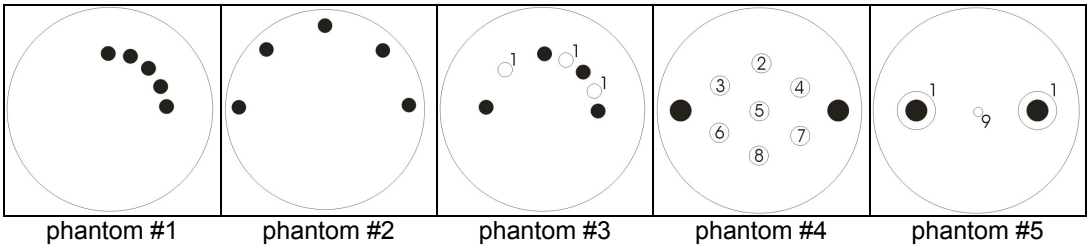

Figure 4-2.1: Schematic overview of three cylindrical head phantoms (#1, #2 and #3, 15 cm in diameter) with small steel cylinders (1.3 cm in diameter) mimicking dental fillings and of two cylindrical pelvic phantoms (#4 and #5, 27 cm in diameter) with large steel cylinders (2.8 cm in diameter) mimicking hip prostheses. The full circles represent steel cylinders, the remaining materials are listed in table 4-2.1.

in 512×512 pixel images. The HU range in the original CT image from the scanner is [-1000, 3095].

The two phantoms were scanned with various inserts, holding steel cylinders mimicking dental fillings or hip prostheses, Teflon cylinders mimicking bone and vials with different in-house made solutions of ethanol and calcium compounds. Steel was chosen as one of three commonly used hip prosthesis materials [13]. In this paper, artifact correction results of five phantoms are presented: phantoms #1, #2 and #3 are head phantoms; phantoms #4 and #5 are pelvic phantoms (figure 4-2.1). Phantoms #1 and #2 are similar phantoms that contain five small steel cylinders to simulate dental fillings positioned either close together or further apart. The small cylinders are placed closer to the phantom surface in phantom #2, so that electron MC dose calculation can be done. Phantom #3 consists of four steel cylinders interleaved by three small Teflon cylinders that mimic teeth.

Table 4-2.1: Composition by fractional weight of Teflon cylinders and solutions used in the phantoms.

			Fraction by weight						
#	Material/solution	ρ(g/cm^3)	H	C	N	O	F	Cl	Ca
1	Teflon	2.200		24.02			75.98		
2	$Ca(NO_3)_2$	1.045	10.41		1.19	86.69			1.71
3	C_2H_5OH	0.931	11.93	19.81		68.26			
4	$CaCl_2$	1.184	8.29			65.78		16.56	9.37
5	C_2H_5OH	0.838	12.66	39.63		47.71			
6	$Ca(ClO_4)_2$	1.119	9.33			82.93		4.94	2.80
7	$CaCl_2$	1.025	10.66			84.58		3.04	1.72
8	C_2H_5OH	0.883	12.30	29.72		57.98			
9	$Ca(ClO_4)_2$	1.692	3.88			65.77		19.39	10.96

Phantom #4 contains two large steel cylinders and seven vials filled with water solutions of ethanol C_2H_5OH, calcium chloride $CaCl_2$, calcium perchlorate $Ca(ClO_4)_2$ and calcium nitrate $Ca(NO_3)_2$ with densities varying from 0.838 g/cm^3 to 1.184 g/cm^3 (table 4-2.1). Phantom #5 consists of two steel cylinders embedded in Teflon cylinders to simulate hip prostheses surrounded by bone. A $Ca(ClO_4)_2$ water solution with density of 1.692 g/cm^3 is placed in the center of the phantom.

In the case of the prostate patient, a helical sinogram consisting of 66 slices was processed and the artifact correction algorithm was applied on 672×672 pixel images. The patient's hip prostheses extended from slice #30 to slice #66.

We developed an algorithm that converts raw data from the scanner into images. To ensure that the procedure works well and reconstructs correct HU, an RMI electron density calibration phantom (figure 4-2.2) was used to test it. The mean HU of 18 materials obtained directly from the scanner and reconstructed by the procedure

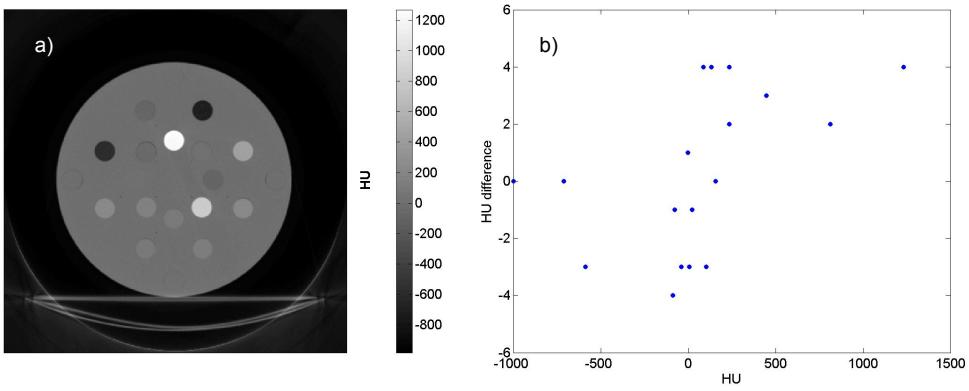

Figure 4-2.2: The RMI electron density calibration phantom (a) and the differences between the mean HU as reconstructed by the CT scanner and by our algorithm for 18 materials.

were compared, the absolute differences for each material are plotted in figure 4-2.2b. The tested HU range extends from -1000 to 1250. The HU were reconstructed accurately within ± 4 HU with our procedure.

4.2.2 Artifact correction algorithm

The artifact reduction algorithm used in this work is based on interpolation of raw sinogram data. The basic steps are identification of the projections corresponding to metals and their interpolation in sinogram space. As a result, the interpolated sinogram is used to obtain an artifact-corrected image. We have developed a Matlab routine to which a fan beam sinogram is the input and an artifact-corrected image is the output.

First, sinograms from a CT scanner are extracted and transferred to a PC where the correction algorithm is performed. The fan beam sinograms are converted into parallel beam sinograms using Fourier analysis [14]. The correction algorithm itself

(figure 4-2.3) is based on work by Roeske *et al.* [11] and Yazdi *et al.* [12] and starts by identifying projections corresponding to high density voxels. For this purpose, filtered back-projection of the parallel beam sinogram is performed resulting in an original image containing artifacts produced by metals. The HU scale of the original image reconstructed from the sinogram is unlimited as opposed to the original image from the CT scanner with the maximum HU of 3095. The voxels corresponding to metals are detected by a fixed threshold in the original image. The threshold has been tested on various geometries and it has been established to be 3800 HU for our scanning protocol. A new image of only high density voxels - a metal only image - is produced. Its forward Radon transform defines a mask for the original sinogram and consequently the missing projections over which an interpolation has to be applied. The masked sinogram in which the interpolation is performed is created by applying the mask to the original sinogram. The cubic spline interpolation is done at each projection angle of the masked sinogram as follows. First, the missing projections are found. To make sure interpolated data will be consistent, two neighboring projection values of the same projection angle on both sides of the missing projections are taken into account. The cubic spline fit is performed on the basis of the four neighboring projections at every projection angle and hence the interpolated sinogram is created. FBP of the modified sinogram produces an artifact-corrected image not containing metals, because their projections have been replaced by the interpolation. The final artifact-corrected image is created by superposition of the metal-only image on the corrected image without metals.

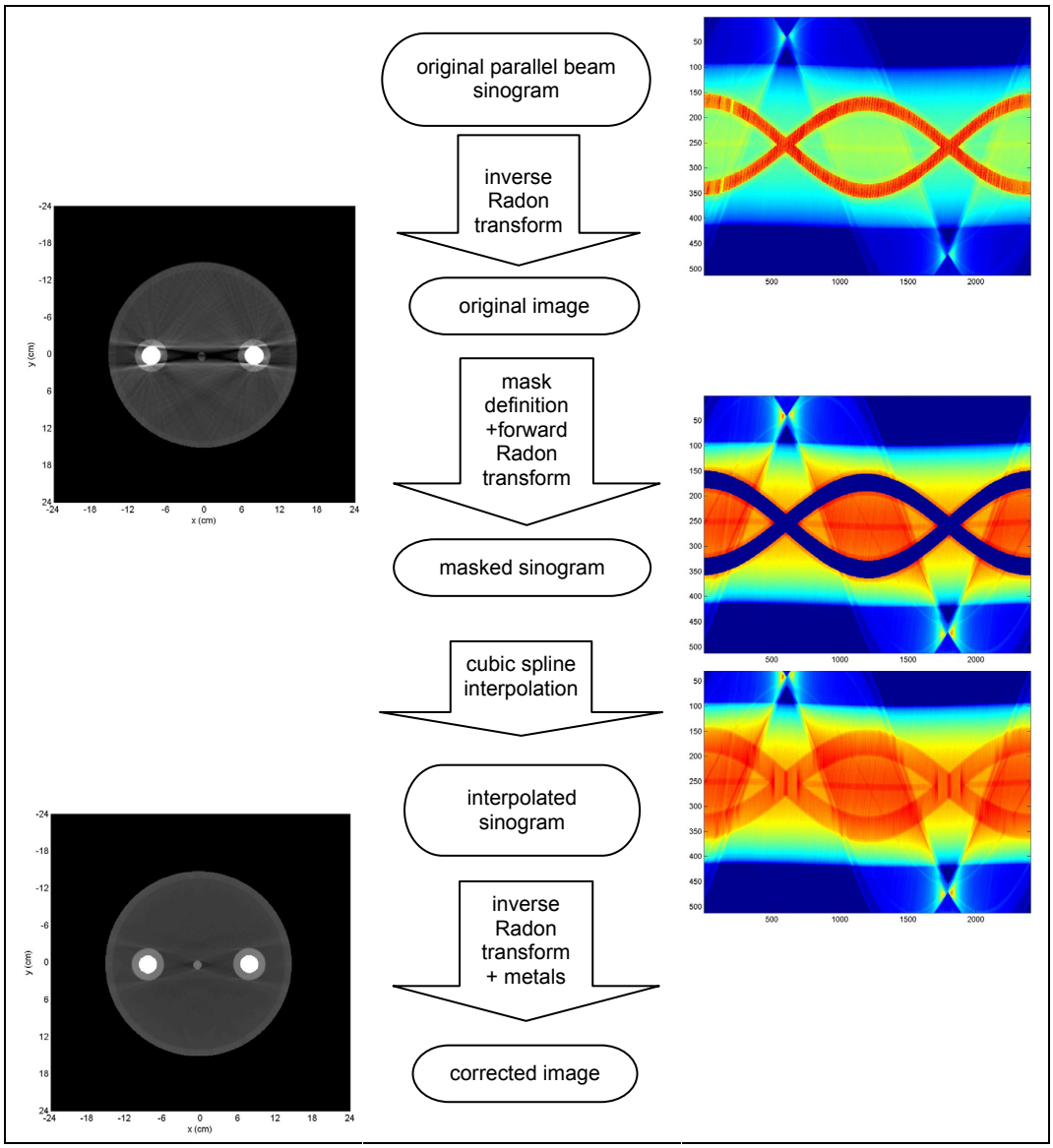

Figure 4-2.3: Flow chart of metal artifact correction algorithm.

4.2.3 MC dose calculation and extended calibration

The influence of the metal artifact reduction method on MC dose calculation was examined with the EGSnrc/DOSXYZnrc code [15] in a set of beam geometries. The original and corrected images were converted into mass densities and segmented into materials according to the standard DOSXYZnrc/CTCREATE calibration which uses four materials: air, lung, tissue and bone. It is common practice to use four materials for MC dose calculation. Several authors use the exact CTCREATE ramp with the default HU and density limits [16, 17], while others [1, 18–20] keep the four media and slightly modify the HU and density limits. Some authors segment CT images into less than four materials for MC dose calculations [21–24]. Du Plessis *et al.* [25] segment CT images into 7 materials and Schneider *et al.* [26] into 71 materials for MC dose calculations, however, this approach is rare. In our work, we have used the HU and density limits given by the DOSXYZnrc/CTCREATE ramp. Since we knew there was no lung in the phantoms or the patient, the lung calibration point was excluded from our conversion.

We have noticed an important issue in our Monte Carlo simulations using the CTCREATE calibration. It was found that in the presence of foreign metal objects, an extra calibration point for a metal must be added to the standard DOSXYZnrc calibration in order to obtain agreement between exact geometry MC dose calculations and dose calculations based on CT image geometry. The limited HU scale [27] of our CT scanner with a maximum value of 3095 together with the present calibration makes it impossible to retrieve densities higher than $2.664\,\mathrm{g/cm^3}$. In comparison, the density of steel is $8.055\,\mathrm{g/cm^3}$. Since there is no bone in the human body that

Table 4-2.2: HU and mass density (ρ) intervals used for conversion of HU into densities and materials for MC dose calculations. Steel is the added calibration point compared to the standard DOSXYZnrc calibration.

Material	HUinterval	ρ interval
Air	[-1000 : -950]	[0.001 : 0.044]
Water/Tissue	[-950 : 125]	[0.044 : 1.101]
ICRP cortical bone	[125 : 2000]	[1.101 : 2.088]
Steel	**3095**	**8.055**

has a HU of 3095 in the energy range of typical CT x-ray tubes, in our calibration, all voxels with 3095 HU are set to steel with density of $8.055\,\mathrm{g/cm^3}$. We denote the calibration as an extended calibration (table 4-2.2). For phantom dose calculations, the second segment of the calibration curve corresponds to water, whereas in the patient study, ICRU tissue is used for the same HU interval.

In our work, we have found that omitting the extended calibration in the presence of metals leads to large dose calculation errors. All dose calculation results in this paper were obtained with the extended calibration, unless stated otherwise.

In phantoms, the dose was calculated in original and corrected CT images in a set of beam arrangements. 6 MV and 18 MV broad polyenergetic photon beams (four field box, two parallel opposed beams) and a single 18 MeV broad polyenergetic electron beam were used for dose calculations; the spectra were taken from Mohan *et al.* [28]. The isocenter was placed in the center of the phantoms in all MC simulations. Since we acquired single slice images in our phantom study, we used the reciprocity theorem [29] to score dose in the phantoms. We created the 3D phantoms by adding a 10 cm z-dimension to the 2D slices. In addition to that, we used 1 cm thick beams perpendicular to the z-axis to make sure all laterally

scattered electrons were captured within the phantom. As a result, the voxel sizes for head phantom calculations were $(0.47\times0.47\times100)\,\mathrm{mm}^3$ and for pelvic phantoms $(0.94\times0.94\times100)\,\mathrm{mm}^3$ and all beams were then of 1 cm length in the z-axis and of varying width in the perpendicular direction.

The 6 MV photon beam used in phantom #1 was 8 cm wide, the 18 MV photon beams were used in the pelvic phantoms and were 10 cm wide. The 8 cm 18 MeV electron beam was simulated at an angle of 315° in phantom #2. The dose distributions were then compared to exact geometry dose calculations.

To quantify the dose differences, a target has been delineated in all phantoms. Dose calculation results of phantoms #1, #4 and #5 are analyzed by the mean errors of a cylindrical target placed in the center of the phantom. The electron dose distributions in phantom #2 are compared by means of dose calculation errors in an ellipsoidal target.

For the prostate patient, a hypothetical five 18 MV photon beam (0°, 90°, 270°, 110° and 250°) treatment was simulated in the DOSXYZnrc code. The photon beam size was $7\times7\,\mathrm{cm}^2$ and the isocenter was placed in the center of the prostate. The 90° and 270° beams were shot straight through the prostheses. It has to be noted that this technique is rather theoretical and treating straight through both prostheses should be avoided. Nevertheless, it is very difficult to avoid the prostheses totally with the five beam technique that is used in our hospital. A hypothetical target in the shape of an ellipsoid was delineated around the prostate. The target was 6 cm long with a semimajor and a semiminor axis of 3 cm and 2 cm respectively, defining a volume of $50\,\mathrm{cm}^3$. The voxel size for patient dose calculation was defined by the

scan parameters to be $(0.744 \times 0.744 \times 4.25)\,\mathrm{mm}^3$. Although it was not known what the hip prostheses were made of, for the MC dose calculation the metallic material was set to steel for this hypothetical case. The results of the original CT geometry and the artifact-corrected geometry were compared by dose distributions and dose volume histograms (DVH) of the target. Exact dose calculations for the patient were not possible.

All Monte Carlo dose calculations presented have statistical errors less than 0.5% in high dose regions.

4.2.4 MC simulation of sources of metal streaking artifacts

Although origins of artifacts are mostly known, discussion on causes of metal streaking artifacts is still an issue. De Man *et al.* [30] and Williamson *et al.* [31] using mathematical simulations show that beam hardening, scatter and noise are the dominant causes of metal streaking artifacts. In this study, we used the Monte Carlo method to simulate a CT scanner and evaluated the effect of scatter and beam hardening on the metal streaking artifacts. We produced sinograms of a phantom by modifying the DOSXYZnrc code such that it is possible to track scattered particles and save them in a separate sinogram.

A schematic view of the simulation geometry is shown in figure 4-2.4. The phantom was a cylindrical phantom filled with water and containing two small steel cylinders. The source of x-rays in our simulation is a phase-space file created by the MC simulation of a CT scanner using the BEAMnrc code [32]. We used two types of x-rays: a polyenergetic x-ray beam that is used in real CT scanners and a mono-energetic x-ray beam that can be used for evaluation of beam hardening on streaking

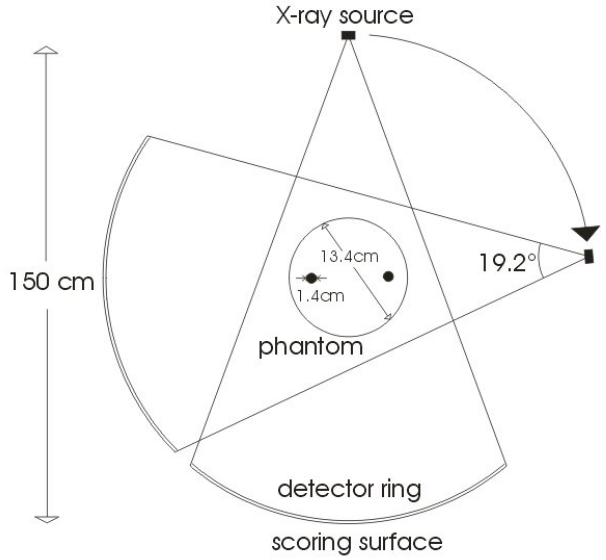

Figure 4-2.4: Schematic view of the geometry for the scatter study. The full circles are steel cylinders.

artifacts. The polyenergetic spectrum was obtained by simulation of an x-ray tube with 120 keV electrons striking a tungsten target that was simulated according to manufacturer's specifications. The spectrum was validated by HVL measurements and spectral measurements taken with a high resolution Schottky CdTe detector (XR-100T, AMPTEK Inc, Bedford, MA). A simple model for our single slice Picker PQ5000 CT was developed by adding two collimators that shape the beam to a 19.6° fan beam with a width of 1 cm at the detector ring. Identical collimation was used for the monoenergetic x-ray beam.

The source of x-rays rotated in 1° steps about the CT scanner isocenter which was placed in the center of the phantom. The x-ray source irradiated the phantom

from 200 positions, because the minimal data set for image reconstruction in our fan beam geometry requires a 200° rotation [33].

The detector ring consists of 128 $CdWO_4$ detectors. Their response to x-rays in energy range of our interest was simulated in the DOSXYZnrc code by calculating the dose deposited in $(29\times4\times0.945)\,\mathrm{mm}^3$ $CdWO_4$ crystals. Put another way, when a photon trajectory intersects the detector ring, its energy is convolved with the energy response of the detector crystals and the resulting signal is stored in the corresponding detector. In this way, an intensity map is created consisting of 128 detector readings at 200 projection angles.

A sinogram is a 2D map of projections $p = -\ln(I/I_0)$, where I is the intensity at the detector ring in the presence of attenuating object and I_0 is the source intensity at the detector ring. The source intensity map is simulated with no phantom. Subsequently a 200° sinogram is obtained. The sinogram is then completed in Matlab to a 360° sinogram, converted into a parallel beam sinogram [14] and reconstructed.

In a CT scanner, the x-rays pass through a patient toward the detector ring and the attenuated photons generate a signal for image reconstruction. The reconstruction process (FBP) assumes that the detector signal consists of only primary attenuated photons. However, this is not the case in real CT scanners. There is a certain amount of scattered photons that reach the detector and their signal is incorrectly taken into account in the FBP. The scattered photon signal is negligible when scanning low density objects but it plays an important role when a high density material is present in the scanned object. Since the attenuation of x-rays in thick

high density materials is excessive, the signal in the shadow of these materials consists almost entirely of the scattered photons. This is a part of the detector-model mismatch introduced by Williamson *et al.* [31].

In our MC simulations, it is possible to track all interactions the x-rays undergo, including the scatter. All the scattered photons were tagged and two different sinograms have been produced: a primary sinogram of primary photons and a sinogram of the tagged scattered photons. The total sinogram that the real CT scanners use is obtained by their summation. The effect of scattered photons on metal streaking artifacts is studied by comparison of two images: the original image reconstructed from the total sinogram and the scatter-free image that is obtained by a FBP of the primary sinogram.

The reconstruction algorithm also assumes that each voxel is represented by a constant, the linear attenuation coefficient of the voxel material. However, low energy photons of a polyenergetic spectrum are attenuated more easily than the high energy photons, which results in a higher effective beam energy as the beam passes through material. Consequently, the attenuation in every voxel is dependent on the mean beam energy at its position, which makes it difficult to assign a single value of the linear attenuation coefficient to that voxel. To investigate the effect of beam hardening, we simulated an x-ray tube with a single energy so that the beam cannot get harder and a single attenuation value to each voxel can be assigned. We used the energy of 75 keV which is approximately the mean energy of a common 120 kVp CT spectra. In this setup, we produced and processed a total and a primary sinogram in order to study the scatter contribution as well.

4.3 Results and discussion

The results are presented in four sections. The first two sections contain phantom images and dose calculations in phantoms and the third part is dedicated to patient MC simulation. The fourth part summarizes the results on the effects of scatter and beam hardening on metal streaking artifacts.

4.3.1 Corrected images

The artifact correction algorithm was used on several cylindrical phantoms and their results are presented in figure 4-3.5. Comparison of the first and the second columns that contain original CT and artifact-corrected images clearly demonstrates an improvement in image quality. Phantom #1 is a head phantom in which artifacts are produced by steel cylinders that mimic tooth fillings. Phantom #3 also contains three small Teflon cylinders that are placed between fillings and are poorly visible in the original image. The correction algorithm cleans up the large artifacts and the Teflon cylinders can be distinguished.

The pelvic phantoms (#4 and #5) are more complex with major artifacts that severely influence the image. The original CT image of phantom #4 does not display the central vial with density of $0.838\,\mathrm{g/cm^3}$. However, the vial is completely visible in the artifact-corrected image. Phantom #5 demonstrates the ability of the algorithm to distinguish between bone (Teflon) and metal; it validates the metal threshold choice. Due to artifacts, more voxels than just the steel cylinders have the maximum HU (3095) in the original image acquired by the CT scanner which makes it impossible to detect high density voxels directly in the original image by setting the threshold to 3095 HU. Nevertheless, after the original sinogram is processed, an

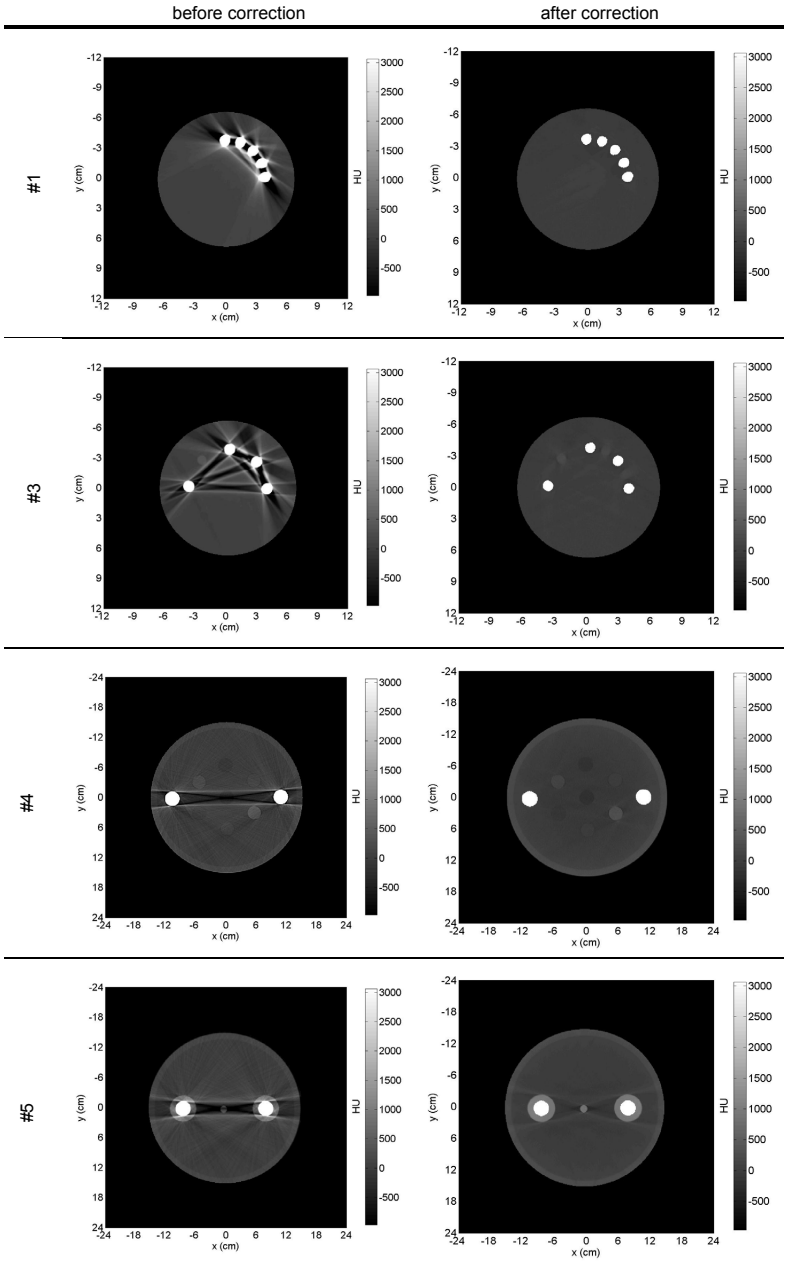

Figure 4-3.5: Original images (first column) and artifact corrected CT images (second column) for phantoms #1, #3, #4 and #5. Phantom is #2 not shown, the results are similar to phantom #1.

unlimited HU scale can be used and a suitable threshold larger than the maximum HU in the CT images for metal detection of the artifact correction algorithm can be found. We have investigated the threshold on various phantoms and we have established it to the value of 3800 HU. The corrected image of phantom #5 shows that the threshold used in the artifact correction algorithm for metal detection can distinguish between higher density materials, such as Teflon and metal.

It should be pointed out that the choice of Teflon as bone equivalent material is not suitable [34]. The presence of fluorine in Teflon gives low HUs compared to bone for the same mass density. Consequently, our calibration curve based on real human tissues is not able to retrieve the density of Teflon ($2.2\,\mathrm{g/cm^3}$) from its relatively low HU (400).

4.3.2 Phantom Monte Carlo dose calculation

The importance of the metal streaking artifact correction algorithm for MCTP is demonstrated by a set of MC dose calculations. We performed dose calculations in the exact phantom geometry (D_{ex}), in original CT geometry (D_{CT}) and in artifact-corrected CT geometry (D_{cor}). In figures 4-3.5, 4-3.7 and 4-3.8, the dose differences (D_{ex} - D_{CT})/D_{ex} and (D_{ex} - D_{cor})/D_{ex} for 6 MV photon beams, an 18 MeV electron beam and 18 MV photon beams are displayed. Hypothetical targets have been delineated in individual dose distributions and their mean and maximum dose calculation errors are summarized in table 4-3.3.

To illustrate the need for the extended calibration, differences in MC dose distributions for two parallel opposed 6 MV beams were evaluated when the extended calibration for HU conversion was not used (results not shown). The significance of

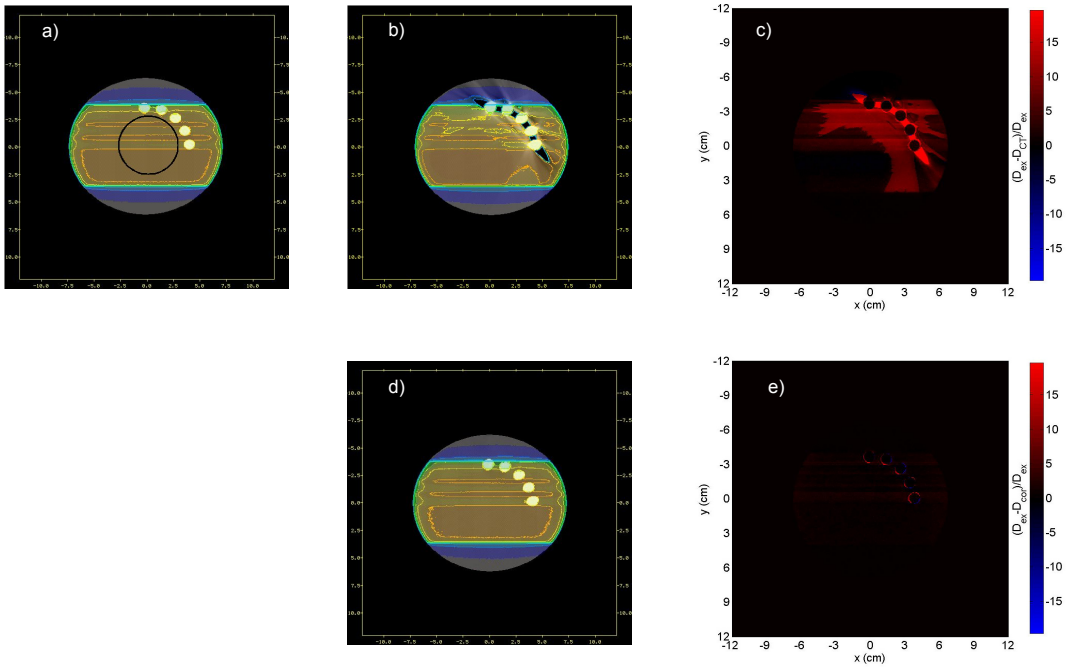

Figure 4-3.6: Monte Carlo dose calculation in phantom #1 for two parallel opposed 6 MV photon beams. Exact geometry dose distribution D_{ex} with a hypothetical target outlined in black (a), original CT-based geometry D_{CT} (b) and artifact corrected geometry D_{cor} (d) dose distributions both with use of the extended calibration. The corresponding dose distribution differences from the exact geometry are presented in (c, e).

the extended calibration can be clarified by comparison of dose calculation errors in the artifact-corrected geometry. Whereas the mean error of the calculation in the target with the standard calibration is 2.6%, it decreases to 0.7% when the extended calibration is used (figure 4-3.6e). To emphasize the influence of the extended calibration, one should note that the maximum error of the target in the artifact-corrected geometry with the extended calibration is only 1.9% whereas without the extended

Table 4-3.3: Percentage mean and maximum errors in dose calculation for different targets of four phantoms (with the extended calibration). Phantom #3 is not listed because of dose differences in Teflon cylinders.

	Ph.#1 (6 MV)		Ph.#2 (18 MeV)		Ph.#4 (18 MV)		Ph.#5 (18 MV)	
	mean	max	mean	max	mean	max	mean	max
original CT image	4.6	13.6	4.3	51.2	3.1	10.6	4.6	43.4
artifact-corrected	0.7	1.9	0.4	1.5	0.6	3.0	3.1	6.9

calibration it is 7.7%. The mean and maximum error of the target in the original geometry (figure 4-3.6c) is 4.6% and 13.6%, respectively.

An important conclusion can be drawn from the presented 6 MV photon dose calculations. The maximum dose calculation errors decreased significantly from more than 25% in the original image without using the extended calibration to less then 2% in the artifact-corrected image with the extended calibration. In other words, only the combination of the artifact correction and the use of the extended calibration provides good dose calculation results. Clearly, the CTCREATE defaults should not be used for treating patients with metal implants. In the rest of the work, only the extended calibration for material and density conversion will be used.

For the purpose of the single 18 MeV electron beam dose calculation, phantom #2 has been constructed with steel cylinders close to its surface (figure 4-3.7). The mean dose errors in the hypothetical ellipsoidal target decreased significantly from 4.3% in the original CT image to 0.4% in the artifact-corrected image.

Two photon beam dose calculations were performed with an 18 MV photon beam on two pelvic phantoms, phantom #4 and phantom #5 (figure 4-3.8). For phantom #4, a four field box beam arrangement was chosen. The mean dose differences in

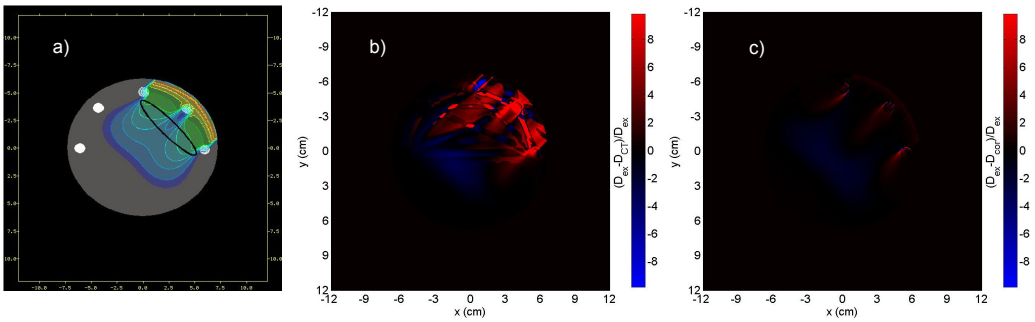

Figure 4-3.7: 18 MeV electron beam dose distribution in a head phantom (phantom #2). Exact geometry (a) and dose calculation errors in original CT (b) and in artifact-corrected (c) geometry.

the target improved significantly from 3.1% in the original CT geometry to 0.6% in the artifact-corrected geometry.

Phantom #5 containing steel cylinders embedded in Teflon was simulated with two parallel opposed beams. Since there are large differences in mass energy absorption coefficients between Teflon and cortical bone (about 10% for a 6 MeV photon), in this case, we used a special approach for material and mass density assignment. We did not want to introduce deliberate dose calculation errors by incorrectly assigning the Teflon voxels to bone, so the material map for both the original CT and corrected geometry MC dose calculation is the exact material map taken from the exact geometry. Only the mass densities were assigned from the actual images according to the extended calibration. There is an improvement in the mean error of the target after artifact correction is done. The error decreases from 4.6% in the original CT image to 3.1% in the artifact-corrected image. Nevertheless, the inability of the calibration to retrieve the correct Teflon mass density prevents to obtain better results. This is

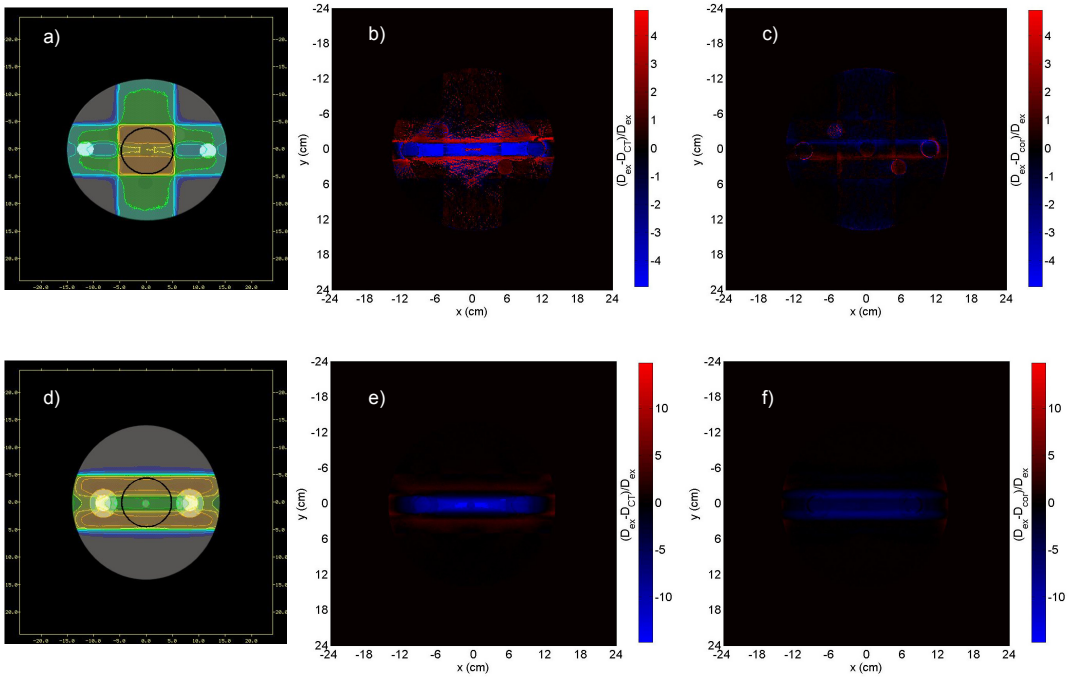

Figure 4-3.8: 18 MV photon beam dose distributions for two pelvic phantoms: phantom #4 (top) and phantom #5 (bottom). Exact geometry dose distribution (a, d) and differences from it in original CT image (b, e) and in metal artifact-corrected image (c, f).

also the reason why MC dose calculation results are not presented for phantom #3 that also exhibits large calculation errors in the Teflon cylinders.

Dose perturbation interface effects due to the presence of high-Z materials are an interesting issue that is usually neglected in commercially available dose algorithms. However, MC codes are able to simulate these effects caused by perturbations of secondary electron fluence [35]. The dose profile through the center of phantom #4 along x-direction is shown in figure 4-3.9. The 18 MV beam four field box dose profile

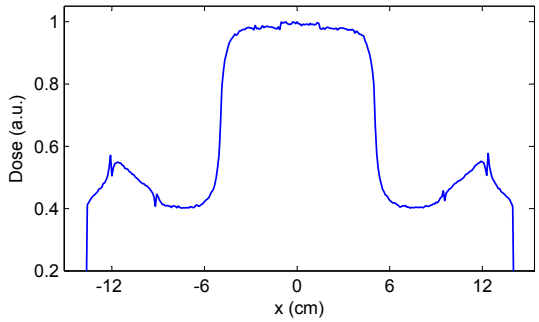

Figure 4-3.9: Dose profile through the dose distribution of figure 4-3.8a ($y = 0\,\text{cm}$). Dose interface effects due to the presence of the steel cylinders are clearly visible (at x = -12, -9, 9 and 12 cm).

clearly shows the dose perturbation at the water/metal interfaces at the position of the two steel cylinders.

4.3.3 Patient study

The metal artifact correction algorithm has been tested on several phantoms with a rather simple geometry. The advantage of this approach is that we can compare dose distributions of original and artifact-corrected images to dose calculations in the exact geometry. The metal streaking artifact correction algorithm has also been used on a prostate patient with bilateral hip prostheses and differences in dose volume histograms (DVH) of a hypothetical target have been evaluated.

The patient study results are summarized in figures 4-3.10 and 4-3.11. The 18 MV photon beam dose distribution in the entire original CT image (figure 4-3.10c) is affected by streaking artifacts that are the most pronounced in the area between the hip prostheses (figure 4-3.10a). The correction algorithm results in a

more correct material segmentation and a smoother dose distribution in the artifact-corrected geometry (figure 4-3.10d). We have also compared DVHs of an ellipsoidal target (outlined in red in figure 4-3.10) in order to quantify differences in the two dose distributions. Since the slice shown in figure 4-3.10 is almost at the edge of the target, the delineated circle appears small.

An additional problem to the metal artifacts was found to arise. Due to incorrect assignment of some artifact influenced voxels to air in the original CT slice (figure 4-3.10b), about 20% of the target receives no dose (figure 4-3.11a). It is common practice in MC dose calculations that the dose to air is set to zero, partly because the voxels filled with air have large calculation errors. Moreover, we are usually not interested in the dose outside the patient, or to air in body cavities. Figure 4-3.11a also shows that the entire target receives more than 80% of the maximum dose and the DVH curve is steeper in the artifact-corrected geometry. Figure 4-3.11b compares the dose distributions shown figure 4-3.10 by plotting the differences between the dose in the original CT slice D_{CT} and the dose in the artifact-corrected slice D_{cor}. The two dose distributions were first normalized to the maximum dose in the artifact-corrected geometry and then subtracted. As expected, the negative dose differences appear in the voxels that have been incorrectly assigned to air in the original CT geometry, because the dose to these voxels is zero in the original geometry. The positive differences can be explained by incorrect assignment of some voxels to bone and subsequently larger energy deposition to bone than to tissue for the 18 MV photon beam. Our conclusion from the patient study is that the DVH curves for the original CT geometry and the corrected CT geometry differ

significantly which is mostly due to the 'zero dose to air' issue. Although the beam angles for our hypothetical MC simulation were taken from real prostate treatments as it is done in our hospital, it would be advisable to avoid the 90° and 270° beams. These should be replaced by beams that do not intersect the prostheses.

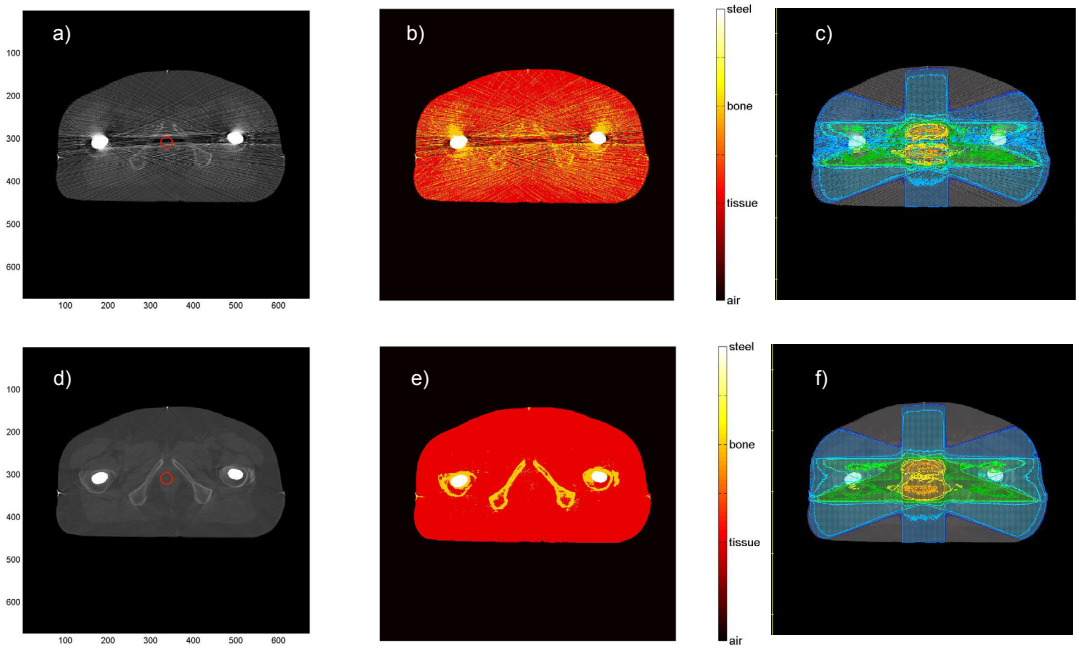

Figure 4-3.10: Original CT image (a) and artifact-corrected image (d) of a prostate patient with an ellipsoidal target delineated. Material segmentation in the original CT image (b) and in the artifact-corrected image (e). Dose distribution in five-field 18 MV photon beam setup in the original CT image (c) and the artifact-corrected image (f).

It has to be noted that metal artifact reduction techniques in general do not produce ideal artifact-free images. While the majority of the artifacts is reduced, some minor artifacts are created, such as these around vial #7 in pelvic phantom

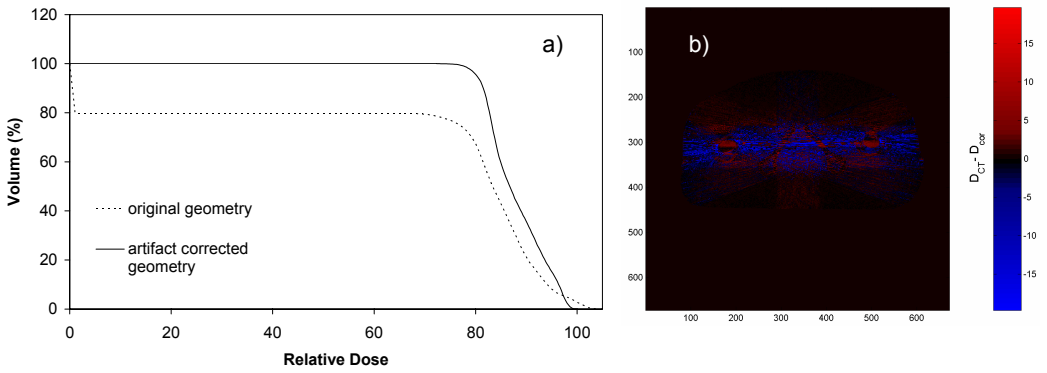

Figure 4-3.11: DVHs for the target in the original CT geometry and in CT artifact-corrected geometry (a) and differences between the original CT geometry D_{CT} and the artifact-corrected geometry D_{cor} dose distributions D_{CT} - D_{cor} (bright blue voxels have differences larger or equal to -20%). The dose is normalized to the maximum dose in the artifact-corrected geometry in both images.

#4 (figure 4-3.5). However, the net benefit for Monte Carlo dose calculations is demonstrated in this paper.

The Task Group 63 reported on Dosimetric consideration for patients with hip prostheses undergoing pelvic irradiation [13]. First, they propose beam arrangements that partly or completely avoid hip prosthesis. Sometimes such an arrangement is not the best choice due to high dose to organs at risk and inhomogeneity correction for the prostheses is essential. In conventional treatment planning systems (TPS), the inhomogeneity correction can be calculated by the software by entering the correct electron densities for the prosthesis material. The position and shape of the prosthesis has to be known. However, these are often very difficult to define in CT images containing artifacts. Metal artifact correction algorithms produce artifact

reduced images and help identify the accurate position and shape of patients' prostheses. Finally, artifact corrected images can be used not only for MCTP but also for conventional TPS to properly account for tissue inhomogeneities.

4.3.4 Scatter and beam hardening as causes of metal streaking artifacts

The results from our preliminary study on scatter and beam hardening are summarized in figure 4-3.12. In order to quantify the differences in metal streaking artifacts, we present the mean HU of a rectangular water area extending between the steel cylinders. We will denote it as the test value. Without artifacts, the test value should correspond to HU of water (HU = 0).

All the images contain subtle streaks that are produced by the small number of projections (360 projections over 360°) in our Monte Carlo simulation compared to real CT scanners that use on average 10 times more projections. Nevertheless, the CT image obtained with the polyenergetic spectrum including scatter (figure 4-3.12a) is very similar to a real image produced by our CT scanner (not shown). The test value reads -80 HU which means that the density of this area is underestimated. The scatter-free image produced by the polyenergetic spectrum (figure 4-3.12b) shows less severe artifacts than the image with scatter. The HU in the area between the steel cylinders are higher, even though a dark streak is still visible. The test value for this case is -39 HU which is an improvement compared to -80 HU in figure 4-3.12a.

A monoenergetic spectrum was used to quantify the impact of beam hardening on metal streaking artifacts. As can be seen in figure 4-3.12c, the artifacts are almost identical with the monoenergetic spectrum as with the polyenergetic spectrum (figure 4-3.12a). There is only a slight improvement in the test value which is -78 HU.

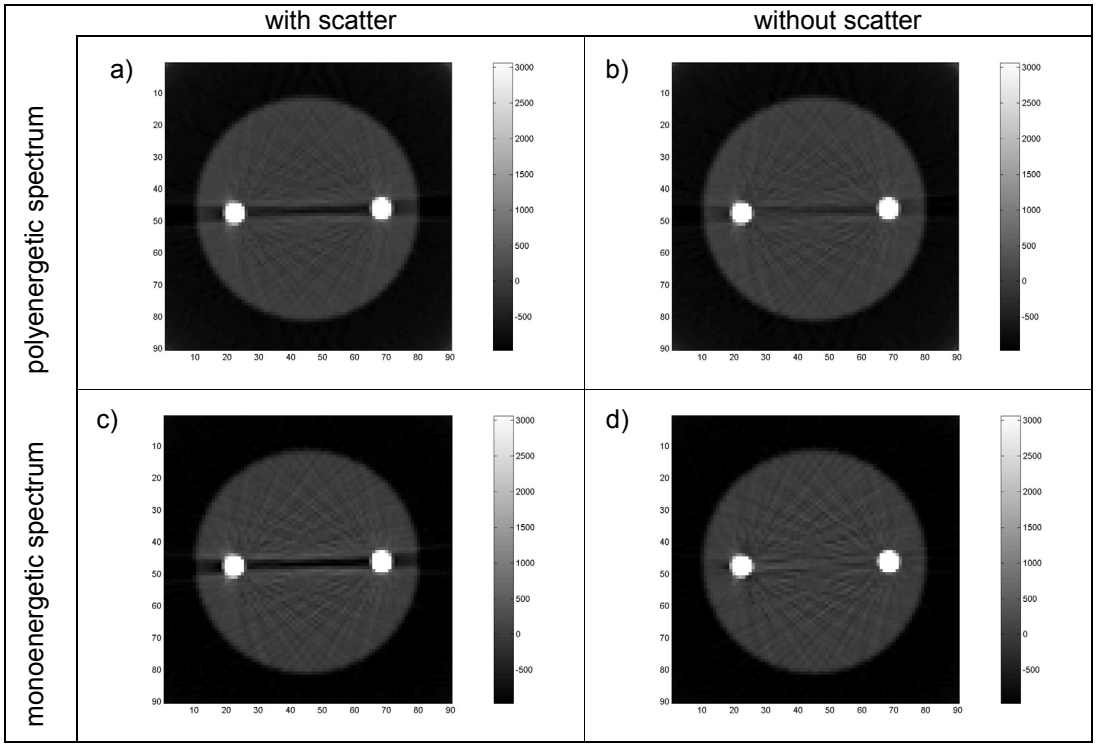

Figure 4-3.12: CT image of the phantom simulated with a 120 kVp x-ray spectrum with scattered photons (a), with only primary photons (b); simulated with a monoenergetic 75 keV x-ray beam with scattered x-rays (c) and with primary x-rays only (d).

On the other hand, figure 4-3.12d displays the scatter corrected image simulated with the monoenergetic spectrum that is almost artifact free. The test value improves significantly to 3 HU.

We have to note that the contribution of scatter in our MC simulation is more significant than in real CT scanners. The real CT scanners accommodate an anti-scatter collimator that prevents some of the scattered photons to reach the detectors

and which was not modeled. On the other hand, the noise, which is another important source of metal streaking artifacts [31] was not simulated at all. To summarize, whereas the scatter contribution is overestimated, the noise contribution is underestimated and figure 4-3.12a closely resembles the actual image obtained from the Picker scanner. Our results correspond to conclusions that Williamson *et al.* [31] drew in their paper.

Our study shows that in presence of scatter, the effect of beam hardening on metal streaking artifacts is minor. However, the best image is obtained with the primary monoenergetic beam. For the time being, it is not possible to use monoenergetic beams in CT scanners, however, a narrower spectrum can be obtained by adding appropriate filtration to the polychromatic x-ray beam. Also, the scatter contribution can be suppressed by using the smallest slice thickness. The collimators that define the slice thickness will help to avoid some of the scattered photons to reach the detectors.

4.4 Conclusions

A method for correction of CT metal streaking artifacts was implemented and validated on several test phantoms and on a prostate patient. The impact of the artifact correction on MC dose calculation has been evaluated on both phantoms and the patient in a set of beam geometries. MC dose distributions have been calculated for original CT images and CT artifact-corrected images with the EGSnrc/DOSXYZnrc code. The phantom calculations were compared to dose calculation in the exact geometry; the patient's dose distributions were compared by DVHs of a hypothetical target.

The correction algorithm clearly allows to identify and delineate various structures that are invisible in images containing artifacts. We have found that in order to calculate dose accurately in between two metallic objects, the artifact correction is essential. In addition, the procedure to convert HU values to a MC phantom has to be modified by adding an extra high-density material. In other words, an extended calibration has to be used. The errors in 6 MV photon dose calculations decreased from 25% for phantom images with CT artifacts when the default CT calibration was used to less than 2% for CT artifact-corrected images with the extended calibration. Similar improvement has been found for 18 MV photon beam and an 18 MeV electron beam dose calculations. A hypothetical treatment scenario of the prostate patient exhibits large differences in DVHs of a hypothetical target in the original geometry and in the artifact-corrected geometry, mainly due to miss-assignment of voxels to air in the presence of metal artifacts.

We have also briefly investigated scatter and beam hardening as causes of metal streaking artifacts. We have found that whereas beam hardening has a minor effect on metal artifacts, scattered photons are an important cause to these artifacts. A MC model of a CT scanner offers possibilities to reduce metal artifacts by removing scatter.

The metal streaking artifact correction algorithm results in a significant improvement in image quality, especially in the area between metallic objects and makes material segmentation and dose calculation more accurate. Our work strongly demonstrates the need of a metal streaking artifact correction method in Monte Carlo Treatment Planning. Omission of a correction algorithm for streaking artifacts in

MC planning systems will lead to large dose calculation errors and potential mistreatment of patients.

This chapter shows that metal streaking artifacts significantly influence Monte Carlo dose calculations for both electron and high energy photon beams. It is therefore suitable to use an artifact correction technique to obtain the real tissue properties. As demonstrated with a phantom study, the sinogram interpolation correction algorithm based on cubic spline interpolation gives satisfactory results and reduces the major artifacts. With the correction, tissue segmentation and density assignment is done more accurately resulting in more accurate calculations of dose distributions.

The correction algorithm worked well on a prostate patient with bilateral hip prostheses which resulted in an improved image quality and a more accurate tissue segmentation for dose calculations. A Monte Carlo simulation of a hypothetical treatment of the patient showed significant differences in the dose volume histogram of the prostate when the artifact correction is applied. In conclusion, a metal streaking artifact correction algorithm should be a part of any Monte Carlo treatment planning.

A MC simulation of CT image formation shows that beam hardening has a minor effect on the creation of metal streaking artifacts. Scatter and possibly detector noise are the main causes of metal artifacts in CT. Therefore, we suggest that an anti-scatter grid and a small beam collimation, if possible, are used. In the case of a

large collimation, such as in multi-detector CT or cone beam CT, a scatter correction algorithm might improve the image quality.

REFERENCES

[1] C.-M. Ma, E. Mok, A. Kapur, T. Pawlicki, D. Findley, S. Brain, K. Forster, and A. L. Boyer. Clinical implementation of a Monte Carlo treatment planning system. *Med. Phys.*, 26:2133–2143, 1999.

[2] J. Hsieh. *Image artifacts, causes, and corrections.* Advanced Medical, Madison, WI, 1995.

[3] T. Pawlicki and C.M. Ma. Effect of CT Streaking Artifacts in Monte Carlo Dose Distributions for Head and Neck Cancer. *XIII. ICCR Heidelberg Germany*, pages 414–416, 2000.

[4] W.A. Kalender, R. Hebel, and J. Ebersberger. Reduction of CT artifacts caused by metallic implants. *Radiology*, 164:576–577, 1987.

[5] J. Hsieh. Adaptive streak artifact reduction in computed tomography resulting from excessive x-ray photon noise. *Med. Phys.*, 25:2139–2147, 1998.

[6] D.L. Snyder, T.J. Schultz, and J.A. O'Sullivan. Deblurring subject to nonnegativity constraints. *IEEE T. Signal Process.*, 40:1143–1150, 1992.

[7] G. Wang, D.L. Snyder, J.A. O'Sullivan, and M.W. Vannier. Iterative Deblurring for CT Metal Artifact Reduction. *IEEE T. Med. Imaging*, 15:657–664, 1996.

[8] P.J. Keall, L.B. Chock, R. Jeraj, J.V. Siebers, and R. Mohan. Image reconstruction and the effect on dose calculation for hip prostheses. *Med. Dos.*, 28:113–117, 2003.

[9] D. Xia, J.C. Roeske, L. Yu, C.A. Pelizzari, A.J. Mundt, and X. Pan. A hybrid approach to reducing computed tomography metal artifacts in intracavitary brachytherapy. *Brachytherapy*, 4:18–23, 2005.

[10] B. De Man, J. Nuyts, P. Dupont, G. Marchal, and P. Suetens. An Iterative Maximum-Likelihood Polychromatic Algorithm for CT. *IEEE T. Med. Imaging*, 20:999–1008, 2001.

[11] J.C. Roeske, C. Lund, C.A. Pelizzari, X. Pan, and A.J. Mundt. Reduction of computed tomography metal artifacts due to the Fletcher-Suit applicator in gynecology patients receiving intracavitary brachytherapy. *Brachytherapy*, 2:207–214, 2003.

[12] M. Yazdi, L. Gingras, and L. Beaulieu. An adaptive approach to metal artifact reduction in helical computed tomography for radiation therapy treatment planning: experimental and clinical studies. *Int. J. Radiat. Oncol., Biol., Phys.*, 62:1224–1231, 2005.

[13] C. Reft, R. Alecu, I.J. Das, B.J. Gerbi, P. Keall, E. Lief, B.J. Mijnheer, N. Papanikolaou, C. Sibata, J. Van Dyk, and AAPM Radiation Therapy Committee Task Group 63. Dosimetric considerations for patients with HIP prostheses undergoing pelvic irradiation. report of the AAPM Radiation Therapy Committee Task Group 63. *Med. Phys.*, 31:1162–1182, 2003.

[14] X. Pan. Optimal noise control in and fast reconstruction of fan-beam computed tomography image. *Med. Phys.*, 26:689–697, 1999.

[15] B.R.B. Walters and D.W.O. Rogers. DOSXYZNRC Users Manual. *NRCC Report No. PIRS 794*, 2002.

[16] J. Seco, E. Adams, M. Bidmead, M. Partridge, and F. Verhaegen. Head-and-neck IMRT treatments assessed with a Monte Carlo dose calculation engine. *Phys. Med. Biol.*, 50:817–830, 2005.

[17] X.A. Li, L. Ma, S. Naqvi, R. Shih, and C. Yu. Monte Carlo dose verification for intensity-modulated arc therapy. *Phys. Med. Biol.*, 46:2269–2282, 2001.

[18] S. Stapleton, S. Zavgorodni, I.A. Popescu, and W.A. Beckham. Implementation of random set-up errors in Monte Carlo calculated dynamic IMRT treatment plans. *Phys. Med. Biol.*, 50:429–439, 2005.

[19] C. Boudreau, E. Heath, J. Seutjens, O. Ballivy, and W. Parker. IMRT head and neck treatment planning with a commercially available Monte Carlo based planning system. *Phys. Med. Biol.*, 50:879–890, 2005.

[20] A. Leal, F. Sanchez-Doblado, R. Arrans, J. Rosello, E.C. Pavon, and J.I. Lagares. Routine IMRT verification by means of an automated Monte Carlo simulation system. *Int. J. Radiat. Oncol. Biol. Phys.*, 56:58–68, 2003.

[21] T. Pawlicki and C.-M. Ma. Monte Carlo simulation for MLC-based intensity-modulated radiotherapy. *Med. Dos.*, 26:157–168, 2001.

[22] P. Francescon, S. Cora, and P. Chiovati. Dose verification of and IMRT treatment planning system with the BEAM EGS4-based Monte Carlo code. *Med. Phys.*, 30:144–157, 2003.

[23] E.D. Yorke, L. Wang, K.E. Rosenzweig, D. Mah, J.B. Paoli, and C.S. Chui. Evaluation of deep inspiration breath-hold lung treatment plans with Monte Carlo dose calculation. *Int. J. Radiat. Oncol.*, 53:1058–1070, 2002.

[24] L. Wang, E. Yorke, and C.S. Chui. Monte Carlo evaluation of tissue inhomogeneity effects in the treatment of the head and neck. *Int. J. Radiat. Oncol. Biol. Phys.*, 50:1339–1349, 2001.

[25] F.C. Du Plessis, C.A. Willemse, and M.G. Lotter amd L. Goedhals. Comparison of the Batho, ETAR and Monte Carlo dose calculation methods in CT based patient models. *Med. Phys.*, 28:582–589, 2001.

[26] W. Schneider, T. Bortfeld, and W. Schlegel. Correlation between CT numbers and tissue parameters needed for Monte Carlo simulations of clinical dose distributions. *Phys. Med. Biol.*, 45:459–478, 2000.

[27] C. Coolens and P.J. Childs. Calibration of CT Hounsfield units for radiotherapy treatment planning of patients with metallic hip prostheses: the use of extended CT-scale. *Phys. Med. Biol.*, 48:1591–1603, 2003.

[28] R. Mohan, C. Chui, and L. Lidofsky. Energy and angular distributions of photons from medical linear accelerators. *Med. Phys.*, 12:592–597, 1985.

[29] A.F. Bielajew. Fundamentals of the Monte Carlo Method for Neutral and Charged Particle Transport. *Course notes*, 2001.

[30] B. De Man, J. Nuyts, P. Dupont, G. Marchal, and P. Suetens. Metal Streak Artifacts in X-ray Computed Tomography: A Simulation Study. *IEEE T. Nucl. Sci.*, 46:691–696, 1999.

[31] J.F. Williamson, B.R. Whiting, J. Benac, R.J. Murphy, G.J. Blaine, J.A. O'Sullivan, D.G. Politte, and D.L. Snyder. Prospects for quantitative computed tomography imaging in the presence of foreign metal bodies using statistical image reconstruction. *Med. Phys.*, 29:2404–2418, 2002.

[32] D.W.O. Rogers, B.A. Faddegon, G.X. Ding, C.-M. Ma, and J. We. BEAM: A Monte Carlo code to simulate radiotherapy treatment units. *Med. Phys.*, 22:503–524, 1995.

[33] D.L. Parker. Optimal short scan convolution reconstruction for fan-beam CT. *Med. Phys.*, 9:254–257, 1982.

[34] F. Verhaegen and S. Devic. Sensitivity study for CT image use in Monte Carlo treatment planning. *Phys. Med. Biol.*, 50:937–946, 2005.

[35] F. Verhaegen and IJ Das. Interface dosimetry for kV and MV photon beams. *Recent Developments in Accurate Radiation Dosimetry*, pages 268–287, 2002.

CHAPTER 5
Monte Carlo dose calculations for phantoms with hip prostheses

In the previous chapter it was shown that CT metal streaking artifacts make Monte Carlo dose calculations inaccurate and the improvement of dose calculations using artifact corrected images was demonstrated. The study was mainly carried out with phantoms with steel cylinders mimicking dental fillings and hip prostheses. However, real prostheses are mostly irregularly shaped, as was seen in the patient study. Correction of metal artifacts caused by irregularly shaped metals is more challenging. The artifact correction algorithm presented in the previous chapter is tested with real hip prostheses in this chapter. The magnitude of metal streaking artifacts for three common hip prosthesis materials is examined. Monte Carlo dose calculations for both unilateral and bilateral prosthesis phantoms are performed and the effect of the artifacts on the calculated dose distributions is studied by means of a hypothetical prostate treatment.

Authors: M. Bazalova, C. Coolens, F. Cury, P. Childs, L. Beaulieu and F. Verhaegen
Published in: *Journal of Physics: Conference Series* **102** 2008

Abstract

Computed tomography (CT) images of patients with hip prostheses are severely degraded by metal streaking artifacts. The low image quality makes organ contouring more difficult and can result in large dose calculation errors when Monte Carlo (MC)

techniques are used. In this work, the extent of streaking artifacts produced by three common hip prosthesis materials (Ti-alloy, stainless steel and Co-Cr-Mo alloy) was studied. The prostheses were tested in a hypothetical prostate treatment with five 18 MV photon beams. The dose distributions for unilateral and bilateral prosthesis phantoms were calculated with the EGSnrc/DOSXYZnrc MC code. This was done in three phantom geometries: in the exact geometry, in the original CT geometry and in an artifact-corrected geometry. The artifact-corrected geometry was created using a modified filtered back-projection correction technique. It was found that unilateral prosthesis phantoms do not show large dose calculation errors, as long as the beams miss the artifact-affected volume. This is possible to achieve in the case of unilateral prosthesis phantoms (except for the Co-Cr-Mo prosthesis which gives a 3% error) but not in the case of bilateral prosthesis phantoms. The largest dose discrepancies were obtained for the bilateral Co-Cr-Mo hip prosthesis phantom, up to 11% in some voxels within the prostate. The artifact correction algorithm worked well for all phantoms and resulted in dose calculation errors below 2%. In conclusion, a MC treatment plan should include an artifact correction algorithm when treating patients with hip prostheses.

5.1 Introduction

Metal streaking artifacts in computed tomography (CT) can severely degrade image quality. CT images of patients with metal artifacts due to dental work, surgical clips or hip prostheses are often very difficult to contour. Moreover, it has been shown that metal streaking artifacts cause dose calculation errors in treatment planning systems taking heterogeneities into account [1], especially in those using Monte Carlo

(MC) simulations [2]. Bazalova *et al.* [2] also show that in order to avoid large MC dose discrepancies, an artifact correction technique should be used when calculating the dose to patients having hip prostheses. Another option to consider for patients having bilateral hip replacements is a prostate brachytherapy implant procedure.

Various artifact correction techniques are available to improve the image quality. The two main approaches for correction of metal artifacts are iterative techniques [3] and techniques based on modified filtered back-projection [4]. Modified filtered-back projection techniques result in a slightly lower image quality than iterative techniques, nevertheless, they are used for their shorter computation time. A technique based on modified filtered back-projection using cubic interpolation is used in this work. The technique is described in detail elsewhere [2]. It basically involves interpolation of corrupted sinogram data corresponding to metallic objects using adjacent projections and cubic interpolation. The method works very well for simple prosthesis geometries. For complex prosthesis geometries, the algorithm corrects the large artifacts and results in formation of minor streaks. It has to be noted that an alternative approach to more accurate treatment of patients with hip prostheses is the use of the extended CT-scale as demonstrated by Coolens and Childs [5].

In this work, we evaluated the effect of three common hip prosthesis materials on the extent of metal streaking artifacts and their influence on MC dose calculation. We also applied a sinogram interpolation method based on cubic splines on the original CT images, obtained artifact-corrected CT geometries and evaluated the effect of the correction on MC dose calculations.

5.2 Materials and methods

One or two prostheses made of three common prosthesis materials were placed in a 27 cm diameter cylindrical acrylic phantom filled with water. This allowed us to construct unilateral and bilateral hip prosthesis pelvic phantoms.

5.2.1 Prosthesis materials

The elemental compositions of the three common hip prosthesis materials [6] are listed in table 5-2.1. Ti-alloy with the lowest mass density (4.48 g/cm^3) produces the least artifacts. Co-Cr-Mo alloy with 8.20 g/cm^3 creates the most artifacts, as shown in figure 5-2.1 where phantom CT images and photographs of the prostheses are presented. As can be seen in figure 5-2.1b, a solid steel acetabular cup is a part of the stainless steel prostheses. Ceramic acetabular cups can be placed on the stem of the Ti-alloy and Co-Cr-Mo alloy prostheses, however, they were not used in our experiments.

Table 5-2.1: Elemental composition (fraction by weight) and mass densities (ρ) of three common hip prosthesis materials.

Ti-alloy ρ=4.48 g/cm^3		Stainless steel ρ=6.45 g/cm^3		Co-Cr-Mo alloy ρ=8.20 g/cm^3	
Ti	89.17	Fe	62.72	Co	61.90
Al	6.20	Cr	21.00	Cr	28.00
V	4.00	Ni	9.00	Mo	6.00
Fe	0.30	Mn	3.60	Mn	1.00
O	0.20	Mo	2.50	Si	1.00
C	0.08	Si	0.75	Fe	1.00
N	0.05	N	0.43	Ni	0.75
				C	0.35

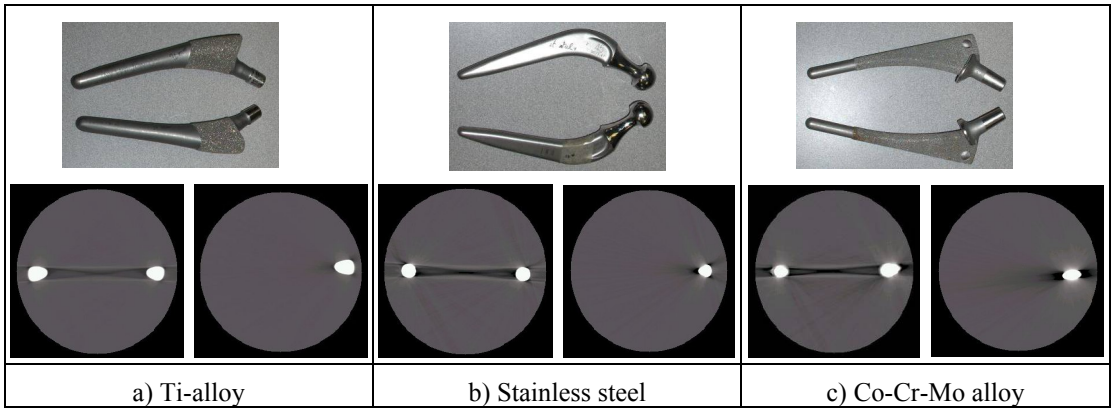

Figure 5-2.1: Photographs of three common types of hip prostheses and the extent of artifacts produced by them in bilateral and unilateral prosthesis water phantoms.

5.2.2 Scanning parameters and artifact correction

The hip prosthesis phantoms were scanned on a PQ5000 single slice CT scanner (Royal Philips Electronics, Eindhoven, the Netherlands). The axial mode was chosen to acquire 5 mm thick slices at 5 mm separation, 130 kVp and 400 mAs. Moreover, a 100 kVp scan of the Ti-alloy bilateral phantom was taken and the effect of tube voltage on metal artifacts was evaluated. All scans consisted of 24 images with 512×512 pixels. The pixel size was determined by the 48 cm field size to be 0.94 mm.

The phantom raw data were saved in the scanner and transferred via a modem connection to a PC for processing. The raw data consisted of 512 detector readings at 2400 x-ray tube positions and were subsequently converted to sinograms. The sinogram interpolation correction algorithm based on cubic spline interpolation was run for each slice on a 1.6 GHz PC in Matlab (The Mathworks, Natick, MA). The correction of one slice took approximately 11 minutes.

5.2.3 Treatment plan

The original CT images of the bilateral steel prosthesis phantom with metal streaking artifacts were transferred to a contouring station and a physician was asked to create a prostate case by delineating a fictitious prostate (target) and rectum (organ at risk). The CT images with the contours were then transferred to a planning station and the external contour of the phantom was semi-automatically drawn. The automatic external contour detection of the surface of the phantom failed due to the presence of metal artifacts and the contouring had to be completed manually. The geometry of the steel bilateral prosthesis phantom is presented in figure 5-2.2. The external contour is drawn in blue, steel prostheses in black, the prostate in red and the rectum in green. The prostate volume is 42.8 cc.

Subsequently, a dosimetrist generated a treatment plan. A five 18 MV co-planar photon beam arrangement was chosen as it is commonly used for prostate treatments in our hospital. Since the prostheses were relatively small, a setup with all beams missing the prosthesis could be used. The beam angles were 300°, 230°, 0° (using IEC convention), 60° and 130° with field sizes being 5.5 cm in x and 8.0 cm in y which spared the rectum. The treatment plan was then applied to all phantoms.

5.2.4 Monte Carlo dose calculations

The beam arrangement from the planning station was implemented in the EGSnrc/DOSXYZnrc [7] Monte Carlo code. The CT images of the phantom were used to create three sets of geometry files in the following way. First, the exact geometry was built on the basis of the original CT images by assigning the voxels with the maximum CT number (or Hounsfield unit, HU, 3095 for our scanner where HU =

0 for water) to the corresponding prosthesis material. The remaining voxels of the phantom were assigned to water with mass density $1.0\,\mathrm{g/cm^3}$.

Secondly, the original CT geometry and the corrected geometry were created on the basis of the original CT images and the artifact-corrected images, respectively. Similarly to the exact geometry, the 3095 HU voxels were assigned to the corresponding prosthesis material. Remaining voxels in the phantom were assigned to water, including the voxels with the low CT numbers due to the artifacts. The mass densities were assigned on the basis of the scan and a (HU, ρ) calibration curve. The calibration curve was obtained using scans of an RMI electron density calibration phantom (Gammex, Middleton, WI) taken at the corresponding tube voltage.

Note that the contouring of the prostheses was done using a simplistic approach that assigns the saturated HU to the corresponding prosthesis material. However, since identical prosthesis contours were used in all three geometries (in the exact, original CT and in the artifact-corrected geometry), the dose distributions are consistent and the dose differences are not compromised by the prosthesis geometries. The exact prosthesis geometry could be found by applying the filtered back-projection on the raw data and using a pre-defined windowing and leveling [5].

The acrylic cylinder was excluded from the geometry. As can be seen in figure 5-2.2, the prostate is very close to the top of the phantom. This geometry might result in a lack of scattered radiation. In order to account for the scatter, a 10 cm layer of uniform water was added on top of the phantom in all geometries.

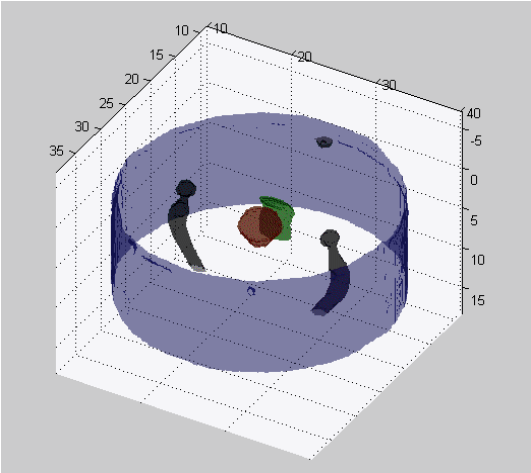

Figure 5-2.2: Phantom geometry - external contour (blue), steel prostheses (black), prostate (red) and rectum (green).

Three dose calculations were performed for each of the phantom geometries: in the exact geometry (D_{ex}), in the original CT geometry (D_{or}) and in the artifact-corrected geometry (D_{cor}). The resulting dose distributions were compared. The calculations were run with $1{\times}10^9$ particles with the energy cut-offs of 10 keV for both photons and electrons. The dose to air was set to zero, as commonly done in MC dose calculations. The dose calculation uncertainty in high dose regions did not exceed 1.2%.

5.3 Results

The results are presented in two different ways. In order to evaluate the effect of the artifact correction algorithm on the image quality, the original CT images and the artifact-corrected images of the isocentric slice are displayed. Percentage dose difference maps of the isocentric slice are also plotted. The dose difference map in

the original geometry is calculated as $(D_{ex}\text{-}D_{or})/D_{ex}$ and in the artifact-corrected geometry as $(D_{ex}\text{-}D_{cor})/D_{ex}$.

5.3.1 Bilateral prosthesis phantoms

All bilateral prosthesis phantoms contained severe artifacts. The most severe artifacts were observed for the high density Co-Cr-Mo alloy (figure 5-3.3). Figure 5-3.3a shows the large extent of the artifacts and it can be seen clearly that the prostate (in red) is contoured in the area where the streaks are the most pronounced. The artifact-corrected image produced using the sinogram interpolation method is presented in figure 5-3.3b where the large artifacts between the prostheses are completely corrected. Note that minor streaks in the vicinity of the prostheses appeared which is fairly typical for the sinogram interpolation correction algorithm. The dose difference maps of the original geometry and the artifact-corrected geometry with respect to the exact geometry are plotted in figure 5-3.3c and 5-3.3d, respectively. The artifact-affected area of figure 5-3.3c is enlarged in figure 5-3.3e. Note that the scale is also enlarged in figure 5-3.3e.

As can be seen in figure 5-3.3e, some voxels have dose calculation errors larger than 15%. This comes from the fact that dose to air was set to zero in the DOSXYZnrc calculation. When this option is chosen, the dose to artifact-affected voxels with density > 0.044 g/cm^3 is zeroed, which results in dose differences close to 100%. Figure 5-3.3e also contains non-air voxels with dose calculation errors from -3% up to 11% in the prostate volume that are entirely caused by the metal streaking artifacts. Since the rectum is contoured outside the artifacts for all phantoms, the dose differences in the rectum are within 2% for all phantom geometries. Figure 5-3.3d

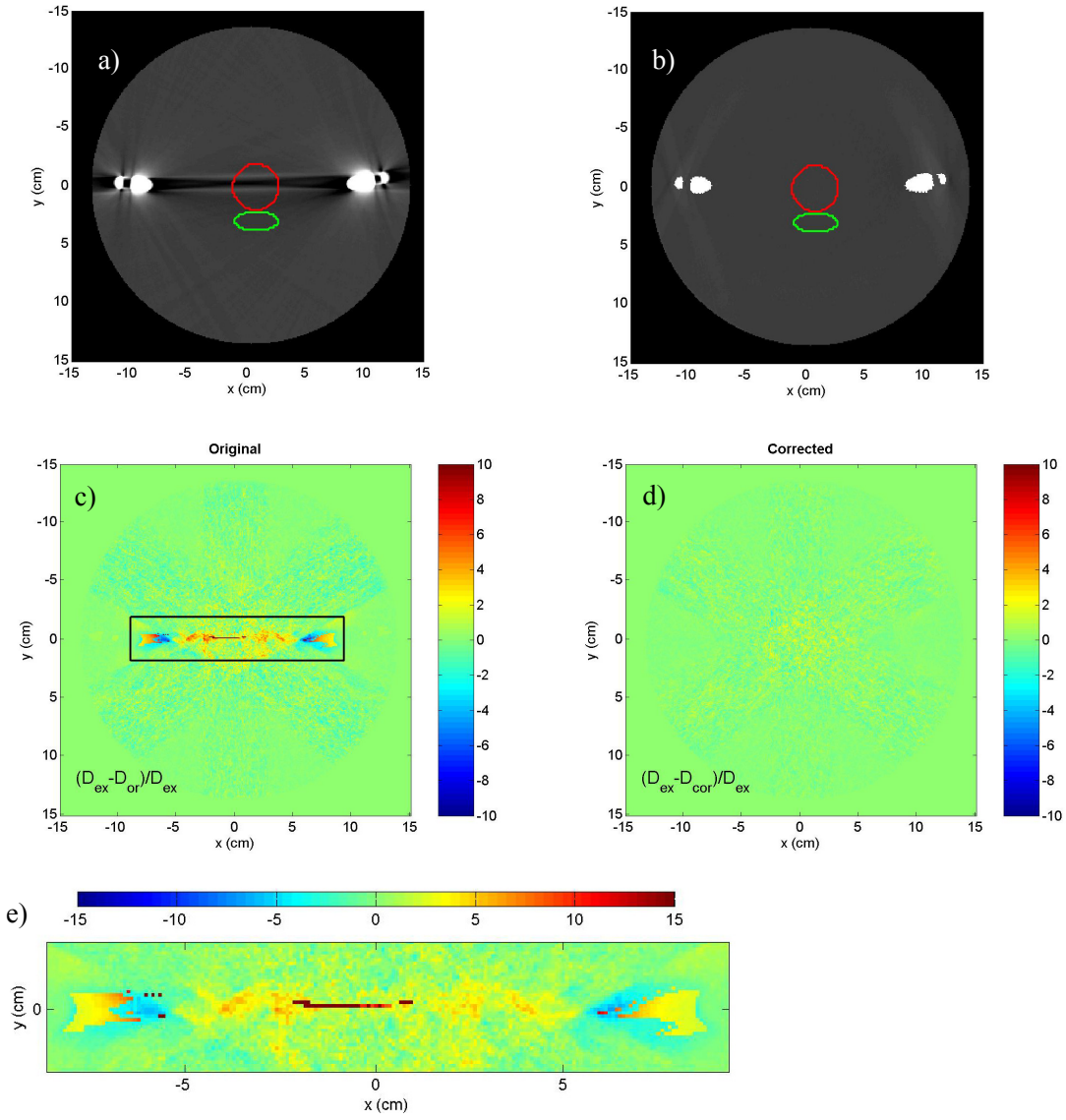

Figure 5-3.3: CT images of the original geometry (a) and the artifact-corrected geometry (b) for the Co-Cr-Mo alloy bilateral prosthesis phantom. Differences in dose distribution from the exact geometry for the original CT geometry (c) and the artifact-corrected geometry (d). The artifact-affected volume marked by the black rectangle of (c) is enlarged in (e).

demonstrates that MC dose calculations are improved in the artifact-corrected geometry. The dose calculation errors are within 2% and reflect statistical uncertainties of the calculation.

The remaining results for the Ti-alloy and the steel prosthesis phantoms are not shown, however, the maximum dose errors in voxels with density > 0.044 g/cm^3 were found to be 3% and 5%, respectively. The correction algorithm produced geometries with suppressed metal artifacts that resulted in dose difference maps with dose calculation errors within 2%.

5.3.2 Unilateral prosthesis phantoms

The results for the Co-Cr-Mo unilateral prosthesis phantom are shown in figure 5-3.4. The original CT image and the artifact-corrected image of the isocentric slice are displayed in figure 5-3.4a and 5-3.4b, respectively. As expected, artifacts produced by one Co-Cr-Mo prosthesis are less severe than artifacts produced by two Co-Cr-Mo prostheses. Nevertheless, streaks are spread in the entire phantom. The correction algorithm works well and corrects for the main artifacts (figure 5-3.4b).

Since one of the five 18 MV photon beams does not miss the small volume affected by the artifacts, the dose distribution in the original geometry is affected by the streaking artifacts. Dose uncertainties up to 3% are observed close to the right prosthesis in the original CT geometry (figure 5-3.4c). The rest of dose difference map for the original geometry and the entire dose difference map for the artifact-corrected geometry (figure 5-3.4d) reflect mostly the dose calculation uncertainties.

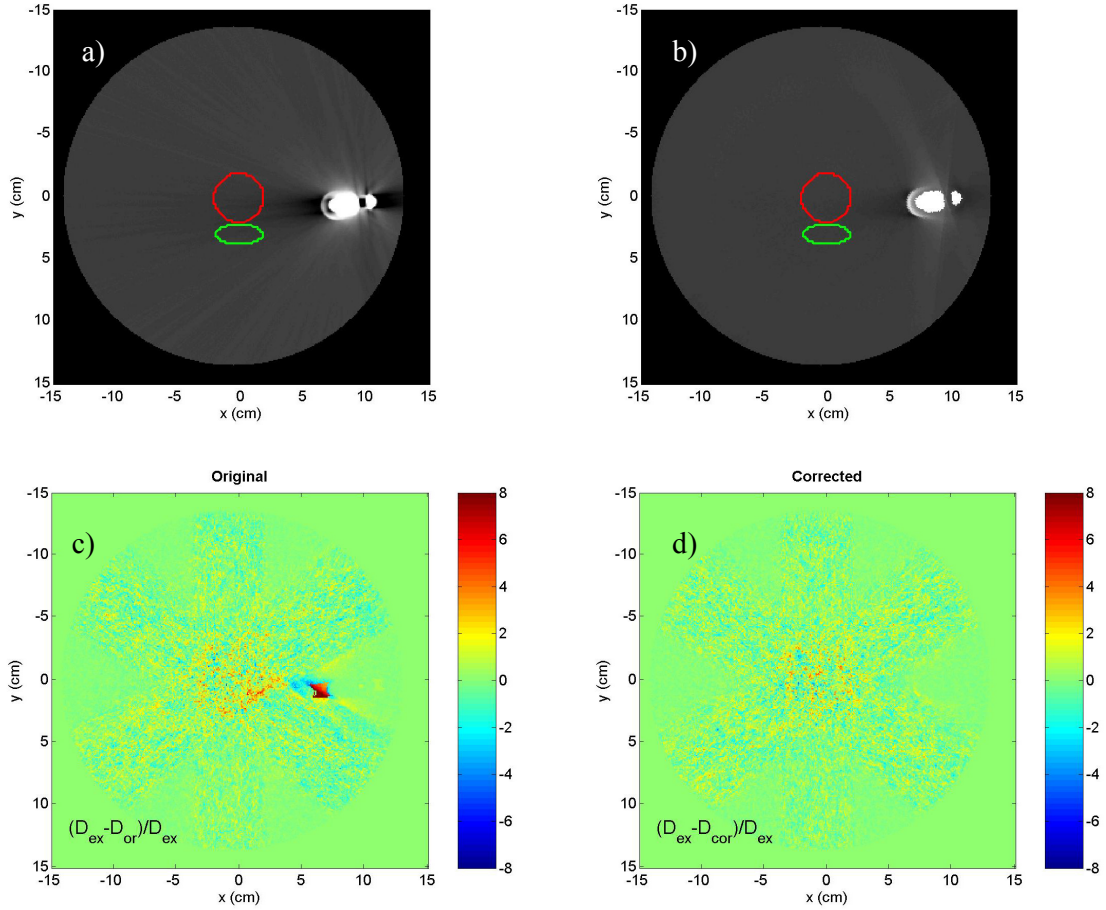

Figure 5-3.4: CT images of the original geometry (a) and the artifact-corrected geometry (b) for the Co-Cr-Mo unilateral prosthesis phantom. Dose distribution differences from the exact geometry for the original CT geometry (c) and the artifact-corrected geometry (d).

It should be noted that the direction of the 130° beam that passes through the artifact affected volume should not be changed. It could be only changed in the clockwise direction which would result in excessive dose to the rectum.

The results for the unilateral Ti-alloy phantom and the steel phantom are not presented. The artifact-affected volume for these prostheses is small. Therefore, the photon beams miss the volume affected by the streaking artifacts. As a result, the dose distribution in the original geometry is very similar to the dose distribution in the exact geometry and in the artifact-corrected geometry. The dose difference maps are very similar and reflect only the dose calculation uncertainties.

5.3.3 Effect of tube voltage

The effect of tube voltage on the extent of metal streaking artifacts was studied on the bilateral Ti-alloy phantom. A scan at 100 kVp produced significantly more artifacts than the scan at 130 kVp. The maximum dose difference from the exact geometry increased from 3% for the 130 kVp geometry to 5% for the 100 kVp geometry within the prostate volume. The artifact correction algorithm worked again very well and the dose distribution in the artifact-corrected geometry was in agreement with the exact geometry dose distribution. As our example demonstrates, higher tube voltages should be used for patients with hip prostheses, if possible.

5.4 Conclusions

We have evaluated the effects of metal streaking artifacts produced by three common hip prosthesis materials on Monte Carlo dose calculations for a hypothetical five 18 MV photon beam prostate treatment. Unilateral and bilateral Ti-alloy, stainless steel and Co-Cr-Mo prosthesis phantoms with a fictitious prostate and rectum were studied. A sinogram interpolation method for correction of metal artifacts was applied on all phantoms and the effect of the correction on MC dose calculations was also evaluated.

It was found that bilateral hip prosthesis phantoms show significant streaking artifacts for all hip prosthesis materials. The largest dose discrepancies due to the artifacts were observed for the high density Co-Cr-Mo bilateral phantom. The dose calculation errors from the exact geometry were as high as 11% in the prostate volume. The dose calculation errors for the bilateral Ti-alloy and steel prosthesis phantoms were 3% and 5%, respectively.

Unilateral prosthesis phantoms show less streaking artifacts than bilateral prosthesis phantoms. Therefore, in the case of the unilateral low density (steel and Ti-alloy) prosthesis phantoms, it is possible to choose a beam arrangement that misses the artifact affected volume. As a result, the calculated dose distributions are not affected by the presence of the artifacts which strongly depends on the size of the prosthesis and the patient geometry. However, artifacts in the phantom with the high density Co-Cr-Mo prosthesis were more pronounced and the beam close to the prosthesis could not avoid the artifact-affected volume. This caused a 3% dose discrepancy from the exact geometry.

The effect of tube voltage on the extent of artifacts was studied for the bilateral Ti-alloy phantom. It was found that in order to decrease dose calculation errors (assuming no artifact correction algorithm), higher tube voltages should be used when scanning patients with bilateral hip prosthesis. However, when the artifact correction algorithms based on interpolation of sinograms are used, the effect of tube voltage is insignificant.

The sinogram interpolation correction algorithm performed well in all phantom geometries which resulted in dose calculations errors below 2%. We conclude that in

order to avoid large dose discrepancies, Monte Carlo treatment planning for bilateral hip prosthesis patients should always include a metal artifact correction algorithm. If one or more beams pass through the artifact-affected volume, a correction algorithm for metal streaking artifacts should be also used for patients with one hip prosthesis.

The results of this chapter show the extent of CT artifacts caused by real hip prostheses. They also demonstrate that the sinogram artifact correction algorithm based on cubic spline interpolation works well on phantoms with real prostheses. The study indicates that the artifact correction will work reasonably well for any patients with hip implants.

This chapter demonstrates that Monte Carlo dose calculations are more accurate when the artifact correction is taken into account, especially when one or more of the treatment beams interact with the prostheses. It can be expected that significant dose calculation errors due to metal artifacts will be seen for patients with high-density Co-Cr-Mo prostheses. In conclusion, omitting a CT artifact correction caused by hip prostheses may result in inaccurate dose calculations affecting the outcome of radiotherapy treatments.

REFERENCES

[1] Y. Kim, W.A. Tom, M. Bal, T.R. McNutt, and L. Spies. The impact of dental metal artifacts on head and neck IMRT dose distributions. *Radiother. Oncol.*, 79:198–202, 2006.

[2] M. Bazalova, L. Beaulieu, S. Palefsky, and F. Verhaegen. Correction of CT artifacts and its influence on Monte Carlo dose calculations. *Med. Phys.*, 34:2119–2132, 2007.

[3] G. Wang, D.L. Snyder, J.A. O'Sullivan, and M.W. Vannier. Iterative Deblurring for CT Metal Artefact Reduction. *IEEE T. Med. Imaging*, 15:657–664, 1996.

[4] M. Yazdi, L. Gingras, and L. Beaulieu. An adaptive approach to metal artefact reduction in helical computed tomography for radiation therapy treatment planning: experimental and clinical studies. *Int. J. Radiat. Oncol., Biol., Phys.*, 62:1224–1231, 2005.

[5] C. Coolens and P.J. Childs. Calibration of CT Hounsfield units for radiotherapy treatment planning of patients with metallic hip prostheses: the use of extended CT-scale. *Phys. Med. Biol.*, 48:1591–1603, 2003.

[6] C. Reft, R. Alecu, I.J. Das, B.J. Gerbi, P. Keall, E. Lief, B.J. Mijnheer, N. Papanikolaou, C. Sibata, J. Van Dyk, and AAPM Radiation Therapy Committee Task Group 63. Dosimetric considerations for patients with HIP prostheses undergoing pelvic irradiation. report of the AAPM Radiation Therapy Committee Task Group 63. *Med. Phys.*, 31:1162–1182, 2003.

[7] B.R.B. Walters and D.W.O. Rogers. DOSXYZnrc Users Manual. *NRCC Report No. PIRS 794revB*, 2007.

CHAPTER 6
Monte Carlo simulation of a computed tomography x-ray tube

As demonstrated in chapter 4, scattered photons are one of the main contributors to CT metal artifacts. The only technique to determine the properties of scattered particles is the Monte Carlo method. In order to accurately evaluate the amount of scatter in CT, spectral characteristics of the CT x-ray beam have to be well known. This chapter presents a Monte Carlo model of a CT x-ray tube and its validation with spectral and half-value layer measurements.

With the increased number of CT examinations and the complexity of new multi-detector CT scanners, an accurate MC model of a CT x-ray tube in combination with patient CT will help to accurately evaluate the dose from CT. Thus, another application of the work presented in this chapter, published in *Physics in Medicine and Biology*, is the calculation of CT dose.

Authors: M. Bazalova and F. Verhaegen

Published in: *Physics in Medicine and Biology* **52** 5945-5955, 2007

Abstract

The dose delivered to patients during computed tomography (CT) exams has increased in the past decade. With the increasing complexity of CT examinations, measurement of dose becomes more difficult and more important. In some cases, the standard methods, such as measurement of the computed tomography dose index

(CTDI), are currently under question. One approach to determine the dose from CT exams is to use Monte Carlo (MC) methods. Since the patient geometry can be included in the model, Monte Carlo simulations are potentially the most accurate method of determining dose delivered to patients. In this work, we developed a MC model of a CT x-ray tube. The model was validated with half-value layer (HVL) measurements and spectral measurements with a high resolution Schottky CdTe spectrometer. First and second HVL for beams without additional filtration calculated from the MC modeled spectra and determined from attenuation measurements differ by less than 2.5%. The differences between first and second HVL for both filtered and non-filtered beams calculated from the MC modeled spectra and spectral measurements with the CdTe detector were less than 1.8%. The MC modeled spectra match the directly measured spectra. This works presents a first step towards an accurate MC model of a CT scanner.

6.1 Introduction

Computed tomography (CT) is an essential part of today's radiological diagnostics. CT is a high performance imaging modality that combines good image resolution with high tissue contrast. Due to the advances in CT technology, the relative number of CT examinations of all radiological examinations has increased from 2% to 10-15% in some countries in the past ten years [1]. As a result, their contribution to the total dose from medical examinations is very significant, accounting for 34% of the collective dose [1]. Epidemiological studies have shown that the absorbed dose to tissues from CT can often approach or exceed levels known to increase the probability of cancer [1].

With the development of new CT techniques, such as multi-slice CT, cine CT or cone beam CT, determination of dose delivered to patients during complex CT exams becomes more difficult. Brenner in his Letter to the Editor [2] questioned the use of the standard computed tomography dose index for CT quality assurance and dose optimization. More recently, Mori *et al.* showed that the CTDI can no longer be used in multi-slice CT exams using scanners with a large detector size [3]. The authors estimate the CT dose by using a conversion factor which is determined by a set of measurements with a 300 mm and a 100 mm long ionization chamber.

Another approach to estimate CT dose is using Monte Carlo (MC) methods [4]. Since the anatomy of individual patients can be included in the MC model, this approach is potentially superior to any other available method. However, in order to calculate the dose with high accuracy, it is necessary to have an accurate Monte Carlo model of the CT scanner. The model has to include simulation of the x-ray tube, beam filters and shapers and patient anatomy. In order to simulate image formation and image quality, the MC model has to be completed by the detector ring geometry. All the CT components have to be modeled with high accuracy.

The aim of this work is to develop an accurate MC model of a CT x-ray tube. Spectral measurements on the central axis of the x-ray beam are performed and compared to spectra obtained by the MC model of the x-ray tube. Half-value layer (HVL) measurements are used in the Monte Carlo model for determination of inherent filtration of the x-ray tube.

For measurements of diagnostic x-ray spectra, semiconductor detectors are often used, such as high purity germanium (HP-Ge) [5–7] and compound semiconductors

such as cadmium zinc telluride (CdZnTe) and cadmium telluride (CdTe). As opposed to HP-Ge detectors, detectors with a small thermoelectric cooling element (CdTe and CdZnTe) do not require a large liquid nitrogen cryogenic system which makes them very practical for measurements in radiological diagnostics. Whereas HP-Ge detectors are used for their excellent energy resolution, compound semiconductor detectors are used for their compactness. Miyajima [8] showed that CdZnTe spectra are distorted due to charge trapping. He also demonstrated that correction for charge trapping of photon spectra measured by a CdTe detector is not necessary. Therefore, a new generation CdTe spectrometer was used in our work.

It was shown in several works [9–13] that due to the high photon fluence and consequent pile-up in the detector, spectral measurements of diagnostic x-ray tubes are not trivial. The high photon fluence can be decreased by using very small collimators (as small as 50 μm in diameter) and placing the detector several meters away from the focal spot which is in case of CT scanners impossible.

The Compton scattering technique, introduced in radiological imaging by Yaffe *et al.* [9] and developed in several works [10–12], is also very efficient in reducing the number of photons. These workers designed a device known as a Compton spectrometer that measures 90° scattered photons from a scattering object. They studied the effect of different scattering materials and geometries on the energy resolution of the whole system. More recently, Maeda *et al.* [13] measured diagnostic x-ray spectra using Compton scattering on a carbon scattering target. This geometry is rather simple and can be easily accommodated in a CT scanner. As far as we know, the technique has not yet been reported for use in CT scanners.

In this work, a MC model of a CT x-ray tube based on HVL measurements was created. We then compared MC simulated spectra to CT spectra measured by the Compton method using a high resolution CdTe detector and scattering on a carbon scatterer. The MC simulated spectra were also compared to spectra produced by the TASMIP algorithm [14]. TASMIP is a code that interpolates measured constant potential x-ray spectra published by Fewell *et al.* [15].

An accurate MC model of a CT x-ray tube is a first step toward developing a model of a whole CT scanner that will allow us to estimate the CT dose. It will also be a useful tool for understanding imaging processes and might be helpful in reducing scatter and CT artifacts, such as metal streaking artifacts.

6.2 Materials and methods

6.2.1 Spectral measurements

Spectral measurements of the x-ray tube (Rhino 6.5, DUNLEE, Illinois, USA) of our CT scanner (Picker PQ5000, Royal Philips Electronics, Eindhoven, the Netherlands) were performed with a high resolution Schottky CdTe spectrometer (XR-100T, AMPTEK Inc, Bedford, MA) in a Compton scatter setup. The detector is a $3\times3\,\mathrm{mm}^2$ and 1 mm thick CdTe crystal with an energy resolution of 1.1% for ^{57}Co (122 keV). The detector operated at a bias voltage of 500 V. The energy calibration was done with the 31 keV peak of ^{133}Ba. The energy bin widths for the multichannel analyzer were set to 0.5 keV.

The x-ray tube was in a stationary position, pointing downwards, as shown in figure 6-2.1. A carbon scatterer (a $2\times2\times2\,\mathrm{cm}^3$ carbon block cut at 45°) was positioned at the isocenter of the gantry. A carbon scatterer was chosen because of its

low atomic number with no characteristic x-rays above 0.3 keV. The spectrometer was placed on the couch at 2 m from the isocenter to minimize the range of scattering angles. In addition, a 2 mm diameter tungsten collimator was mounted on the detector in order to further reduce the scattering angle range and to prevent the scattered photons from interacting at the edge of the CdTe crystal.

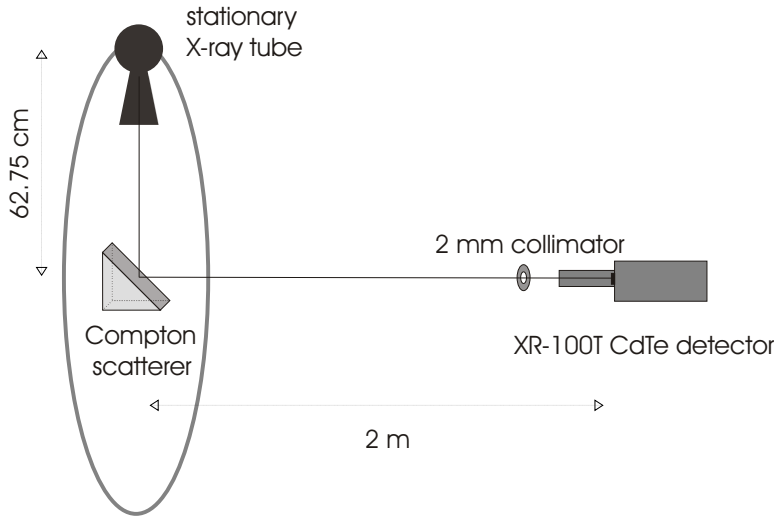

Figure 6-2.1: Compton scattering setup for spectral measurements.

Detector response

The measured spectra are distorted by the response of the detector. Therefore, they have to be corrected for photoelectric, coherent scattering and Compton scattering interactions that occur in the CdTe crystal. Seltzer [16] introduced a procedure, described as a stripping method, that corrects for the detector response. The stripping method was later modified by Maeda *et al.* [13] to the following form:

$$N_t(E_0) = \frac{N_d(E_0) - \sum_{E=E_0+0.5}^{E_{max}} R(E_0, E) N_t(E)}{R(E_0, E_0)}, \qquad (6\text{-}2.1)$$

where $N_t(E_0)$ is the true number of photons with energy E_0 (in keV), $N_d(E_0)$ is the number of photons detected with E_0, E_{max} is the maximum energy in the detected spectrum, $R(E_0,E)$ is the monoenergetic response function and $R(E_0,E_0)$ is the full energy absorption peak efficiency. The monoenergetic response functions were obtained using Monte Carlo simulations in a modified version of the EGSnrc/DOSXYZnrc code [17]. Monoenergetic beams (3.0 to 150 keV in 0.5 keV intervals) of 2 mm in diameter impinged on a $(3\times3\times1)\,\mathrm{mm}^3$ CdTe crystal and the monoenergetic response functions were determined by scoring the energy deposited in the crystal. The beryllium window ($100\,\mu$m) and the two 200 nm metallic contacts (Pt on top and In on bottom) were also included in the geometry. Similarly to work by Miyajima [8], the effects of carrier trapping and the dead layer of the crystal were not included in the response functions because they were shown to be insignificant in thin crystals operating at high voltages.

The full-energy absorption efficiency of the 1 mm thick CdTe spectrometer calculated from the response functions is presented in figure 6-2.2. It is in a good agreement with the curve calculated with the LSCAT/EGS4 code presented by Miyajima [8]. The discontinuities are due to K-absorption edges of Cd and Te and L-absorption edges of Pt.

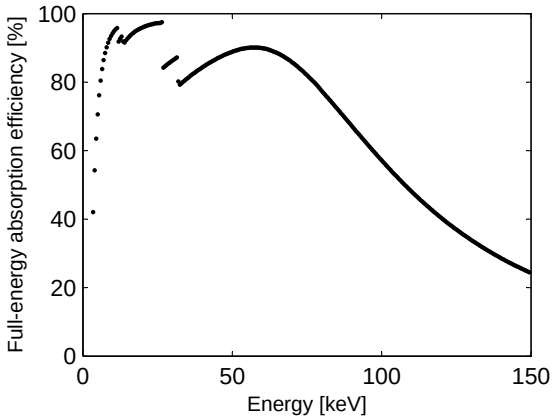

Figure 6-2.2: Full-energy absorption efficiency of a 1 mm thick CdTe detector calculated with the EGSnrc/DOSXYZnrc code.

Reconstruction of primary spectra

The primary x-ray spectra were found by correcting the 90° scattered spectra for Compton scatter using an energy shift, the Klein-Nishina formula and deconvolution of the characteristic x-ray peaks. The attenuation in air due to the 2 m air gap between the scatterer and the spectrometer was also taken into account. The scatterer was removed and multiple-scatter radiation that was not due to the 90° Compton scattering on the carbon block was measured. The scatter from the CT gantry, the couch and the walls was found to be insignificant for our measurement.

The primary photons with energy $h\nu$ scattered at 90° were detected with energy $h\nu'$. The primary photon energy can be calculated from:

$$h\nu = \frac{h\nu'}{1 - \frac{h\nu'}{m_e c^2}} \tag{6-2.2}$$

where $m_e c^2$ is the rest mass of an electron.

The primary spectra $\phi_0(h\nu)$ are reconstructed from the intensities of the scattered spectra $\phi'(h\nu)$ by using the Klein-Nishina formula [13]:

$$\phi_0(h\nu) = \frac{\phi'(h\nu)}{\frac{1}{2}\left(\frac{1}{1+\alpha}\right)^2\left(1+\frac{\alpha^2}{1+\alpha}\right)} \tag{6-2.3}$$

where $\alpha = h\nu/m_e c^2$.

The velocities of the scattering electrons in the carbon target cause a Doppler shift in the scattered photon energies [18] which results in broadening of the characteristic x-ray peaks. Matscheko and Ribberfors [10] developed a deconvolution method that reconstructs the characteristic peaks $\phi_1(h\nu)$ from the primary photon spectrum $\phi_0(h\nu)$. The method was implemented in our work as following, assuming 90° scattering:

$$\phi_1(h\nu) = \phi_0(h\nu) - \frac{T}{3m_e c^2}\left(\frac{\nu}{\nu'}\right)^2\left[\frac{\mathrm{d}^2\phi_0(h\nu)}{\mathrm{d}(h\nu)^2}\left[(h\nu)^2+(h\nu')^2\right] + 2h\nu\left(\frac{\mathrm{d}\phi_0(h\nu)}{\mathrm{d}(h\nu)}\right)\right] \tag{6-2.4}$$

where T is a measure of the mean kinetic energy of the bound electrons in the scatterer which is 0.101 keV for carbon [12]. As pointed out by the authors, the deconvolution is strongly dependent on derivatives of $\phi_0(h\nu)$ and therefore should be used only in energy intervals that contain the characteristic x-ray peaks. Thus, the deconvolution of the spectrum was applied in the bins with energies between 57 keV and 61 keV (K_α tungsten lines) and in the bins with energies between 66 keV and 70 keV (K_β lines). The unfolded primary spectrum is then the combination of the

primary spectrum $\phi_0(h\nu)$ calculated by equation 6-2.3 and the deconvolved spectrum $\phi_1(h\nu)$ at the position of the characteristic x-ray peaks.

6.2.2 Half-value layer measurements

Half-value layer (HVL_1) is the thickness of specified material (aluminum) that will reduce the air-kerma rate of a narrow beam of radiation to one-half of its initial value [19]. The second HVL (HVL_2) is the additional thickness of the absorber that attenuates the air-kerma rate to 25% of its initial value. HVL is a beam quality specifier that together with tube voltage and total filtration is often used to characterize diagnostic x-ray spectra. It was used in our work to determine the inherent filtration of the x-ray tube with the MC model, as the manufacturer specifies only a nominal thickness.

HVL_1 and HVL_2 on the central axis were determined by attenuation measurements of stationary x-ray tube using a PTW model 23342 parallel-plate chamber (Freiburg, Germany) and high purity 1 mm thick aluminum foils. The output of the x-ray tube was monitored by an Exradin A14 ionization chamber (Standard Imaging Inc, Middleton, WI).

6.2.3 MC simulation

The CT x-ray tube was modeled with the EGSnrc/BEAM Monte Carlo code [20]. The code includes an x-ray tube component module that was used for our simulation. The x-ray tube parameters were set according to the manufacturer's specifications.

CT specifications

The small $(0.4\times0.7)\,\mathrm{mm}^2$ and the large $(0.6\times1.3)\,\mathrm{mm}^2$ focal spots are produced by accelerated electrons striking a tungsten target. The x-ray tube offers high voltage potentials between 80 and 140 kV and tube currents between 30 mA to 300 mA. The anode has a 7° tilt and the anode heat is dissipated through a copper heat sink. The x-ray tube is evacuated. The inherent filtration due to the housing window is equivalent to a nominal thickness of 1.5 mm of aluminum according to the manufacturer's specifications. Additional 4.5 mm and 9.0 mm aluminum filtration is also available.

Head or body compensators can be used in order to account for non-uniform tissue thickness across the various exposed parts of the body and thus to achieve a more uniform beam intensity at the detector ring. Lead collimators define the field of view and slice thickness. The available slice thicknesses vary from 1 to 10 mm and the full and half field sizes are produced by a 38.4° and 19.2° fan beam, respectively.

Monte Carlo model

The x-ray tube was modeled according to the specifications (figure 6-2.3). The lead collimator was set to produce the full field size and 1 mm slice thickness. The inherent filtration of the x-ray tube was initially set to 1.5 mm of aluminum. However, due to deposition of tungsten on the tube window caused by tube aging [21], the inherent filtration increases with time. To account for tube aging and attenuation of the beam as it passes through various structures such as the tube window, the inherent filtration was iteratively modified until a good agreement with the HVL attenuation measurements was obtained. The simulated spectra were then compared to spectra measured with the CdTe detector.

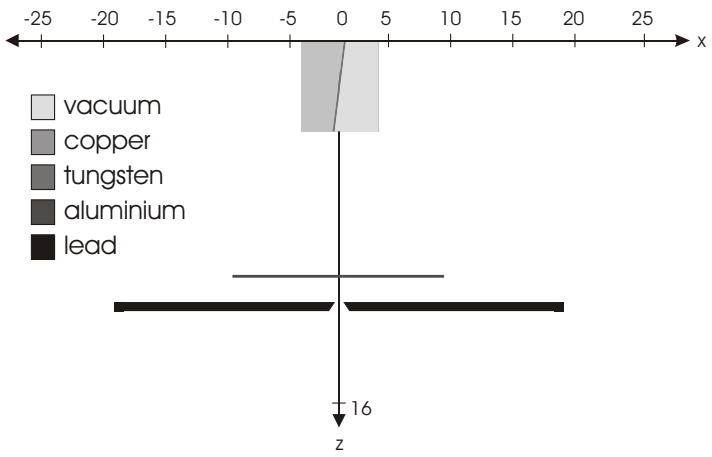

Figure 6-2.3: MC model of the CT x-ray tube.

All Monte Carlo simulations were run with 3×10^9 histories, the cut-off energies for electrons and photons were 20 and 10 keV, respectively. In order to obtain the correct number of photons in the characteristic x-ray peaks, the electron impact ionization process, which is by default off in the EGSnrc code, was on. Bound Compton scattering, Rayleigh scattering and atomic relaxations were also included in the simulations.

6.3 Results

6.3.1 Spectral measurements

Spectral measurements were performed for two tube voltages (100 and 140 kVp) and with and without the 9.0 mm aluminum filter. The spectral processing for the 140 kVp spectrum filtered by an additional 9.0 mm of aluminum is shown in figure 6-3.4.

The dashed line is the raw scattered spectrum acquired by the detector. The low energy tail (1-20 keV) is produced entirely by the spectrometer. The raw spectrum is corrected for detector response by the stripping method (dotted line). Note that the low energy tail produced by the detector disappeared. The crossed curve is created by applying the corrections based on the energy shift, the Klein-Nishina formula and the attenuation in air. Finally, the solid line corresponds to the primary x-ray tube spectrum. It is produced by deconvolution of the characteristic x-ray peaks of the crossed curve. The area under each curve is equal to unity.

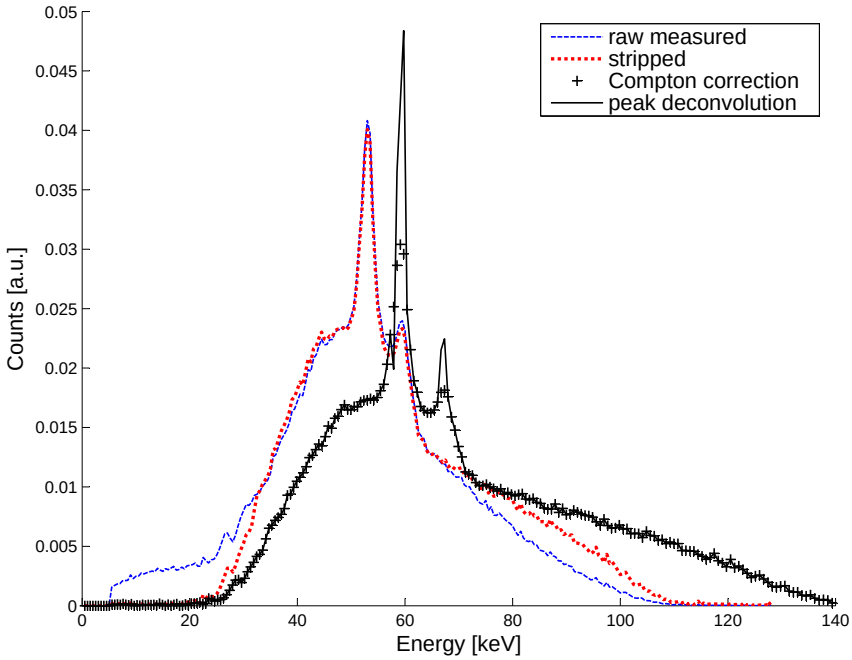

Figure 6-3.4: Spectral processing. Raw measured spectrum (dashed line), stripped spectrum corrected for detector response (dotted line). Spectrum corrected for Compton scatter with broad characteristic x-ray peaks due to Doppler shift (crosses) and with deconvolved characteristic peaks (solid line).

The spectrum corrections were subsequently applied to all acquired spectra and thus primary spectra were obtained for 100 kVp and 140 kVp with and without 9.0 mm aluminum filter.

6.3.2 HVL measurements

HVL measurements were carried out for 100 kV and 140 kV tube voltages with and without a 9.0 mm aluminum filter. HVL_1 and HVL_2 were iteratively determined on the basis of measured attenuation curves. The results are shown in table 6-3.1. HVL values were also iteratively calculated from the measured spectra, as done in the work by Verhaegen *et al.* [22]. The percentage differences from HVL values calculated from the measured spectra are also listed in table 6-3.1. All differences between HVL values determined from attenuation curves and calculated from measured spectra are within 4.6%.

Table 6-3.1: HVL values (in mm of aluminum) and percentage differences $(HVL_{PTW} - HVL_{CdTe})/HVL_{CdTe}$ as determined from attenuation measurements with a PTW chamber and as calculated from measured spectra with the CdTe detector. The values in the brackets are HVL values corrected for the PTW energy response.

		no additional filtration			additional 9.0 mm Al		
		PTW mm Al	CdTe mm Al	$diff_{PTW-CdTe}$ [%]	PTW mm Al	CdTe mm Al	$diff_{PTW-CdTe}$ [%]
100 kVp	HVL_1	3.67	3.73	-1.6	6.64 (6.57)	6.40	3.8 (2.7)
	HVL_2	5.91	5.83	1.4	8.05 (7.93)	7.87	2.3 (0.8)
140 kVp	HVL_1	5.57	5.51	1.1	8.70 (8.60)	8.32	4.6 (3.4)
	HVL_2	7.84	7.95	-1.4	10.58 (10.27)	10.18	3.9 (0.9)

As can be seen in table 6-3.1, the HVL values for the beams with additional 9 mm aluminum filtration determined by the attenuation measurement are consistently higher than the values calculated from the measured spectra. This can be explained

by the non-flat energy response of the ionization chamber. According to the NRC Calibration Report of the chamber, the reading for a 9.5 mm aluminum HVL beam is by 4% higher than the reading for a 3.0 mm HVL beam. When a correction for this was performed, assuming a linear energy response of the ionization chamber in the HVL range (6.49-11.07) mm aluminium, the values in the brackets given in table 6-3.1 were obtained. This leads to smaller differences with the HVL values derived from the CdTe spectrometer measurements, as indicated in the last column.

6.3.3 MC simulations

In order to complete the MC x-ray tube model as specified by the manufacturer, the inherent filtration had to be determined. First, it was set to 1.5 mm of aluminum and iteratively altered until a good agreement with HVL attenuation measurements for beams with no additional filtration was found. This process resulted in the value of 1.90 mm of aluminum. As can be seen from the third column of table 6-3.2 ($\text{diff}_{\text{MC-PTW}}$), 1.90 mm of aluminum leads to HVL differences smaller than 2.5%. The MC calculated spectra are also compared to the CdTe calculated spectra in table 6-3.2. The HVL values for beams with no additional filtration show a very good agreement, the differences are within 1.2%. The HVL values for beams filtered with additional 9 mm of aluminium are within 1.8%.

Once the inherent filtration of the x-ray tube is established, Monte Carlo simulated spectra can be compared to the measured spectra. The results are shown in figure 6-3.5. A good agreement between measurements and MC simulations was found. The largest discrepancies are observed for the non-filtered 100 kVp spectrum

Table 6-3.2: HVL values (in mm of aluminum) and percentage differences $(HVL_{MC}-HVL_{PTW})/HVL_{PTW}$ and $(HVL_{MC}-HVL_{CdTe})/HVL_{CdTe}$ as measured with the PTW chamber, as calculated from MC simulated spectra and as calculated from measured spectra with the CdTe spectrometer.

		no additional filtration					additional 9.0 mm Al		
		PTW mm Al	MC mm Al	$diff_{MC-PTW}$ [%]	CdTe mm Al	$diff_{MC-CdTe}$ [%]	CdTe mm Al	MC mm Al	$diff_{MC-CdTe}$ [%]
100 kVp	HVL_1	3.67	3.76	2.5	3.73	0.8	6.40	6.49	1.4
	HVL_2	5.91	5.76	-2.5	5.83	-1.2	7.87	7.80	-0.9
140 kVp	HVL_1	5.57	5.46	-2.0	5.51	-0.9	8.32	8.47	1.8
	HVL_2	7.84	8.03	2.4	7.95	1.0	10.18	10.15	-0.3

in the area where Bremsstrahlung radiation has its peak which can be partially explained by noise in the CdTe measurements. The tungsten K-lines measured by the detector have always lower intensity that the K-lines calculated by MC. This is primarily due to the energy resolution of the spectrometer that was measured to be 1.42 keV at 122 keV. However, the errors of total net areas of the characteristic peaks for the spectrometer measurements and MC simulations are within 20%.

MC simulated spectra were also compared to spectra calculated by the TASMIP program. Figure 6-3.6 shows the comparison for the 100 kVp spectrum with added filtration and for the 140 kVp without filtration. Similarly to the comparison of MC simulated spectra and measured spectra with the CdTe detector, the intensities of the TASMIP characteristic peaks are smaller than the intensities predicted by MC. This is due to the calculation resolution of TASMIP. In general, a very good agreement in determination of spectra between TASMIP and MC was found.

In conclusion, for purposes where only diagnostic x-ray spectra without spatial information are needed, the TASMIP program can be conveniently benefited from.

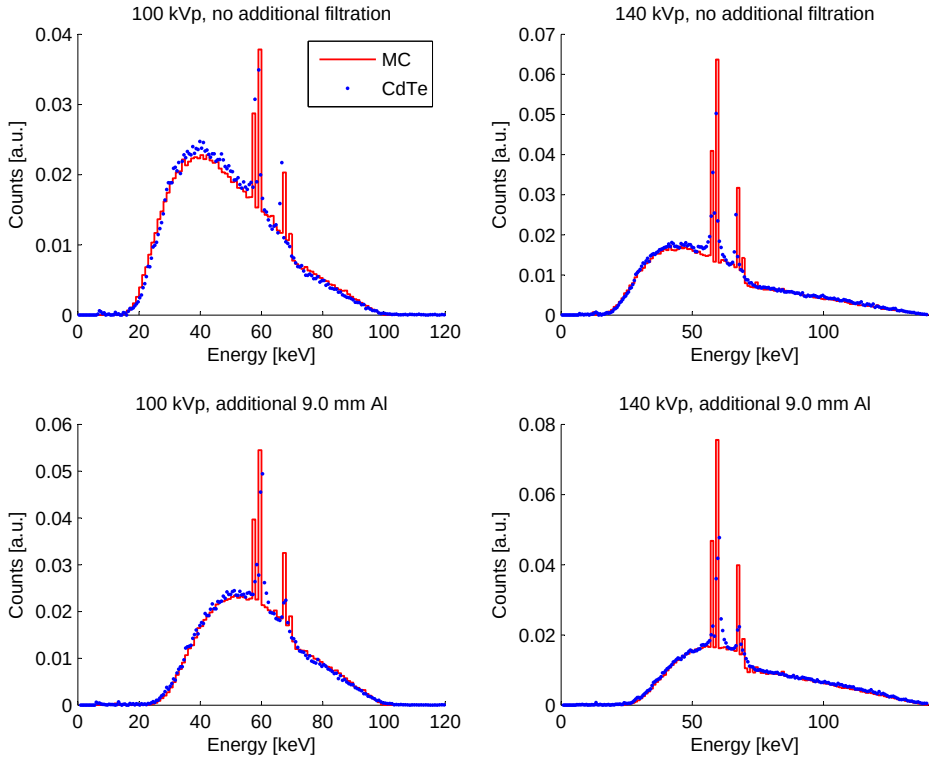

Figure 6-3.5: Comparison of spectra measured with CdTe detector (dotted curve) and simulated with Monte Carlo (full line). Area under each curve equals unity.

However, the TASMIP program cannot be used for Monte Carlo simulation of a CT scanner where high precision on photon fluence distribution or scatter distribution is required. The information on photon positions and directions can be calculated only by full MC simulation of the entire CT scanner geometry, including the x-ray tube.

6.4 Conclusions

A Monte Carlo model of a CT x-ray tube was validated by measurements of x-ray beams produced by two different tube voltages and filtrations. HVL_1 and HVL_2

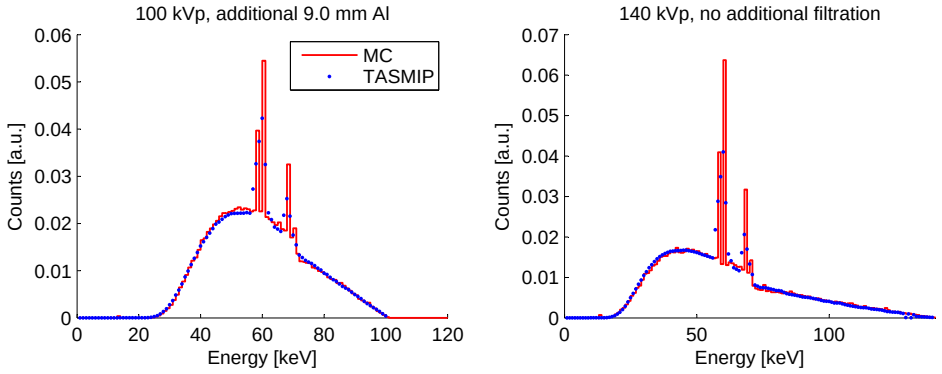

Figure 6-3.6: MC simulated spectra (full line) compared to TASMIP spectra (dotted curve).

for beams without additional filtration calculated from the MC modeled spectra and determined from attenuation measurements differ by less than 2.5%. The differences between HVL_1 and HVL_2 calculated from the MC modeled spectra and determined from spectral measurements with a CdTe detector are within 1.8%. The MC modeled spectra were directly compared to spectra measured by the CdTe detector and to spectra calculated by the TASMIP program and a good agreement was found.

We have created a Monte Carlo model of a CT x-ray tube. The model can be now completed by the compensator and the detector ring geometry and the dose delivered to the patients can be calculated by the Monte Carlo method. The model will also be helpful in understanding CT imaging processes and creation of CT artifacts.

A Monte Carlo model of a CT x-ray tube is presented in this chapter. The model is validated by spectral measurements with a CdTe detector and by half-value layer measurements. Spectral properties of CT x-ray tubes do not only affect the image quality but also directly influence the dose delivered to the patient during scanning. The Monte Carlo model of the CT x-ray tube can be used for:

- correction of metal artifacts by evaluating the scattered radiation, as described in the previous chapter,
- an accurate calculation of patient CT dose,
- dual-energy CT-based material extraction, as described in the next three chapters of the thesis.

Dual-energy CT-based (DECT) material extraction presents a novel method for more accurate mass density assignment and tissue segmentation, leading to improved Monte Carlo dose calculations. In our interpretation of DECT, spectral properties of CT x-rays have to be known with a reasonable accuracy. A method for an accurate determination of CT x-ray spectra was the topic of this chapter.

REFERENCES

[1] M.M. Rehani, G. Bongartz, S.J. Golding, L. Gordon, W. Kalender, T. Murakami, P. Shrimpton, R. Albrecht, and K. Wei. ICRP Publication 87: Managing patient dose in computed tomography. *Annals of the ICRP*, 30, 2002.

[2] D.J. Brenner. Is it time to retire the CTDI for CT quality assurance and dose optimization? *Med. Phys.*, 32:3225–3226, 2005.

[3] S. Mori, K. Nishizawa, M. Ohno, and M. Endo. Conversion factor for CT dosimetry to assess patient dose using a 256-slice CT scanner. *Brit. J. Radiol.*, 79:888–892, 2006.

[4] J.J. DeMarco, C.H. Cagnon, D.D. Cody, D.M. Stevens, C.H. McCollough, J. O'Daniel, and M.F. McNitt-Gray. A Monte Carlo based method to estimate radiation dose from multidetector CT (MDCT): cylindrical and anthropomorphic phantoms. *Phys. Med. Biol.*, 50:3989–4004, 2005.

[5] M.S. Nogueira, H.C. Mota, and L.L. Campos. (HP) Ge Measurement of spectra for diagnostic X-Ray beams. *Rad. Prot. Dos.*, 111:105–110, 2004.

[6] C.S. Chen, K. Doi, C. Vyborny, H.P. Chan, and G. Holje. Monte Carlo simulation studies of detectors used in the measurement of diagnostic x-ray spectra. *Med. Phys.*, 7:627–635, 1980.

[7] M. Bhat, J. Pattison, G. Bibbo, and M. Caon. Diagnostic x-ray spectra: A comparison of spectra generated by different computational methods with a measured spectrum. *Med. Phys.*, 25:114–120, 1998.

[8] S. Miyajima. Thin CdTe detector in diagnostic x-ray spectroscopy. *Med. Phys.*, 30:771–777, 2003.

[9] M. Yaffe, K.W. Taylor, and H.E. Johns. Spectroscopy of diagnostic x rays by a Compton-scatter method. *Med. Phys.*, 3:328–334, 1976.

[10] G. Matscheko and R. Ribberfors. A Compton scattering spectrometer for determining x-ray photon energy spectra. *Phys. Med. Biol.*, 32:577–594, 1987.

[11] G. Matscheko and G.A. Carlsson. Compton spectroscopy in the diagnostic X-ray energy range: I. Spectrometer design. *Phys. Med. Biol.*, 34:199–208, 1989.

[12] G. Matscheko, G.A. Carlssoni, and R. Ribberfors. Compton spectroscopy in the diagnostic x-ray energy range. II. Effects of scattering material and energy resolution. *Phys. Med. Biol.*, 34:199–208, 1989.

[13] K. Maeda, M. Matsumoto, and A. Taniguchi. Compton-scattering measurement of diagnostic x-ray spectrum using high-resolution Schottky CdTe detector. *Med. Phys.*, 32:1542–1547, 2005.

[14] J.M. Boone and J.A. Seibert. An accurate method for computer-generating tungsten anode x-ray spectra from 30 to 140 kV. *Med. Phys.*, 24:1661–1670, 1997.

[15] T.R. Fewell, R.E. Shuping, and K.R. Hawkins. Handbook of Computed Tomography X-Ray Spectra. *NTIS, SPRINGFIELD, VA, 1981, 112*, 1981.

[16] S.M. Seltzer. Calculated response of intrinsic germanium detectors to narrow beams of photons with energies up to 300 keV. *Nucl. Instrum. Methods*, 188:133–51, 1981.

[17] B.R.B. Walters and D.W.O. Rogers. DOSXYZnrc Users Manual. *NRCC Report No. PIRS 794 rev B*, 2007.

[18] R. Ribberfors. Relationship of the relativistic Compton cross section to the momentum distribution of bound electron states. *Physical Review B*, 12:2067–2074, 1975.

[19] C.W. Coffey, L.A. DeWerd, C. Liu, R. Nath, S.M. Seltzer, and J.P. Seuntjens. AAPM protocol for 40–300 kV x-ray beam dosimetry in radiotherapy and radiobiology. *Med. Phys.*, 28:868–893, 2001.

[20] D.W.O. Rogers, B.A. Faddegon, G.X. Ding, C.M. Ma, J. Wei, and T.R. Mackie. BEAM: A Monte Carlo code to simulate radiotherapy treatment units. *Med. Phys*, 22:503–524, 1995.

[21] H.D. Nagel. Limitations in the determination of total filtration of X-ray tube assemblies. *Phys. Med. Biol.*, 33:271–89, 1988.

[22] F. Verhaegen, A.E. Nahum, S. Van de Putte, and Y. Namito. Monte Carlo modelling of radiotherapy kV x-ray units. *Phys. Med. Biol.*, 44:1767–1789, 1999.

CHAPTER 7
Tissue segmentation in Monte Carlo treatment planning: a simulation study using dual-energy CT images

Dual-energy CT (DECT) is a relatively well known method for calculation of the effective atomic number and the relative electron density of a material scanned with two energies. In this thesis, DECT was newly applied as an alternative method for assignment of CT numbers to mass densities and tissue types for Monte Carlo dose calculations. The difference in attenuation coefficients measured with two different tube voltages is transformed into the effective atomic number (Z) and relative electron density (ρ_e) of each voxel. Both Z and ρ_e are then used for the novel tissue segmentation scheme. On the other hand, the conventional method for tissue segmentation using a single-energy CT image is exclusively based on differences in ρ_e. Therefore, an improved material segmentation is expected for tissues with similar ρ_e and different Z, such as soft tissue and soft bone.

The accuracy of DECT material extraction strongly depends on the spectral properties of the two x-ray beams used for scanning. In this chapter, published in *Radiotherapy and Oncology*, spectral properties of x-ray beams used for DECT are investigated solely by means of Monte Carlo simulations. The effect of the improved tissue segmentation using Z differences of tissue-equivalent materials is demonstrated with an orthovoltage photon beam dose calculation.

Authors: M. Bazalova, J.-F. Carrier, L. Beaulieu and F. Verhaegen

Published in: *Radiotherapy and Oncology* **86** 93-98, 2008

Abstract

Tissue segmentation is an important step in Monte Carlo (MC) dose calculation and is often done uncritically. A new approach to tissue segmentation using dual-energy CT images is studied in this work. A simple MC model of a CT scanner was built and CT images of phantoms with ten tissue-equivalent cylinders were simulated using soft and hard x-ray spectra. The Z and ρ_e of the cylinders were extracted using a formalism based on a parameterization of the linear attenuation coefficient. It was shown that in order to extract Z and ρ_e with a reasonable accuracy, hard x-ray beams have to be used for scanning. When an additional filtration of 9 mm of aluminum in the CT x-ray beam is used, beam hardening in high density materials is suppressed and the mean errors of the extraction of Z and ρ_e for 10 tissue-equivalent materials in a small tissue-equivalent phantom are 3.7% and 3.1% respectively. MC simulations were used to show that the extraction of Z and ρ_e for a number of tissue-equivalent materials using dual-energy CT images is possible which improves tissue segmentation for Monte Carlo dose calculations, as demonstrated with a 250 kVp photon beam dose calculation.

7.1 Introduction

The use of Monte Carlo (MC) techniques for radiotherapy is increasing which is reflected in the literature [1–3]. MC dose calculations using codes such as the

EGSnrc/DOSXYZnrc are sensitive to the method of conversion from computed tomography (CT) images to mass density (ρ) and material maps. The common approach to assigning mass densities to CT numbers (or Hounsfield units, HU), is based on (HU, ρ) calibration curves. Subsequently, each material type is assigned to a predefined HU range, based on the same calibration curve. It has been shown that this approach can lead to inaccurate conversion resulting in dose calculation errors, up to 10% for 6 MV and 15 MV photon beams for a set of NaCl and $CaCl_2$ solutions when the default DOSXYZnrc/CTCREATE calibration is used [4]. In this work, a novel method for tissue segmentation using dual-energy CT-based material extraction is employed.

Table 7-1.1 lists ten tissue-equivalent materials with their relative electron densities ρ_e[a] , effective atomic numbers Z[b] and mass densities ρ. As shown in the table, some materials have very similar ρ and ρ_e but their Z differ significantly. Materials number 3, 4 and 5 represent an example. It would be difficult to distinguish these materials when only the information about their ρ_e was available. However, the information about Z of these materials certainly makes it possible to tell them apart. This is illustrated in figure 7-1.1 which shows a 2D (Z, ρ_e) plot for a set of RMI (Gammex, Middleton, WI) tissue-equivalent materials listed in table 7-1.1. Note

[a] $\rho_e = (\rho Z/A)/(\rho_w Z_w/A_w)$, where A is the atomic mass of a material and ρ_w, Z_w,and A_w are the mass density, the atomic number and the atomic mass of water

[b] $Z = (\sum_i w_i Z_i^{3.5})^{1/3.5}$ where w_i is fraction by weight of element i with atomic number Z_i [5]

that all materials are well separated. The additional information on Z of each pixel is used for an improved tissue segmentation using a (Z, ρ_e) calibration.

Table 7-1.1: Ten RMI tissue-equivalent materials, their effective atomic numbers Z, relative electron densities ρ_e and mass densities ρ.

#	MATERIAL	ρ_e	Z	ρ [g/cm^3]
1	lung(LN300)	0.292	7.864	0.300
2	lung(LN450)	0.438	7.835	0.450
3	AP6 adipose	0.902	6.404	0.920
4	polyethylene	0.945	5.740	0.920
5	CT Solid Water	0.986	8.111	1.015
6	B200 Bone Mineral	1.097	10.897	1.145
7	CB2 - 10% CaCO3	1.142	8.905	1.170
8	CB2 - 30% CaCO3	1.286	11.393	1.340
9	CB2 - 50% CaCO3	1.470	12.978	1.560
10	SB3 Bone, Cortical	1.692	14.141	1.819

Rutherford *et al.* [6] showed in 1976 that if CT images of an object are acquired at two significantly different tube voltages, Z and ρ_e of the object can be determined. The algorithm for extracting Z and ρ_e is based on a parameterization of the linear attenuation coefficient (μ), introduced by Jackson and Hawkes [5], using the effective energies of two x-ray beams. The method developed by Rutherford *et al.* was later modified by Torikoshi *et al.* [7, 8] for monochromatic x-rays.

In this paper, the algorithm developed by Torikoshi *et al.* was modified for polychromatic x-rays. The new algorithm was tested using MC simulations of a CT scanner. CT images of phantoms with various tissue-equivalent materials were calculated for two x-ray beam energies and Z and ρ_e were determined by the new method. The agreement between the extracted and true Z and ρ_e was quantified.

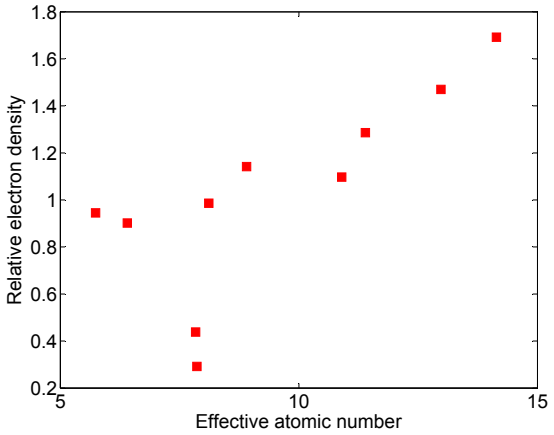

Figure 7-1.1: Plot of ρ_e versus the Z for ten tissue-equivalent materials used for a 2D (Z,ρ_e) tissue segmentation.

Provided this method works, more accurate MC dose calculations may be feasible which is demonstrated in the last section of this paper. Moreover, the MC model of a CT scanner can be used for optimization of the voltages and filtrations of the two x-ray beams used for scanning. As a result, the best performance of a dual-energy CT scanner can be obtained.

7.2 Materials and methods

The algorithm for dual-energy CT-based material extraction for polychromatic x-rays is presented in this work. The algorithm description is followed by the Z and ρ_e extraction of ten tissue-equivalent materials calculated from μ-maps. The μ-maps are obtained from MC simulations of a CT scanner.

7.2.1 Dual-energy CT-based material analysis

The dual-energy CT-based material extraction method developed by Torikoshi *et al.* [7, 8] was modified in this work. The $\mu(Z,\ \rho_{\mathrm{e}})$ of a material with Z and ρ_{e} measured at two different tube voltages can be expressed by

$$\mu_j = \rho_e \sum_i \omega_{ji} \left[Z^4 F(E_{ji}, Z) + G(E_{ji}, Z) \right], \tag{7-2.1}$$

$j = 1, 2$, assuming the two x-ray spectra are represented by weights ω_{ji} corresponding to energy E_{ji}, where $\sum_i \omega_{ji} = 1$, for $j = 1, 2$. $\rho_{\mathrm{e}} Z^4 F(E, Z)$ and $\rho_{\mathrm{e}} G(E, Z)$ are the photoelectric absorption and the combined Rayleigh and Compton scattering terms of the linear attenuation coefficient obtained by fitting of data from the NIST database [9], respectively.

If two μs of a material measured at two tube voltages are known, then Z of the material can be obtained by solving the following equation:

$$\frac{\mu_1}{\mu_2} - \frac{\sum_i \omega_{1i} \left[Z^4 F(E_{1i}, Z) + G(E_{1i}, Z) \right]}{\sum_i \omega_{2i} \left[Z^4 F(E_{2i}, Z) + G(E_{2i}, Z) \right]} = 0. \tag{7-2.2}$$

ρ_{e} can be obtained by inserting Z back into equation 7-2.1. The presented algorithm has to be slightly modified for extracting Z and ρ_{e} directly from CT images where HU are represented by HU = $1000(\mu/\mu_{\mathrm{w}}\text{-}1)$ and μ_{w} is the linear attenuation coefficient of water which has to be included in the analysis.

7.2.2 Monte Carlo simulations

A MC model of a CT scanner was built using the EGSnrc/BEAM code [10] and a modified version of the EGSnrc/DOSXYZnrc code [11]. The x-ray tube and the

imaging detectors were modeled based on manufacturer's specifications of a PQ5000 CT scanner (Royal Philips Electronics, Eindhoven, the Netherlands) in BEAM. The 100 kVp and 140 kVp x-ray beams were shaped by a pair of lead jaws into either a 19.2° or a 3.1° fan beam according to the required size of the field of view (FOV). The inherent filtration of the x-ray tube is 1.9 mm Al. Simulations were done with either no or 9 mm Al additional filtration. Due to the shift in the mean energies of the filtered beams, the beams filtered with 1.9 mm and 10.9 mm of Al will be denoted as soft and hard beams, respectively. The slice thickness was 1 cm in all geometries.

The geometry of the simulations is shown in figure 7-2.2. Figure 7-2.2a represents a simulation where only one small uniform cylinder is scanned in air using a small FOV, with a 3.1° fan beam. The x-ray source is represented by the phase-space file from the x-ray tube simulations (phsp1) and is randomly rotated over 200° in 1° intervals. The phase-space files (phsp1) were used for simulations of the CT geometry in the modified version of the DOSXYZnrc code. The photons interact in the cylinder and are scored in one of the 128 $(29\times4\times0.945)\,\mathrm{mm}^3$ $CdWO_4$ detectors of a curved phase-space file (phsp2) representing a detector ring. The detector energy response was simulated in the DOSXYZnrc code. The energy response was taken into account in the CT simulation by convolving the photon energy in each detector with the detector response. In this way, a 128×200 intensity matrix I of each cylinder was created. In order to obtain the projection matrix $p = -\ln(I/I_0)$, I_0, the source intensity at the detector ring, was obtained by simulating a scan with only air between

the x-ray source and the detectors. Simulations with ten cylinders made of tissue-equivalent materials listed in table 7-1.1 were performed for soft and hard beams for 100 and 140 kVp.

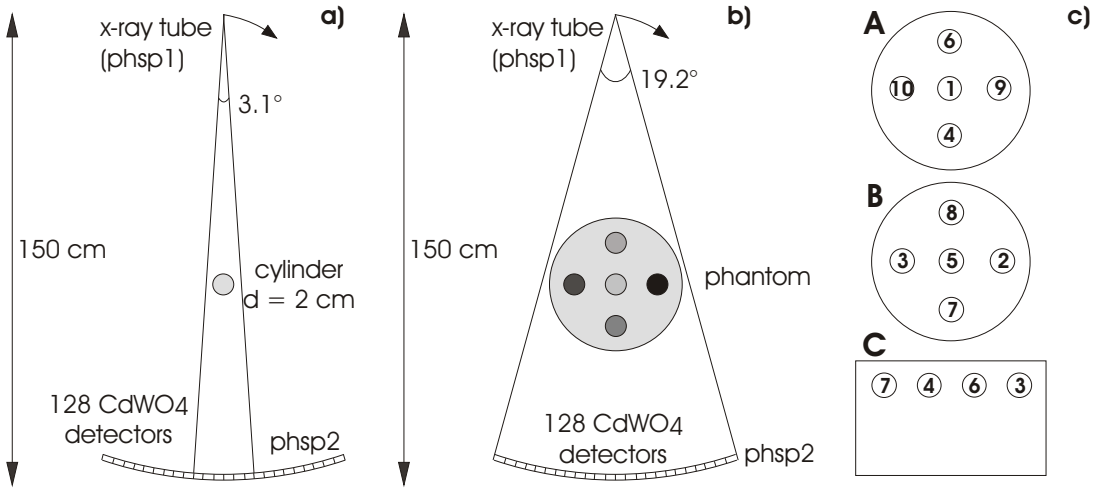

Figure 7-2.2: The setup for MC calculations of CT images of small cylinders made of tissue-equivalent materials scanned in air (a) and in a solid water phantom (b). Phantom A, B and C geometries (c), the materials are listed in table 7-1.1.

Figure 7-2.2b shows the setup for a phantom with 5 cylindrical inserts. Simulations were performed with two solid water phantoms (figure 7-2.2c) with 13.6 cm in diameter. The phantom diameter requires a larger FOV, therefore a new phsp1 with a 19.2° fan beam was created. The simulation parameters are the same as in the case of the simulations with the single cylinders, resulting in 128×200 matrices of projections. CT images for 10 cylinders in air and the phantoms A and B at soft and hard 100 kVp and 140 kVp beams were reconstructed from matrices of projections in Matlab (The Mathworks, Natick, MA). A filtered-back projection (FBP) with

the Shepp-Logan filter was used because nearly all of the reconstruction algorithms employed by commercial CT scanners are based on FBP [12].

7.2.3 MC dose calculations

MC dose calculations were performed for a 250 kVp photon beam in phantom C (figure 7-2.2c). The kilovoltage photon beam was chosen to emphasize the problem and it is representative for errors that might be encountered in assessing dose in kV radiotherapy, CT scanning and brachytherapy. The phantom was created on the basis of the simulated cylinders in images of phantoms A and B. Only four cylinders with low HU contrast (<14%) were used in phantom C. Subsequently, phantom C was converted into a material and density map for MC dose calculations. This was done in two different ways. First, the simulated 100 kVp HU map of the phantom was used to assign material types. This represents the commonly used approach to material segmentation (the single-energy CT material segmentation). Since a (ρ, HU) calibration curve was not available and the exact geometry was known, mass densities were assigned on the basis of the exact geometry mass density. Secondly, a novel dual-energy CT material segmentation was employed on the basis of the extracted ρ_e and Z-maps. The mass density of each voxel was assigned on the basis of the extracted ρ_e and a linear relationship between ρ and ρ_e from table 7-1.1.

MC dose calculations were performed for a single 250 kVp photon beam in three MC geometries: in the exact know geometry (D_{ex}), in the single-energy CT geometry (D_{single}) and in the dual-energy CT geometry (D_{dual}). The statistical uncertainty in dose calculations was less than 0.2% in high dose regions.

7.3 Results

7.3.1 In-air simulations

The results of the extraction of Z and ρ_e for cylinders made of 10 tissue-equivalent materials scanned in air are presented in figure 7-3.3. The simulations using soft beams (crosses) show an overestimation of the extracted ρ_e and an underestimation of the extracted Z for high density materials. The mean errors of the extraction of Z and ρ_e using the soft beams are 8.4% and 4.3%, respectively. A remarkable beam hardening within these cylinders was observed which caused the inaccuracy of the extraction Z and ρ_e. The mean energy of the soft beams is relatively low and the spectrum changes substantially as the beams pass through high density materials. The significant change in the spectra makes dual-energy material segmentation inaccurate [13]. While the effects of beam hardening are well known for single-energy CT images, to our knowledge, the effect on dual-energy material extraction for a large range of tissue equivalent materials has not yet been studied in detail.

The effect of beam hardening can be suppressed when hard spectra are used. The mean energy of the hard beams is higher and therefore the increase is relatively smaller when the beams pass through the cylinders. The improvement of the extraction of both Z and ρ_e is evident in figure 7-3.3 where the circles lie closer to the diagonal. The errors of the extraction of Z and ρ_e using the hard beams are in the range from -9.8% to 6.0% and from -3.5% to 3.3% with the mean errors of 4.5% and 1.6%, respectively.

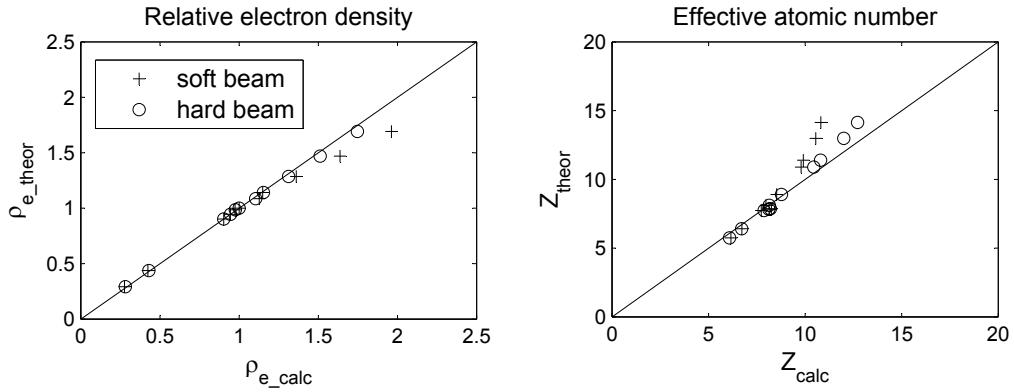

Figure 7-3.3: The extracted ρ_e and Z of 10 tissue-equivalent materials scanned in air. The results for soft beam simulations (crosses) and hard beam simulations (circles) are shown.

7.3.2 Phantom simulations

In order to evaluate the effect of beam hardening within a heterogeneous phantom consisting of tissue equivalent materials, simulations with cylinders embedded in two small phantoms were performed. The simulated CT image for phantom A using the hard 140 kVp spectrum is presented in figure 7-3.4.

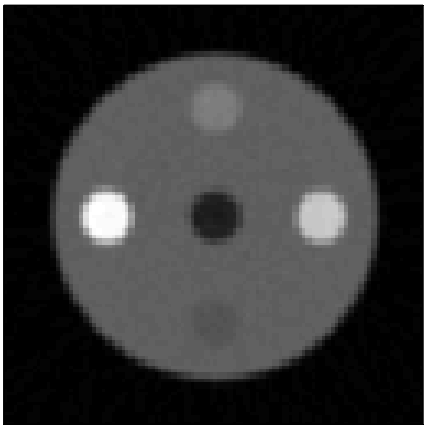

Figure 7-3.4: MC simulated CT image of phantom A.

The results for the extraction of Z and ρ_e are shown in figure 7-3.5. Whereas the ρ_e are extracted with a good accuracy for both soft and hard beams, the extracted Z using the soft beams deviate from the diagonal. The mean errors on the extraction of ρ_e for soft and hard beams are 4.5% and 3.1%, respectively. Note that the beam hardening caused by the solid water phantom also affects the extraction of Z for lower-Z materials, such as lung and solid water.

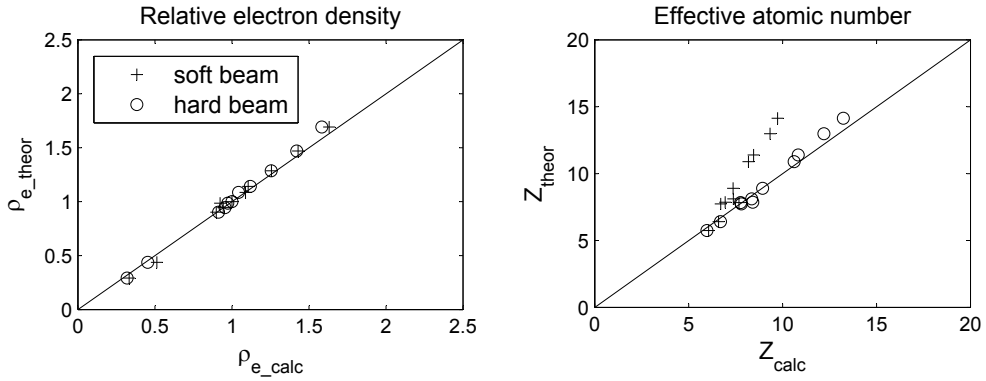

Figure 7-3.5: The extracted ρ_e and Z of 10 tissue-equivalent materials scanned in a phantom. The results for soft beam simulations (crosses) and hard beam simulations (circles) are shown.

The extraction of Z was more accurate when the hard beams were used for the simulations. As a result the mean error for the extraction of Z decreases from 15.6% for the soft beams to 3.7% for the hard beams.

7.3.3 MC dose calculations

It was found that the MC simulated images were fairly noisy, despite the relatively long calculation time (30 hours on a 2.8 GHz machine). The noise in a water phantom was 15 HU which is significantly higher than in real scanners ($\sim$5 HU). As a result, the noise was artificially removed from μ-maps by replacing each material

by its mean μ. The simulated 'noise-free' 100 kVp CT image of phantom C and the reconstructed ρ_e and Z-maps are shown in figure 7-3.6a-c. Note that noise in CT images is an important issue for dual-energy CT based material extraction which was discussed by other authors [14].

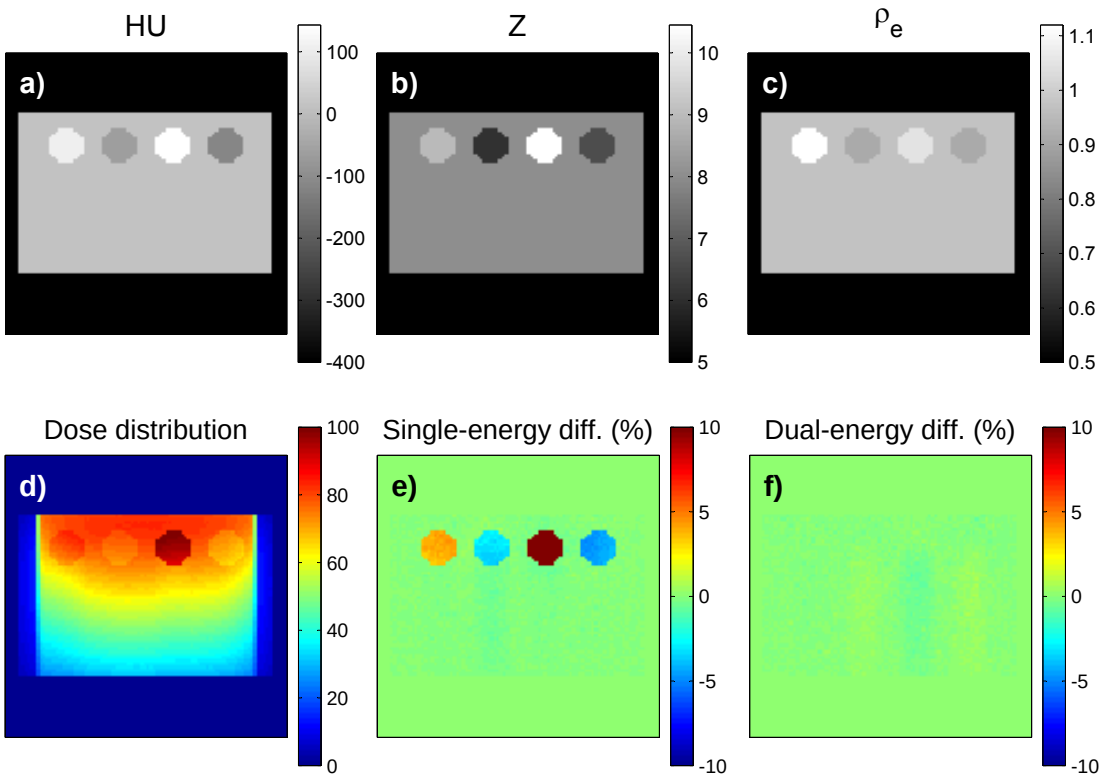

Figure 7-3.6: Simulated 'noise-free' CT image of phantom C (a), its extracted Z (b) and ρ_e-map (c). The exact dose distribution with a single 250 kVp photon beam (d) and the dose differences from the exact dose distribution (D_{ex}-D_{single}/D_{ex}) and (D_{ex}-D_{dual}/D_{ex}) using single-energy CT (e) and dual-energy CT (f) material segmentation, respectively.

To demonstrate the need for an accurate material segmentation, four cylinders with low contrast were chosen for MC dose calculation. The low contrast in the CT

image (figure 7-3.6a) results in mis-assignment of all cylinders to solid water. On the other hand, the contrast of the cylinders is higher (>18%) in the Z-map (figure 7-3.6b) which allows for their accurate segmentation using the novel dual-energy CT approach.

Dose calculations results for a single 250 kVp photon beam are summarized in figure 7-3.6d-f. Figure 7-3.6d shows the normalized dose distribution whereas figure 7-3.6e and 7-3.6f represent dose differences from the exact geometry for dose calculations using the single-energy CT and the dual-energy CT material segmentation, respectively. The dose differences in the mis-assigned cylinders are up to 17%, 5%, 4.5% and 4% for BONE200, AP6, CB2-10% $CaCO_3$ and polyethylene respectively. This is caused by the differences in the mass energy absorption coefficients (μ_{en}/ρ) of solid water and the cylinder materials for the 250 kVp photon beam. The dose differences are below 1% when the dual-energy CT material segmentation was implemented.

7.4 Conclusions

We have used Monte Carlo simulations to show that the extraction of effective atomic numbers and relative electron densities for a number of tissue-equivalent materials using dual-energy CT images is possible. A simple MC model of a CT scanner was built and CT images of cylinders in air and in solid water phantoms with cylinders were simulated using soft and hard x-ray spectra. The Z and ρ_{e} of the cylinders were extracted using a formalism based on a parameterization of the linear attenuation coefficient.

It was shown that in order to extract effective atomic numbers and relative electron densities with a reasonable accuracy, hard beams have to be used for scanning. When no additional filtration to the CT x-ray beam is used, significant beam hardening in high density materials occurs and the mean errors of the extraction of Z and ρ_e for ten tissue-equivalent materials in a small tissue-equivalent phantom are 15.6% and 4.5% respectively. When an additional thickness of 9 mm of aluminium is inserted in the beam, beam hardening is suppressed and the mean errors of the extraction of Z and ρ_e decrease to 3.7% and 3.1%, respectively. Since most clinical CT scanning is done with hard beams, this result will potentially be sufficient for improved tissue segmentation for Monte Carlo dose calculations.

Monte Carlo dose calculations for a 250 kVp photon beam were performed using the conventional single-energy CT material segmentation and the novel dual-energy CT material segmentation. It was found that four low contrast cylinders could not be correctly segmented using the conventional approach due to their HU being similar to the HU of surrounding solid water. This mis-assignment results in dose calculation errors up to 17% in the 250 kVp photon beam. However, using the novel dual-energy tissue segmentation, dose calculation errors are within 1%.

Materials with high contrast in CT images, such as bone and lung tissue equivalent materials, can be segmented with a reasonable accuracy and therefore large dose calculation errors in photon beams are not expected. For MV photon beams, where the main interaction type (the Compton effect) is independent of Z, smaller dose calculation errors are expected for any mis-assigned media. On the other hand, in

high energy MV photon beams (such as a 25 MV beam) pair production becomes important which might result in larger dose calculation errors in inaccurately assigned materials. Ongoing work is being performed to investigate experimental phantoms and a wider range of dose calculations for different treatment modalities.

Monte Carlo simulations of a CT scanner presented in this chapter show that beam hardening is an important effect in dual-energy CT-based material extraction based on the parameterization of the linear attenuation coefficient. Therefore, in order to minimize beam hardening, hard spectra should be used for DECT.

An improvement of a photon beam dose calculation compared to the conventional dose calculation using a single-energy CT image was demonstrated. A MC simulation for four tissue-equivalent materials with similar electron densities but different atomic numbers irradiated with an orthovoltage photon beam was performed. Whereas the dose was calculated accurately on the basis of DECT, significant dose errors for all four materials using the conventional material segmentation were seen.

REFERENCES

[1] N. Reynaert, S.C. van der Marck, D.R. Schaart, W. Van der Zee, C. Van Vliet-Vroegindeweij, M. Tomsej, J. Jansen, B. Heijmen, M. Coghe, and C. De Wagter. Monte Carlo treatment planning for photon and electron beams. *Radiation Physics and Chemistry*, 76:643–686, 2007.

[2] M.F. Tsiakalos, S. Stathakis, G.A. Plataniotis, C. Kappas, and K. Theodorou. Monte Carlo dosimetric evaluation of high energy vs low energy photon beams in low density tissues. *Radiother. Oncol.*, 79:131–138, 2006.

[3] S. Spirydovich, L. Papiez, V. Moskvin, and P. Desrosiers. Evaluation of underdosage in the external photon beam radiotherapy of glottic carcinoma: Monte Carlo study. *Radiother. Oncol.*, 78:159–164, 2006.

[4] F. Verhaegen and S. Devic. Sensitivity study for CT image use in Monte Carlo treatment planning. *Phys. Med. Biol.*, 50:937–946, 2005.

[5] H.E. Johns and J.R. Cunningham. *The physics of radiology.* Springfield, Illinois, fourth edition, 1983.

[6] R.A. Rutherford, B.R. Pullan, and I. Isherwood. Measurement of Effective Atomic Number and Electron Density Using an EMI Scanner. *Neuroradiology*, 11:15–21, 1976.

[7] M. Torikoshi, T. Tsunoo, M. Sasaki, M. Endo, Y. Noda, Y. Ohno, T. Kohno, K. Hyodo, K. Uesugi, and N. Yagi. Electron density measurement with dual-energy x-ray CT using synchrotron radiation. *Phys. Med. Biol.*, 48:673–685, 2003.

[8] T. Tsunoo, M. Torikoshi, Y. Ohno, M. Endo, M. Natsuhori, T. Kakizaki, N. Yamada, N. Ho, N. Yagi, and K. Uesugi. Measurement of electron density and effective atomic number using dual-energy X-ray CT. *Nuclear Science Symposium Conference Record, 2004 IEEE*, 6, 2004.

[9] M.J. Berger, J.H. Hubbell, S.M. Seltzer, J. Chang, J.S. Coursey, R. Sukumar, and D.S. Zucker. XCOM: Photon Cross Section Database (version 1.3). *National Institute of Standards and Technology (NIST), Gaithersburg, MD*, 2005.

[10] D.W.O. Rogers, B.A. Faddegon, G.X. Ding, C.-M. Ma, J. We, and T.R. Mackie. BEAM: A Monte Carlo code to simulate radiotherapy treatment units. *Med. Phys.*, 22:503–524, 1995.

[11] G. Jarry, S.A. Graham, D.J. Moseley, D.J. Jaffray, J.H. Siewerdsen, and F. Verhaegen. Characterization of scattered radiation in kV CBCT images using Monte Carlo simulations. *Med. Phys.*, 33:4320–4329, 2006.

[12] J. Hsieh, E. Chao, J. Thibault, B. Grekowicz, A. Horst, S. McOlash, and T.J. Myers. A novel reconstruction algorithm to extend the CT scan field-of-view. *Med. Phys.*, 31:2385–2391, 2004.

[13] M.M. Goodsitt. Beam hardening errors in post-processing dual energy quantitative computed tomography. *Med. Phys.*, 22:1039–1047, 1995.

[14] F. Kelcz, P.M. Joseph, and S.K. Hilal. Noise considerations in dual energy CT scanning. *Med. Phys.*, 6:418–425, 1979.

CHAPTER 8
Dual-energy CT-based material extraction for tissue segmentation in Monte Carlo dose calculations

The improvement of Monte Carlo dose calculations using dual-energy CT was demonstrated by simulations of a CT scanner in the previous chapter. In this chapter, CT images of a tissue-equivalent phantom are acquired on a clinical CT scanner. As explained in the previous chapter, both x-ray beams are filtered with a 9 mm aluminum filter, i.e. hard x-ray beams are used for DECT scanning.

The proposed material segmentation for MC dose calculations using DECT is tested with a number of treatment beams. Since the novel tissue segmentation is based on differences in effective atomic numbers (Z) of human tissues, improvement in dose calculation results is mainly expected for kilovoltage x-ray beams. The photoelectric effect, strongly dependent on Z, is significant for kilovoltage beams, therefore, neglecting Z differences of tissues is expected to result in dose calculations errors. In this chapter, published in *Physics in Medicine and Biology*, kilovoltage and megavoltage photon and megavoltage electron beam MC simulations are performed on a tissue equivalent phantom. The effect of the novel tissue segmentation compared to the conventional tissue segmentation is evaluated and the importance for human tissues treated with photon and electron beams is discussed.

Authors: M. Bazalova, J.-F. Carrier, L. Beaulieu and F. Verhaegen

Published in: *Physics in Medicine and Biology* **53** 2439-2456, 2008

Abstract

Monte Carlo (MC) dose calculations are performed on patient geometries derived from computed tomography (CT) images. For most available MC codes, the Hounsfield Units (HU) in each voxel of a CT image have to be converted into mass density (ρ) and material type. This is typically done with a (HU; ρ) calibration curve which may lead to mis-assignment of media. In this work, an improved material segmentation using dual-energy CT-based material extraction is presented. For this purpose, the differences in extracted effective atomic numbers Z and the relative electron densities ρ_e of each voxel are used. Dual-energy CT material extraction based on parameterization of the linear attenuation coefficient for 17 tissue-equivalent inserts inside a solid water phantom was done. Scans of the phantom were acquired at 100 kVp and 140 kVp from which Z and ρ_e values of each insert were derived. The mean errors on Z and ρ_e extraction were 2.8% and 1.8%, respectively. Phantom dose calculations were performed for 250 kVp and 18 MV photon beams and an 18 MeV electron beam in the EGSnrc/DOSXYZnrc code. Two material assignments were used: the conventional (HU; ρ) and the novel (HU; ρ, Z) dual-energy CT tissue segmentation. The dose calculation errors using the conventional tissue segmentation were as high as 17% in a mis-assigned soft bone tissue-equivalent material for the 250 kVp photon beam. Similarly, the errors for the 18 MeV electron beam and the 18 MV photon beam were up to 6% and 3% in some mis-assigned media. The assignment

of all tissue-equivalent inserts was accurate using the novel dual-energy CT material assignment. As a result, the dose calculation errors were below 1% in all beam arrangements. Comparable improvement in dose calculation accuracy is expected for human tissues. The dual-energy tissue segmentation offers a significantly higher accuracy compared to the conventional single-energy segmentation.

8.1 Introduction

Monte Carlo (MC) techniques can be used to calculate dose delivered to patients receiving radiotherapy. In Monte Carlo treatment planning (MCTP) using codes such as the EGSnrc/DOSXYZnrc [1, 2], patient computed tomography (CT) scans have to be converted into voxel geometries where each voxel is represented by its mass density (ρ) and tissue type. However, the conversion is not a trivial procedure and it has been shown that inaccurate tissue segmentation can lead to large dose calculation errors, up to 10% for 6 MV and 15 MV photon beams using the default DOSXYZnrc/CTCREATE ramp when not properly implemented [3].

Various authors published studies on conversion of CT images into mass densities. Schneider *et al.* [4] described a method to determine improved CT calibrations for biological tissue, a stoichiometric calibration, based on measurements using tissue equivalent materials. Schneider *et al.* [5] simplified the stoichiometric calibration by introducing interpolation functions in the calibration procedure and were able to derive a non-affine relationship between CT numbers and elemental weights. More recently, Vanderstraeten *et al.* [6] evaluated the stoichiometric calibration in a multicenter study. They obtained dose to water calculation errors up to 10% when multiple bone types were ignored.

Du Plessis *et al.* [7] published a study in which they evaluated the number of tissue types that are needed to calculate the dose at a 1% dose accuracy level for an 8 MV photon beam. They found that 57 tissue subsets are required to represent 16 main tissue types. Some MC-based systems use many tissue types, e.g. the VCU DOSXYZnrc-based MC system [8] uses 56 bins.

Due to the large number of tissue subsets that have to be segmented in patient CT images, mis-assignment of media could occur. All mentioned studies made use of single-energy CT scans of patients or phantoms. The purpose of this study is to improve the commonly used material segmentation by employing dual-energy CT material extraction.

An alternative method to conversion of CT images into MC geometry file is the approach used in VMC/XVMC codes where CT numbers are mapped to mass densities and then continuous mass density to scattering property functions are used. The commercial VMC++ implementation by Nucletron which uses 22 tissue-bins [9] is an example. Such an approach has the potential to suffer much less from inadequate CT to material conversion.

8.2 Materials and Methods

8.2.1 Description of the problem

The conventional approach to the conversion of CT numbers (or Hounsfield Units, HU) involves scanning a set of tissue-equivalent materials and creating a (HU; ρ) calibration curve. HU are defined as HU = $1000(\mu/\mu_{\mathrm{w}}\text{-}1)$ where μ and μ_{w} are the linear attenuation coefficients of a material and water, respectively. An example of a calibration curve created using a set of RMI electron density calibration

materials (Gammex, Middleton, WI, see table 8-2.1) is shown in figure 8-2.1. Material segmentation, done by assigning HU ranges to tissue types, is indicated by the dashed vertical lines.

Table 8-2.1: ρ_e, Z, ρ and elemental composition by weight of 17 RMI tissue-equivalent materials. Data supplied by the manufacturer.

#	MATERIAL	ρ_e	Z	ρ g/cm^3	H	C	N	O	Mg	Si	P	Cl	Ca
1	LUNG(LN300)†	0.292	7.864	0.300	8.5	59.4	2.0	18.1	11.2	0.8		0.1	
2	LUNG(LN450)†	0.438	7.835	0.450	8.5	59.6	2.0	18.1	11.2	0.6		0.1	
3	AP6 ADIPOSE	0.902	6.404	0.920	9.1	72.3	2.3	16.3				0.1	
4	POLYETHYLENE(PE)	0.945	5.740	0.920	14.4	85.6							
5	BR12 BREAST	0.957	7.236	0.980	8.6	70.1	2.3	17.9				0.1	1.0
6	SOLID WATER(SW)	0.986	8.111	1.015	8.0	67.3	2.4	19.9				0.1	2.3
7	LV1 RMI	1.010	8.114	1.039	8.1	67.0	2.5	20.0				0.1	2.3
8	CB3 RESIN	1.020	6.662	1.020	11.3	74.2	1.6	12.0				0.9	
9	SR2 BRAIN	1.045	6.311	1.049	10.8	72.5	1.7	14.9				0.1	
10	IB3 INNER BONE	1.086	10.895	1.133	6.7	55.6	2.0	23.5			3.2	0.1	8.9
11	B200 BONE MINERAL	1.097	10.897	1.145	6.6	55.5	2.0	23.6			3.2	0.1	8.9
12	CB4	1.124	6.468	1.155	8.2	70.2	2.7	18.8				0.1	
13	CB2 - 10% $CaCO_3$	1.142	7.905	1.170	8.6	65.3	2.7	19.2				0.1	4.0
14	ACRYLIC(LUCITE)	1.147	6.704	1.180	8.1	60.0		32.0					
15	CB2 - 30% $CaCO_3$	1.286	11.393	1.340	6.7	53.5	2.1	25.6				0.1	12.0
16	CB2 - 50% $CaCO_3$	1.470	12.978	1.560	4.8	41.6	1.5	32.0				0.1	20.0
17	SB3 BONE CORTICAL	1.692	14.141	1.819	3.4	31.4	1.8	36.5				0.0	26.8

† Both lung materials have very similar elemental composition and therefore for MC dose calculations, they were assigned to a single material type with different densities.

From figure 8-2.1, a number of questions related to the assignment of mass densities and tissue types using the conventional (HU; ρ) approach arise. Specifically, several steps of the procedure are not well defined:

- how is the calibration curve created (e.g. how many linear segments should be used)?
- which tissue-equivalent materials are suitable for calibration?
- where should the boundaries between tissue types be set?

The aim of this work is to simplify or overcome the listed problems using dual-energy CT-based material extraction.

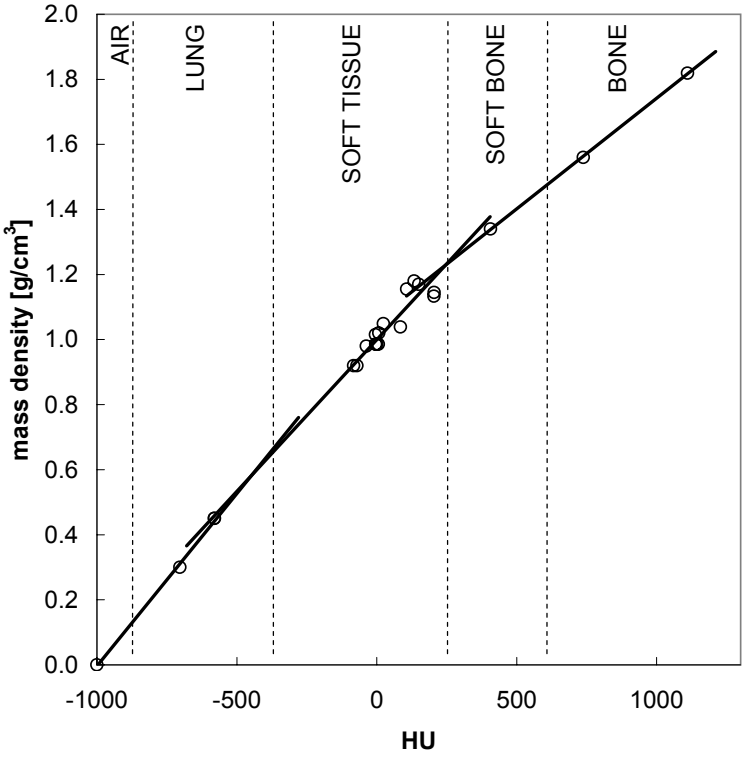

Figure 8-2.1: A typical (HU; ρ) calibration curve used for conversion of HU into mass densities and material types.

The CT dual-energy technique involves scanning an object with two significantly different tube voltages and results in conversion of the measured HU into the effective atomic numbers Z[a] and the relative electron densities ρ_e[b] of each voxel.

---

[a] $Z = (\sum_i w_i Z_i^{3.5})^{1/3.5}$ where w_i is fraction by weight of element i with atomic number Z_i [10]

[b] $\rho_e = \rho'_e/(\rho'_e)_w = (\rho Z/A)/(\rho_w Z_w/A_w)$, where ρ'_e and $(\rho'_e)_w$ are the electron densities of a material and water, A is the atomic mass of a material and ρ_w, Z_w,and A_w are the mass density, the atomic number and the atomic mass of water

Conveniently for MC dose calculations, the ρ_e-maps can be directly converted into ρ-maps using a linear relationship. This way, the above listed difficulties regarding ρ assignment using the (HU; ρ) calibration curve are avoided. The Z-maps can then be used for an improved material segmentation by taking advantage of Z differences for tissues or materials having a similar ρ. For this purpose, Z and ρ have to be determined with a reasonably high accuracy.

The concept of determination of Z and ρ_e from dual-energy CT scans was introduced by Rutherford *et al.* [11] and further developed by Heismann *et al.* [12]. The latter work presented a ρZ projection algorithm which allowed Z and ρ extraction of a set of chemical solutions with Z varying from 7.21 to 9.84 and ρ in the range from 0.910 to 1.219. The errors on Z extraction using this method were up to 5%. Rizescu *et al.* [13] developed their own method for dual-energy material extraction and built a CT scanner with an ^{192}Ir source emitting reported principle gamma radiation of 310.5 and 469.1 keV. They were able to extract Z with an error less than 3% and 10% for $Z > 25$ and $Z < 15$, respectively. The error on ρ determination was less than 3%. Torikoshi *et al.* [14] and Tsunoo *et al.* [15] presented a method for dual-energy CT-based material extraction using monochromatic x-rays. In our paper, this method was modified for polychromatic x-rays which made it suitable for the use in clinical CT scanners and therefore more practical for treatment planning.

8.2.2 Dual-energy CT-based material extraction

As stated in the paper by Torikoshi *et al.* [14], the linear attenuation coefficient (μ) of a material at energy E can be approximated with:

$$\mu(E) = \rho'_{\mathrm{e}} \left(Z^4 F(E,Z) + G(E,Z) \right), \tag{8-2.1}$$

where ρ'_{e} is the electron density of the material and $\rho_{\mathrm{e}} Z^4 F(E,Z)$ and $\rho_{\mathrm{e}} G(E,Z)$ are the photoelectric and combined Rayleigh and Compton scattering terms of the linear attenuation coefficient. The functions $F(E,Z)$ and $G(E,Z)$ are obtained by quadratic fits of the photoelectric and scattering terms of NIST attenuation coefficients [16]. Figure 8-2.2 shows and example of $F(E,Z)$ and $G(E,Z)$ functions for 50 keV and 100 keV photons. The NIST data are also plotted.

The attenuation coefficient μ_j of a material scanned with a continuous energy spectrum j (the index j =1, 2 depends on the spectrum used for the dual energy scanning) can then be calculated by:

$$\mu_j = \rho'_{\mathrm{e}} \sum_i \omega_{ji} \left[Z^4 F(E_{ji}, Z) + G(E_{ji}, Z) \right], \tag{8-2.2}$$

where the spectrum j is represented by a spectral distribution ω_{ji} at energy E_{ji}. Assuming two linear attenuation coefficients of a material (μ_1 and μ_2) are measured by two significantly different spectra (100 and 140 kVp in our work), then two different evaluations of equation 8-2.2 are available that can be solved iteratively for Z. After that, ρ'_{e} is calculated by inserting Z back into equation 8-2.2, for either $j = 1$ or $j = 2$.

Attenuation coefficients of materials can be measured in a CT scanner where they are represented by HU = 1000(μ/μ_{w}-1). If two scans with two different spectra j are taken, the ratios $\mu_j/\mu_{j\mathrm{w}}$ = HU$_j$/1000+1 for j = 1, 2 are known. Therefore, the method for Z and ρ_{e} calculation has to be slightly modified by incorporating

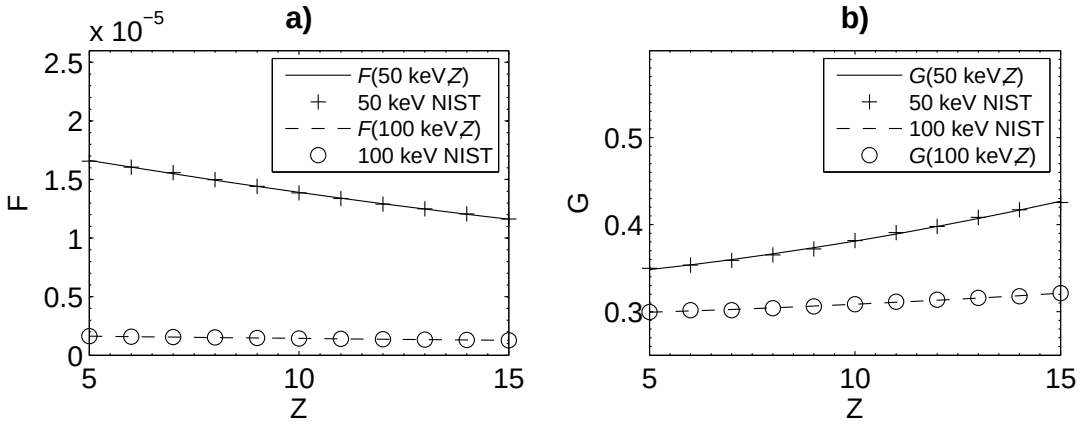

Figure 8-2.2: $F(E,Z)$ (a) and $G(E,Z)$ (b) functions (lines) for 50 keV and 100 keV photons created by fitting NIST data (symbols).

the linear attenuation coefficient of water for spectra 1 and 2 ($\mu_{1\mathrm{w}}$ and $\mu_{2\mathrm{w}}$) into equation 8-2.2. Note that the Z of water according to the definition used here is Z_{w} = 7.733. Finally, the equation that has to be solved to determine the Z of a material is:

$$Z^4 - \frac{\frac{\mu_2}{\mu_{2\mathrm{w}}}\sum_i \omega_{2i}\left[Z_{\mathrm{w}}^4 F(E_{2i},Z_{\mathrm{w}}) + G(E_{2i},Z_{\mathrm{w}})\right]\sum_i \omega_{1i}G(E_{1i},Z_{\mathrm{w}}) - \frac{\mu_1}{\mu_{1\mathrm{w}}}\sum_i \omega_{1i}\left[Z_{\mathrm{w}}^4 F(E_{1i},Z_{\mathrm{w}}) + G(E_{1i},Z_{\mathrm{w}})\right]\sum_i \omega_{2i}F(E_{2i},Z_{\mathrm{w}}) - \frac{\mu_1}{\mu_{1\mathrm{w}}}\sum_i \omega_{1i}\left[Z_{\mathrm{w}}^4 F(E_{1i},Z_{\mathrm{w}}) + G(E_{1i},Z_{\mathrm{w}})\right]\sum_i \omega_{2i}G(E_{2i},Z_{\mathrm{w}})}{-\frac{\mu_2}{\mu_{2\mathrm{w}}}\sum_i \omega_{2i}\left[Z_{\mathrm{w}}^4 F(E_{2i},Z_{\mathrm{w}}) + G(E_{2i},Z_{\mathrm{w}})\right]\sum_i \omega_{1i}F(E_{1i},Z_{\mathrm{w}})} = 0, \tag{8-2.3}$$

The relative electron density is then calculated from (for either j):

$$\rho_{\mathrm{e}} = \frac{\mu_j}{\mu_{j\mathrm{w}}} \frac{\sum_i \omega_{ji} \left[Z_{\mathrm{w}}^4 F(E_{ji}, Z_{\mathrm{w}}) + G(E_{ji}, Z_{\mathrm{w}}) \right]}{\sum_i \omega_{ji} \left[Z^4 F(E_{ji}, Z) + G(E_{ji}, Z) \right]}, \tag{8-2.4}$$

A Matlab (The Mathworks, Natick, MA) routine was developed that iteratively solves equation 8-2.3. The inputs to the program are the two CT photon spectra (spectral distributions ω_{ji} for the 100 and 140 kVp spectra corrected for beam hardening, see the next subsection), the measured HU at the two tube voltages and NIST attenuation coefficients for elements with Z from 5 to 15 which is the range of effective atomic numbers of the materials used in our study.

Correction for beam hardening

Beam hardening in CT is an important effect for dual-energy material extraction. As any polyenergetic x-ray beam passes through a material, low energy photons are attenuated more than high energy photons which causes a shift of the mean energy of the spectrum toward higher energies and 'hardening' of the spectrum. Especially when employing the dual-energy CT-based material extraction on large objects, beam hardening has to be taken in account by using 'tissue filtered' spectra rather than the original x-ray tube spectra.

The HU of each voxel is a representation of the linear attenuation coefficient at the effective energy of the spectrum at the location of the voxel. However, at each position of the x-ray tube, the path length of the ray passing through a particular voxel from the surface of the phantom to the voxel is different. As a result, the effective energy at a voxel is different for each x-ray tube position and the final

reconstructed HU of the voxel corresponds to the mean value of ρ calculated for all x-ray tube positions.

In the phantom study, we found out that the shape and the mean energy of the original x-ray tube spectrum changes considerably when the x-ray beam passes through 32 cm of solid water (the size of the RMI phantom used in the study and an approximate size of adult pelvis). For the 9 mm added aluminum filtration 100 and 140 kVp beams, the mean beam energy changes from 60 keV to 70 keV and from 71 keV to 90 keV, respectively. Since the mean distance from each voxel of a cylindrical phantom to the surface of the phantom can be approximated by the radius of the phantom, the spectra used for the dual-energy material extraction algorithm were the measured 100 and 140 kVp spectra filtered with 16 cm of solid water. Beam hardening in high-Z materials is even more pronounced and it also had to be taken into account in the material extraction analysis. A semi-empirical correction was developed which is described in the Result section.

For MCTP, mass densities not electron densities have to be input for each voxel. A linear relationship between ρ and ρ_e was found by fitting the data for the set of RMI materials listed in table 8-2.1. The linear fit was found to be ρ=1.079ρ_e-0.050 with an R^2 value larger than 0.995.

8.2.3 Spectral measurements

In order to solve equations 8-2.3 and 8-2.4, the spectral distributions ω_{ji} for the 100 and 140 kVp spectra have to be known. The original spectra were measured with a high resolution Schottky CdTe detector (XR-100T, AMPTEK Inc, Bedford, MA) in a Compton scatter setup. Details can be found in Bazalova and Verhaegen [17].

Finally, the 16 cm solid water filtered spectral distributions ω_{ji} were calculated by MC, using the EGSnrc/BEAM code [18].

Heismann *et al.* [12] proposed to include the CT scanner detector response in the spectra. We simulated the response of the detectors used in our CT scanner by impinging monoenergetic photons on the center of $(29\times4\times0.945)\,\mathrm{mm}^3$ $CdWO_4$ crystals. The detector response was then incorporated in our analysis by multiplying each bin of the response with the original x-ray spectra. It was found, however, that the detector response has a negligible effect on the dual-energy material extraction. As a result, the detector response was not taken into account in this paper.

8.2.4 Phantom

A 32 cm diameter solid water RMI electron density calibration phantom with 20 cylindrical inserts made of 17 tissue-equivalent materials (table 8-2.1) was scanned at 100 and 140 kVp in a single-slice CT scanner (Picker PQ5000, Royal Philips Electronics, Eindhoven, the Netherlands). Additional filtration of 9 mm of aluminum was used for both x-ray beam energies in order to minimize beam hardening effects for dual-energy material extraction, as described in Bazalova *et al.* [19]. The RMI cylinders are made of materials with Z in the range between 5.740 for polyethylene and 14.141 for cortical bone. ρ_e of the inserts vary from 0.292 for inflated lung to 1.692 for cortical bone. Note that the Z and ρ_e ranges of the RMI materials approximately correspond to the Z and ρ_e ranges of ICRU-44 tissues [20]. According to ICRU-44, Z of human tissues varies from 6.559 for yellow marrow to 13.978 for cortical bone and ρ_e varies from 0.258 for inflated lung to 1.781 for cortical bone.

The arrangement of the cylinders in the phantom as recommended by the manufacturer and as it was used for material extraction is shown in figure 8-2.3 (phantom A). The mean HU of each insert of both 100 kVp and 140 kVp images were calculated and input into equation 8-2.3 in the form of μ_1/μ_{1w} and μ_2/μ_{2w}, respectively. The extracted Z and ρ_e were then compared to the known values.

8.2.5 Dose calculations

The RMI electron density phantom was also used for MC dose calculations using the EGSnrc/DOSXYZnrc code. Since the number of materials in a DOSXYZnrc geometry file is currently limited to nine[c] and the phantom is made of solid water and surrounded by air, only 7 different material types could be placed in the phantom. Note that due to their elemental composition similarity, the two lung materials were considered to be one material type with different density. The RMI insert arrangements for a single 18 MeV electron and 250 kVp photon beam dose calculations (phantom B) and 6 and 18 MV parallel-opposed photon beam dose calculations (phantom C) are shown in figure 8-2.3. The beam field size for the 18 MeV and 250 kVp dose calculations was 26×8 cm and it was 8×8 cm for the 6 MV and 18 MV photon beam simulations. Whereas the inserts for the MV photon beam dose calculations are placed in the center of the phantom, they are rearranged toward the surface of the phantom for electron and kilovoltage photon beam dose calculations.

[c] The number of materials can in principle be increased. The modification requires changes to the EGSnrc/DOSXYZ code where the geometry files are read in and to the software that creates the phantom voxel geometry.

The RMI materials with the lowest and the highest Z and ρ were among those chosen for the dose calculation study. The photon and electron spectra were taken from previous work [3].

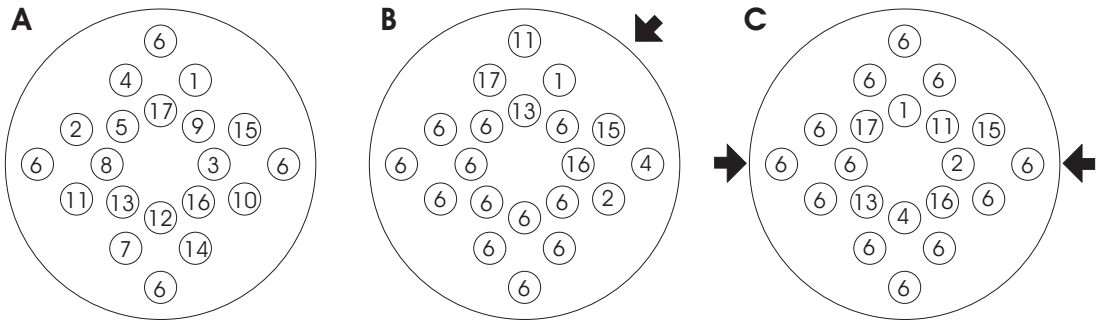

Figure 8-2.3: The geometry of the solid water RMI phantom with 17 different tissue-equivalent inserts for material extraction (phantom A). Phantom geometry for MC dose calculations using an orthovoltage 250 kVp photon beam and an 18 MeV electron beam (phantom B) and using 6 and 18 MV photon beams (phantom C). Medium 6 is the phantom material, solid water. The directions of the beams are indicated by the arrows.

First, the 512×512 CT images of the phantoms were resampled to 256×256 matrices. The conversion from HU to mass densities and materials was done in two different ways: applying the (HU; ρ) conventional approach using a single-energy CT image and a calibration curve and employing the novel (HU; ρ, Z) approach that uses dual-energy CT images and reconstructed Z and ρ_e of each voxel. The latter approach does not require a calibration curve. Finally, 3D phantoms were created by extending the single 2D CT slice of 5 mm into 10 cm. Dose calculations were performed with DOSXYZnrc in the single-energy CT geometry (D_{single}), in the

dual-energy CT geometry (D_{dual}) and in the voxelized exact-known geometry (D_{ex}) of each phantom.

8.3 Results

8.3.1 Single-energy CT material segmentation

The conventional approach for conversion of CT images into mass densities and materials uses a (HU; ρ_{e}) calibration curve which was created as follows. First, phantom A (figure 8-2.3 left) with 20 tissue-equivalent inserts was scanned at 140 kVp. Then ρ_{e} of the inserts versus the measured HU were plotted and the calibration curve was obtained by fitting three linear segments (shown in figure 8-3.4a). The mass densities of each voxel of the 140 kVp scans of phantom B and C (figure 8-2.3 center and 8-2.3 right) were obtained on the basis of the measured HU, the calibration curve and the (ρ, ρ_{e}) relationship. Subsequently, the phantom CT images were segmented into materials using HU ranges according to table 8-3.2a. Note that the solid water (SW) region HU [-320:220] is naturally derived from the intersection points of the calibration curve segments (as depicted in figure 8-3.4a). The four media in the solid water bin have similar HU and were therefore assigned a single material type.

8.3.2 Dual-energy CT material segmentation

Both 100 and 140 kVp images of phantoms B and C were processed by dual-energy material extraction on a pixel-by-pixel basis resulting in 256×256 Z and ρ_{e}-maps of the phantoms. Unlike in the conventional approach where a calibration curve was required, mass densities were assigned on the basis of the ρ_{e}-maps using only the (ρ, ρ_{e}) relationship. No calibration curve was needed.

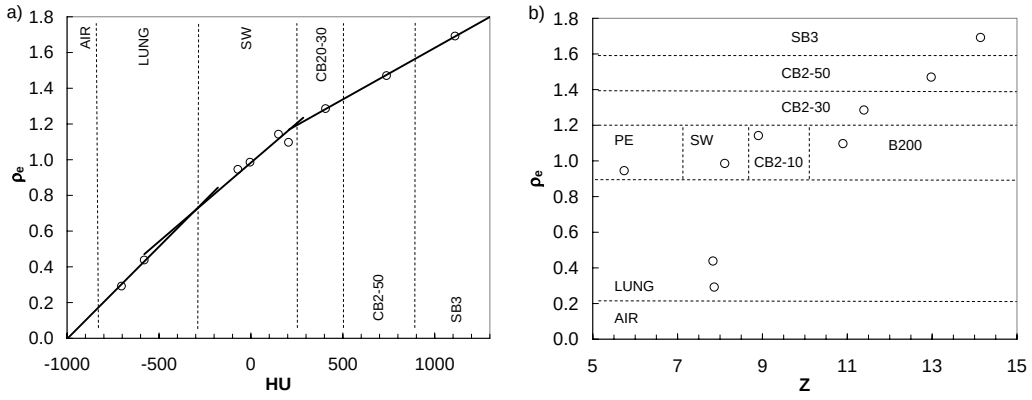

Figure 8-3.4: Tissue segmentation for MC dose calculations in phantoms B and C using single-energy CT images (a) and dual-energy CT images (b).

Both Z and ρ_e-maps were then used for the novel (HU; ρ, Z) tissue segmentation for MC dose calculations as demonstrated in figure 8-3.4b. Each rectangle in the figure corresponds to one material type. The Z and ρ_e ranges of each material type are listed in table 8-3.2b. Note that the four materials (PE, SW, CB2-10, B200), which were assigned to only one material type in the single-energy CT approach, are here separated using their differences in Z. The boundaries in the Z direction were chosen approximately at the center between two neighboring materials.

8.3.3 Material extraction of 17 RMI tissue-equivalent materials

CT scans of phantom A taken at 100 and 140 kVp were processed by the Matlab routine using the 16 cm solid water filtered spectra. The ρ_e and Z of the 17 RMI tissue-equivalent materials were extracted and plotted in figure 8-3.5. As can be seen in the figure, the extracted ρ_e for three high-Z materials are underestimated due to beam hardening effects. From these points, a semi-empirical correction for beam

Table 8-3.2: HU ranges for material segmentation for MC dose calculations using single-energy CT images (a) and ρ_e and Z ranges for material segmentation using dual-energy CT images (b).

a)

	HU
AIR	[-1000 : -950]
LUNG	[-950 : -320]
SW	[-320 : 220]
CB2-30	[220 : 500]
CB2-50	[500 : 900]
SB3	[900 : 1500]

b)

	ρ_e	Z
AIR	[0 : 0.2]	[5 : 15]
LUNG	[0.2 : 0.9]	[5 : 15]
PE	[0.9 : 1.2]	[5 : 7]
SW	[0.9 : 1.2]	[7 : 8.5]
CB2-10	[0.9 : 1.2]	[8.5 : 10]
B200	[0.9 : 1.2]	[10 : 15]
CB2-30	[1.2 : 1.4]	[5 : 15]
CB2-50	[1.4 : 1.6]	[5 : 15]
SB3	[1.6 : 1.8]	[5 : 15]

hardening effects in high-Z materials was derived. ρ_e for materials with $Z > 10$ were corrected using the following equation: $(\rho_e)_{cor} = 1.6953\rho_e$-0.7432.

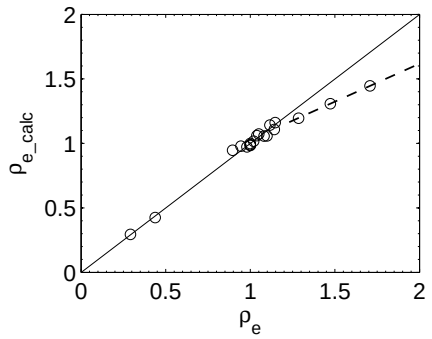

Figure 8-3.5: Calculated ρ_e versus actual ρ_e for 17 RMI tissues. Beam hardening in three high-Z materials causes underestimation of calculated ρ_e. Correction for beam hardening is derived from the dashed line fit.

The results with the correction for beam hardening are presented in figure 8-3.6 where the extracted ρ_e and Z versus the known ρ_e and Z are plotted. Figure 8-3.6 shows good agreement between the extracted ρ_e and Z values and the known

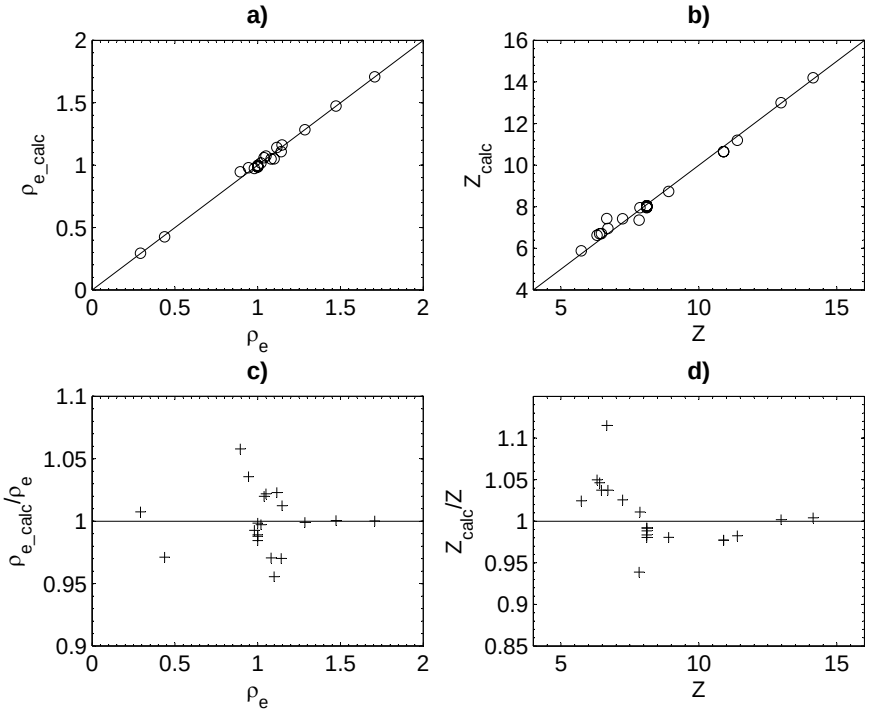

Figure 8-3.6: Calculated and known relative electron densities ρ_e (a) and effective atomic numbers Z (b) of materials included in the RMI electron density CT phantom. The ratios of calculated to known ρ_e and Z are shown in (c) and (d).

values. The mean error of the extraction of ρ_e and Z is (1.8±1.6)% and (2.8±2.6)%, respectively. The largest error (12% in Z) was obtained for the CB3 resin material. We suspect, however, that the insert might have changed its composition in time. The results from figure 8-3.6 are encouraging and therefore the dual-energy CT-based material extraction was used for tissue assignment for MC dose calculations. The mean HU of each material used in this study are listed in table 8-3.3.

Table 8-3.3: The mean HU and standard deviations (σ) of 17 RMI materials scanned at 100 kVp and 140 kVp and 400 mAs.

		100 kVp		140 kVp	
#	MATERIAL	mean HU	σ	mean HU	σ
1	LUNG (LN300)	-703	23	-704	28
2	LUNG (LN450)	-582	11	-580	12
3	AP6 ADIPOSE	-94	12	-82	12
4	POLYETHYLENE (PE)	-90	10	-71	11
5	BR12 BREAST	-41	11	-37	10
6	SOLID WATER (SW)	0	10	-5	9
7	LV1 RMI	90	11	85	11
8	CB3 RESIN	3	9	7	11
9	SR2 BRAIN	14	12	25	12
10	IB3 INNER BONE	267	11	204	11
11	B200 BONE MINERAL	267	12	205	11
12	CB4	93	10	107	11
13	CB2 - 10% $CaCO_3$	168	10	150	11
14	ACRYLIC (LUCITE)	122	11	133	10
15	CB2 - 30% $CaCO_3$	496	11	406	11
16	CB2 - 50% $CaCO_3$	924	13	738	12
17	SB3 BONE CORTICAL	1399	17	1110	15

8.3.4 Dose calculations for 250 kVp photon and 18 MeV electron beams

CT images of phantom B were taken at 100 kVp and 140 kVp (figure 8-3.7a) and processed by a Matlab routine which resulted in ρ_e and Z-maps of 256×256 voxels (figure 8-3.7b and 8-3.7c). Note that the faint streaking artifacts between the two high density inserts in the CT image (lightest color CB2 - 50% $CaCO_3$ and SB3) are still present in the Z-map but they vanished in the ρ_e-map. Also note the grainy character of the Z-map, mainly in the two lung tissue-equivalent cylinders (darkest color). This is explained by volume averaging artifacts of the porous lung inserts [12].

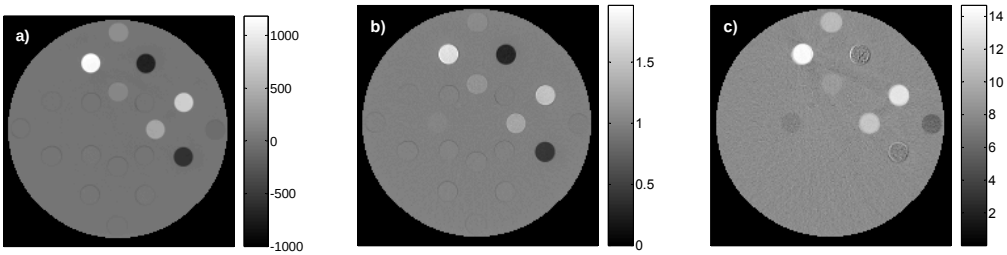

Figure 8-3.7: 140 kVp CT image (a), ρ_e-map (b) and Z-map (c) for phantom B.

MC dose calculations for a 250 kVp photon beam and an 18 MeV electron beam were performed in phantom B. The two material segmentations using the single-energy CT and dual-energy CT approach were done on the basis of table 8-3.2a and b, respectively. The exact geometry, the single-energy CT and dual-energy CT geometry results are summarized in figure 8-3.8a-c. Three inserts (polyethylene, CB2-10% $CaCO_3$ and B200) could not be assigned correctly on the basis of the (HU; ρ_e) calibration curve. On the other hand, the material assignment using the additional information on Z of each voxel is more accurate, leaving only a few voxels incorrectly assigned, mostly due to volume averaging artifacts at the edges of the inserts.

The exact dose distributions, with the known materials and densities assigned to the cylinders, are presented in figure 8-3.9a and 8-3.9d. The dose calculation errors for the 250 kVp photon beam are presented in figure 8-3.9b and 8-3.9c. In the single-energy CT geometry, the incorrectly assigned B200 insert has dose calculation errors as large as +17% which is explained by the large difference in the mass energy absorption coefficients μ_{en}/ρ of B200 and solid water. The dose calculation errors in the polyethylene and CB2-10% $CaCO_3$ inserts caused by incorrect assignments are

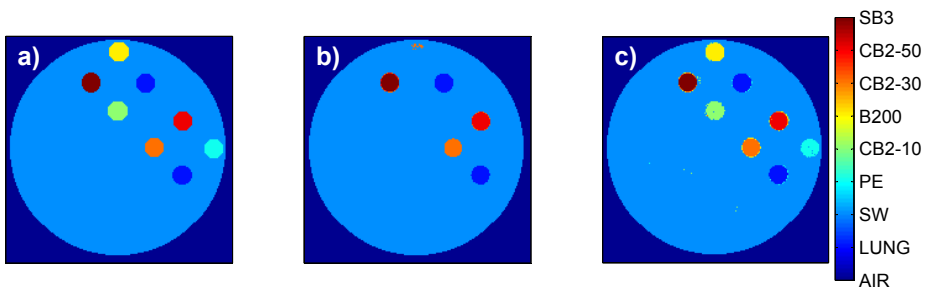

Figure 8-3.8: Material segmentation for electron and orthovoltage photon beam dose calculations: the exact geometry (a), the single-energy CT material segmentation (b) and the dual-energy CT material segmentation (c).

-4% and +3%, respectively. The dual-energy CT material extraction results in dose calculation errors below 1% in all cylinders, except for some voxels at the edge of the cylinders.

For the 18 MeV dose calculations, the dose differences from the exact geometry are shown in figure 8-3.9e and 8-3.9f. The incorrectly assigned polyethylene insert shows errors up to 6%. This corresponds to the difference in the mass collision stopping power $(S/\rho)_{\text{col}}$ between polyethylene and solid water.

A small change in the mass density of the medium with which electrons interact causes a small change in the electron range. This might result in relatively large dose calculation errors in the high dose gradient area in the proximity of the electron range. A small underestimation of the density of solid water in both single and dual-energy CT geometries is reflected by the blue areas that are more pronounced and accounting for -5% dose calculation errors in the single-energy CT geometry. Moreover, the incorrect assignment of the polyethylene insert also causes different attenuation within the insert itself resulting in a larger range of the electrons in the

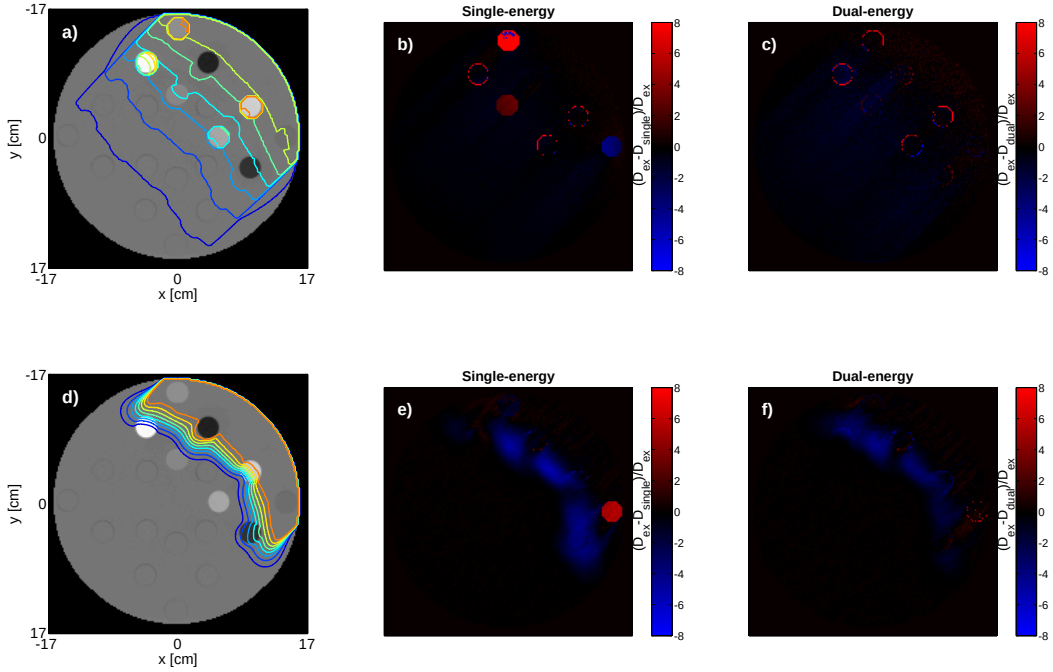

Figure 8-3.9: Dose distributions in the exact geometry for a single 250 kVp photon beam (a) and for a single 18 MeV electron beam (d). The dose calculation errors in the single-energy CT geometry (b,e) and the dual-energy CT geometry (c,f) for a single 250 kVp photon beam and a single 18 MeV electron beam, respectively. Dose differences are defined as $(D_{\mathrm{ex}} - D_{\mathrm{single\ or\ dual}})/D_{\mathrm{ex}}$.

single-energy CT geometry. The effect causes dose calculation errors downstream of the polyethylene insert which is also represented by the blue area.

8.3.5 Dose calculations for 18 MV and 6 MV photon beams

The exact material segmentation, the single-energy CT and dual-energy CT material segmentation for phantom C are shown in figure 8-3.10a-c. Similarly to the MV photon beam phantom, three cylinders could not be assigned correctly using the single-energy CT approach. The dual-energy CT material assignment reproduces the exact geometry well.

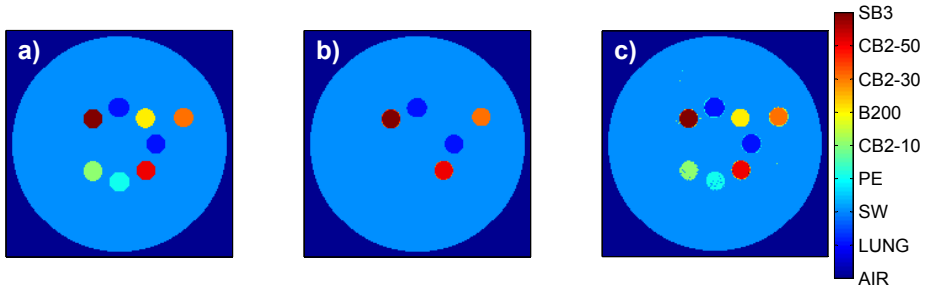

Figure 8-3.10: Material segmentation for MV photon beam dose calculations: the exact geometry (a), the single-energy CT material segmentation (b) and the dual-energy CT material segmentation (c).

Dose calculations were performed for two parallel-opposed 18 MV photon beams. The exact dose distribution is presented in figure 8-3.11a. The dose differences from the exact geometry for the single-energy CT material segmentation and the dual-energy CT material segmentation are shown in figure 8-3.11b and 8-3.11c, respectively. As can be seen, there is up to 3% dose difference in the mis-assigned polyethylene cylinder. This is due to the fact that (μ_{en}/ρ) of polyethylene is 3% higher than that of solid water. Similar results were obtained for a two parallel-opposed 6 MV photon beam arrangement (results not shown). The dose calculation errors in the dual-energy CT geometry are below 1% in all inserts with the exception of a few incorrectly assigned voxels in the polyethylene cylinder which are due to up to 10% errors in Z extraction of some voxels.

8.4 Discussion

Dual-energy material segmentation for human tissues

The importance of material assignment for MC dose calculations was demonstrated on a set of tissue-equivalent materials. However, the RMI tissue-equivalent

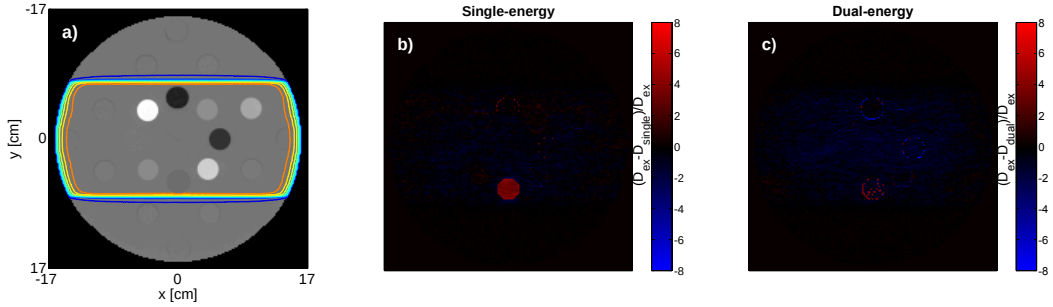

Figure 8-3.11: Dose distributions in the exact geometry for two parallel-opposed 18 MV beams (a). The dose calculation errors in the single-energy CT geometry (b) and the dual-energy CT geometry (c).

materials mimicking human tissues well in CT imaging do not necessarily have the dosimetric properties of human tissues in megavoltage photon beams or electron beams. A theoretical evaluation of the importance of material assignment for human tissues is demonstrated here. Since the largest dose calculation errors due to mis-assignment of media were observed for a 250 kVp photon beam, the emphasis of this study is put on kilovoltage photon beams.

Mass energy absorption coefficients for 34 ICRU-44 [20] tissues (table 8-4.4) were calculated for a 250 kVp photon beam with the EGSnrc/G user code [1] and plotted as a function of Z and ρ_e (figure 8-4.12). Then an assumption about the ability of the material segmentation algorithm to distinguish two similar tissues in Z and ρ_e-maps was made. Following the experimental results, we assumed that two materials can be well differentiated when they differ by 0.05 and 0.5 in ρ_e and Z, respectively.

Figure 8-4.12a refers to the single-energy segmentation procedure and demonstrates that under such circumstances, the difference in (μ_{en}/ρ) between sacrum and

Table 8-4.4: ρ, ρ_e and Z of 34 ICRU-44 tissues used for analysis of dose calculation errors due to mis-assignment of media.

medium	ρ g/cm^3	ρ_e	Z	medium	ρ g/cm^3	ρ_e	Z
adipose	0.950	0.951	6.670	skeleton-cartilage	1.100	1.083	8.329
blood	1.060	1.050	7.825	skeleton-cortical bone	1.920	1.781	13.978
brain	1.040	1.035	7.878	skeleton-cranium	1.610	1.517	13.129
breast	1.020	1.014	7.271	skeleton-femur	1.330	1.278	12.087
cell nucleus	1.000	0.994	8.167	skeleton-humerus	1.460	1.389	12.612
eye lens	1.070	1.055	7.541	skeleton-mandible	1.680	1.577	13.332
GI tract	1.030	1.024	7.710	skeleton-red marrow	1.030	1.023	7.266
heart	1.060	1.051	7.806	skeleton-ribs (2,6)	1.410	1.347	12.224
kidney	1.050	1.041	7.840	skeleton-ribs (10)	1.520	1.441	12.760
liver	1.060	1.050	7.866	skeleton-sacrum	1.290	1.244	11.407
lung (defl.)	1.050	1.041	7.879	skeleton-spongiosa	1.180	1.150	10.678
lung (infl.)	0.260	0.258	7.879	skeleton-vert. column$_{(C4)}$	1.420	1.356	12.271
lymph	1.030	1.026	7.837	skeleton-vert. column$_{(D6,\ L3)}$	1.330	1.278	11.742
muscle	1.050	1.040	7.848	skeleton-yellow marrow	0.980	0.982	6.559
ovary	1.050	1.043	7.843	spleen	1.060	1.051	7.872
pancreas	1.040	1.034	7.699	testis	1.040	1.034	7.816
skin	1.090	1.078	7.627	thyroid	1.050	1.041	7.710

femur is 4.2% indicating that dose calculation errors arising from inaccurate tissue segmentation can be as high as 4.2% between sacrum and femur. However, these two tissue types have significantly different Z and therefore can be distinguished in the Z-map employed in the dual-energy segmentation (see figure 8-4.12b). The maximum difference in (μ_{en}/ρ) in the Z plot between two materials that cannot be separated by their differences in ρ_{e} nor in Z is 1.8% between brain and eye lens tissue. This will directly translate into dose calculation errors for the 250 kVp beam and is therefore a limitation of the dual-energy approach to material segmentation.

(μ_{en}/ρ) calculations for an 18 MV beam showed only a small improvement in (μ_{en}/ρ) differences of indistinguishable tissues when the dual-energy CT material segmentation was used, accounting for a 0.3% improvement. This indicates a small

benefit of the dual-energy material segmentation for patient MC dose calculations with high energy photon beams.

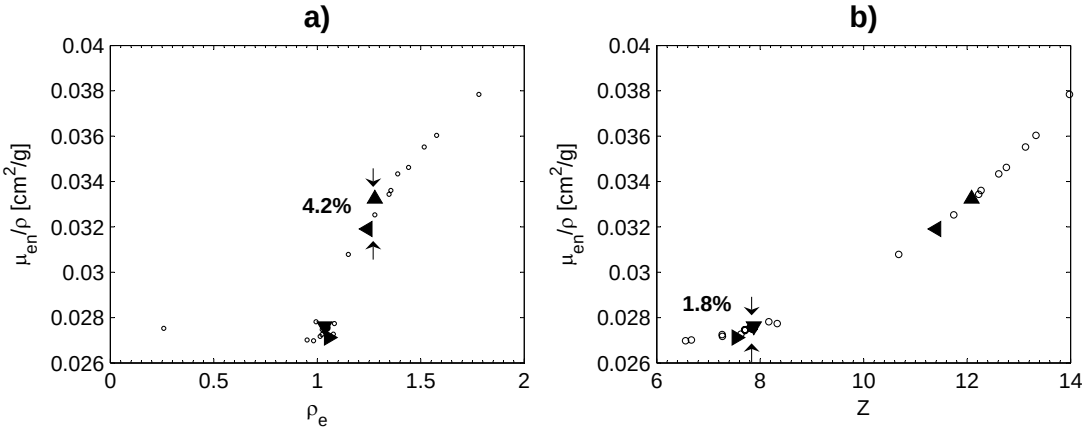

Figure 8-4.12: Mass energy absorption coefficient μ_{en}/ρ versus ρ_{e} (a) and Z (b) for 34 ICRU tissues and a 250 kVp photon beam. Brain (▼), eye lens (►), femur (▲) and sacrum (◄) tissue points are emphasized.

Stopping power ratios material-to-air were calculated for an 18 MeV electron beam using the EGSnrc/SPRRZnrc code [21]. A small improvement in stopping power ratios of indistinguishable tissues was found indicating a small improvement in dose calculation accuracy when the dual-energy tissue segmentation is used. However, an incorrect media assignment for electron beam dose calculations can lead to shifts in electron ranges and can consequently result in high dose calculation errors in dose gradient regions.

This study shows that dual-energy material assignment for human tissues is of importance mainly for kilovoltage photon beams. The dose calculation errors for treatments using external kilovoltage photon beams can be reduced from up to 4.2% to less than 1.8%. Similar MC dose calculation improvement can be achieved for

assessment of dose from x-ray imaging procedures, including CT scanning and cone beam CT for image-guided radiotherapy. The study could also have implications for dose calculations for isotopes used in low dose rate and high dose rate brachytherapy.

Another interesting application of dual-energy scanning, which needs further investigation, might be the use for automatic segmentation and delineation of anatomical structures.

Practical implementation of dual-energy CT imaging

Dual-energy CT-based material extraction could have limited clinical applications because of the complication of patient movement between the two CT scans which could cause the two different kVp images to mis-align. However, Kalender *et al.* [22] developed a CT scanner with a prototype apparatus for rapid kVp switching. By this means, patient movement artifacts are significantly reduced because the two kVp images are acquired simultaneously.

Another way to acquire images at two different voltages with minimal patient movement artifacts is using a dual source CT system [23, 24]. The CT system consists of two x-ray tubes arranged at 90° and offers an increased temporal resolution and submillimeter spatial resolution. The voltages in the x-ray tubes can be set to significantly different values and the two resulting images can be used for dual-energy material analysis. However, since the system is relatively new, more research on image artifacts, e.g. scatter, is needed [25].

Another issue in CT imaging, especially when dealing with extraction of material properties using dual-energy CT images, is noise [26]. A compromise between the dose delivered to patients during CT scanning and the image quality has to be

found. Johnson *et al.* [27] used dual-energy CT images (acquired on a SOMATOM Definition Dual Source CT, Siemens, Germany) and a three-material decomposition method for differentiation of iodine contrast material in various parts of the human body. The dose delivered to patients in the study was well below the reference maximal dose values which resulted in increased image noise. Therefore, the noise had to be reduced by applying averaging across groups of voxels. This noise reduction technique that worked well in the paper by Johnson *et al.* could also be used for our material extraction algorithm.

Spectral measurements are not a trivial task for a CT x-ray tube. The spectra for dual-energy CT-based material extraction can also be calculated by freely available software, such as the TASMIP code [28]. The appropriate x-ray tube voltage, the anode angle, the x-ray tube inherent and added filtration as specified by the manufacturer have to be input in the program. Half value layer (HVL) measurements done during the CT scanner quality assurance can be compared to HVLs calculated from the TASMIP spectra. A more accurate total filtration can be found by matching the HVL values.

8.5 Conclusions

Dual-energy CT material extraction based on parameterization of the linear attenuation coefficient using 100 kVp and 140 kVp CT images and corresponding x-ray spectra was presented. The material extraction was carried out for 17 tissue-equivalent materials with a wide range of relative electron densities ρ_e and effective atomic numbers Z. The mean errors on the extraction of ρ_e and Z are 1.8% and 2.8%, respectively. The results were encouraging and therefore the dual-energy CT

material extraction was used for an improved (HU; ρ, Z) tissue segmentation for Monte Carlo dose calculations.

Dose calculations were performed for 250 kVp, 6 MV and 18 MV photon beams and an 18 MeV electron beam using a solid water phantom with tissue-equivalent inserts in the EGSnrc/DOSXYZnrc code. A single CT image and a calibration curve were used for the conventional (HU; ρ) single-energy CT material segmentation. The novel (HU; ρ, Z) dual-energy CT material extraction was done on the basis of the extracted Z and ρ_e-maps of the phantom.

It was shown that some of the tissue-equivalent inserts could not be differentiated from the surrounding solid water due to their low contrast in the CT image when using the conventional material segmentation. This resulted in dose calculation errors that were particularly large for the 250 kVp beam, accounting for up to 17% in the mis-assigned soft bone tissue-equivalent cylinder. The dose calculation errors in the 18 MeV electron beam and the 18 MV photon beam were 6% and 3% in the mis-assigned polyethylene insert. All inserts were assigned correctly when the dual-energy material extraction was done due to the large contrast in the Z-map. As a result, the dose was calculated accurately within 1% when the dual-energy CT material assignment was used.

A theoretical study on the difference of mass energy absorption coefficients and stopping powers of human tissues for the 250 kVp and 18 MV photon beams and 18 MeV electron beam showed that the dual-energy material segmentation is mainly required for kilovoltage photon beams where the dose calculation error due to mis-assignment of media can be reduced from 4.2% to less than 1.8%. The dual-energy

material assignment should be preferred over the conventional single-energy CT material assignment to decrease dose calculation errors when calculating the dose delivered during kilovoltage radiotherapy, brachytherapy and x-ray imaging procedures such as in CT imaging and cone beam image-guided radiotherapy.

This chapter showed that dual-energy CT material extraction based on parameterization of the linear attenuation coefficient using images acquired on a clinical CT scanner is feasible. Hard x-ray beams have to be used for scanning. Effective atomic numbers (Z) and relative electron densities (ρ_{e}) for a set of tissue-equivalent materials following the Z and ρ_{e} ranges of human tissues were extracted with a reasonable accuracy. Therefore, DECT and the novel material segmentation were applied to images of a tissue-equivalent phantom. It was demonstrated that MC dose calculations are significantly improved for kilovoltage photon beams and megavoltage electron beams due to a more accurate tissue segmentation. Soft bone tissue-equivalent materials exhibited large dose calculation errors due to material mis-assignment. For megavoltage photon beams, MC dose was calculated relatively accurately, with dose calculation errors less than 3%, using the conventional tissue segmentation with single-energy CT images.

The chapter concluded with a theoretical study showing the improvement of the DECT material segmentation for human tissues. MC dose calculations are expected to be more accurate for human tissues in kilovoltage photon beams if the novel tissue segmentation is applied. Brachytherapy dose calculations with radiation sources in

the kV energy range might therefore also be affected by incorrect tissue segmentation. Practical issues of DECT in a clinical setting were briefly discussed and together with brachytherapy dose calculations are the subject of the next chapter.

REFERENCES

[1] I. Kawrakow and D.W.O. Rogers. The EGSnrc Code System: Monte Carlo simulation of electron and photon transport. *NRCC Report PIRS-701*, 2006.

[2] B.R.B. Walters and D.W.O. Rogers. DOSXYZnrc Users Manual. *NRCC Report No. PIRS 794 rev B*, 2007.

[3] F. Verhaegen and S. Devic. Sensitivity study for CT image use in Monte Carlo treatment planning. *Phys. Med. Biol.*, 50:937–946, 2005.

[4] U. Schneider, E. Pedroni, and A. Lomax. The calibration of CT Hounsfield units for radiotherapy treatment planning. *Phys. Med. Biol.*, 41:111–124, 1996.

[5] W. Schneider, T. Bortfeld, and W. Schlegel. Correlation between CT numbers and tissue parameters needed for Monte Carlo simulations of clinical dose distributions. *Phys. Med. Biol.*, 45:459–78, 2000.

[6] B. Vanderstraeten, P.W. Chin, M. Fix, A. Leal, G. Mora, N. Reynaert, J. Seco, M. Soukup, E. Spezi, W. De Neve, et al. Conversion of CT numbers into tissue parameters for Monte Carlo dose calculations: a multi-centre study. *Phys. Med. Biol.*, 52:539–562, 2007.

[7] F.C.P. du Plessis, C.A. Willemse, M.G. Lötter, and L. Goedhals. The indirect use of CT numbers to establish material properties needed for Monte Carlo calculation of dose distributions in patients. *Med. Phys.*, 25:1195–1201, 1998.

[8] J.V. Siebers, P.J. Keall, J.O. Kim, and R. Mohan. Performance benchmarks of the MCV Monte Carlo system. *XIII International Conference on the Use of Computers in Radiation Therapy, Heidelberg, Germany*, pages 129–131, 2000.

[9] I. Kawrakow. VMC++, electron and photon Monte Carlo calculations optimized for Radiation Treatment Planning. *Advanced Monte Carlo for Radiation Physics, Particle Transport Simulation and Applications: Proceedings of the Monte Carlo 2000 Meeting Lisbon*, pages 229–236, 2001.

[10] H.E. Johns and J.R. Cunningham. *The physics of radiology*, pages 241–3. Springfield, Illinois, fourth edition, 1983.

[11] R.A. Rutherford, B.R. Pullan, and I. Isherwood. Measurement of Effective Atomic Number and Electron Density Using an EMI Scanner. *Neuroradiology*, 11:15–21, 1976.

[12] B.J. Heismann, J. Leppert, and K. Stierstorfer. Density and atomic number measurements with spectral x-ray attenuation method. *J. Appl. Phys.*, 94:2073–2079, 2003.

[13] C. Rizescu, C. Beşliu, and A. Jipa. Determination of local density and effective atomic number by the dual-energy computerized tomography method with the ^{192}Ir radioisotope. *Nucl. Instrum. Meth. A*, 465:584–599, 2001.

[14] M. Torikoshi, T. Tsunoo, M. Sasaki, M. Endo, Y. Noda, Y. Ohno, T. Kohno, K. Hyodo, K. Uesugi, and N. Yagi. Electron density measurement with dual-energy x-ray CT using synchrotron radiation. *Phys. Med. Biol.*, 48:673–685, 2003.

[15] T. Tsunoo, M. Torikoshi, Y. Ohno, M. Endo, M. Natsuhori, T. Kakizaki, N. Yamada, N. Ho, N. Yagi, and K. Uesugi. Measurement of electron density and effective atomic number using dual-energy X-ray CT. *Nuclear Science Symposium Conference Record, 2004 IEEE*, 6, 2004.

[16] M.J. Berger, J.H. Hubbell, S.M. Seltzer, J. Chang, J.S. Coursey, R. Sukumar, and D.S. Zucker. XCOM: Photon Cross Section Database (version 1.3). *National Institute of Standards and Technology (NIST), Gaithersburg, MD*, 2005.

[17] M. Bazalova and F. Verhaegen. Monte Carlo simulation of a computed tomography x-ray tube. *Phys. Med. Biol.*, 52:5945–5955, 2007.

[18] D.W.O. Rogers, B.A. Faddegon, G.X. Ding, C.M. Ma, J. Wei, and T.R. Mackie. BEAM: A Monte Carlo code to simulate radiotherapy treatment units. *Med. Phys.*, 22:503–524, 1995.

[19] M. Bazalova, J.F. Carrier, L. Beaulieu, and F. Verhaegen. Tissue segmentation in Monte Carlo treatment planning: A simulation study using dual-energy CT images. *Radioth. Oncol.*, 86:93–98, 2008.

[20] ICRU Report No. 44. *Tissue Substitutes in Radiation Dosimetry and Measurement*. ICRU, Bethesda, MD, 1989.

[21] D.W.O. Rogers, I. Kawrakow, J.P. Seuntjens, and B.R.B. Walters. NRC User Codes for EGSnrc. *NRCC Report PIRS-702 rev B*, 2005.

[22] W.A. Kalender, W.H. Perman, J.R. Vetter, and E. Klotz. Evaluation of a prototype dual-energy computed tomographic apparatus. I. Phantom studies. *Med. Phys.*, 13:334–339, 1986.

[23] T.G. Flohr. First performance evaluation of a dual-source CT (DCST) system. *Eur. Radiol.*, 16:256–68, 2006.

[24] W.A. Kalender. *Computer Tomography*. New York: Wiley, 2 edition, 2005.

[25] Y. Kyriakou and W.A. Kalender. Intensity distribution and impact of scatter for dual-source CT. *Phys. Med. Biol.*, 52:6969–6989, 2007.

[26] F. Kelcz, P.M. Joseph, and S.K. Hilal. Noise considerations in dual energy CT scanning. *Med. Phys.*, 6:418–425, 1979.

[27] T.R.C. Johnson, B. Krauß, M. Sedlmair, M. Grasruck, H. Bruder, D. Morhard, C. Fink, S. Weckbach, M. Lenhard, B. Schmidt, T. Flohr, M.F. Reiser, and C.R. Becker. Material differentiation by dual energy CT: initial experience. *Eur. Radiol.*, 17:1510–1517, 2007.

[28] J.M. Boone and J.A. Seibert. An accurate method for computer-generating tungsten anode x-ray spectra from 30 to 140 kV. *Med. Phys.*, 24:1661–1670, 1997.

CHAPTER 9
Practical aspects of dual-energy CT

9.1 Introduction

As demonstrated in chapters 7 and 8, dual-energy CT-based material extraction (DECT) makes tissue segmentation more accurate and significantly improves Monte Carlo (MC) dose calculations for orthovoltage photon beams. For a 250 kVp photon beam using the conventional material segmentation technique, large dose calculation errors, up to 17% for a soft bone tissue-equivalent material were reported.

Orthovoltage beams are produced by x-ray tubes using potentials between 200 and 300 kVp. The mean energy of such beams is approximately 100 keV meaning that the photoelectric effect, strongly dependent on the effective atomic number (Z), is significant compared to megavoltage (MV) photon beams. Therefore, orthovoltage photon beam dose calculations require a more careful tissue segmentation than MV photon beams. Dose miscalculations due to tissue mis-assignment are expected to be even more pronounced for low dose rate (LDR) brachytherapy where the mean energy of photons is in tens of keV.

In this chapter, DECT is applied to images of a phantom with brachytherapy seeds and MC dose calculations with ^{125}I are performed. Later on and for the first time in the thesis, DECT is tested in vivo. The feasibility of DECT for real tissues is investigated in a canine subject. Then a patient study is presented that raised the issues of patient motion and image noise propagation in DECT. MC dose calculations

for the LDR brachytherapy prostate patient using DECT mass density assignment are performed.

Patient motion between the two consecutive DECT scans can compromise the accuracy of DECT material segmentation. Ideally for DECT, dual-source CT scanners [1, 2] or x-ray tubes with rapid kV switching [3] should be used. Most clinics currently use single-source CT scanners with x-ray tubes without the option for rapid kV switching. In the last section of the chapter, a new scanning method for patient motion reduction for DECT using a single tube voltage and a rotating filter is proposed. As a first step, MC simulations of a stationary setup are presented.

9.2 Materials and methods

9.2.1 Material extraction of an RMI phantom

A single-slice ACQSim CT scanner (Philips, Eindhoven, The Netherlands) was used for DECT for the first time in the thesis and therefore DECT material extraction was tested with 17 tissue equivalent materials (table 8-2.1) in an RMI solid water phantom (figure 8-2.3) using 100 and 140 kVp scans. DECT material extraction based on a parameterization of the linear attenuation coefficient was applied to the two CT scans using an in-house Matlab (The Mathworks, Natick, MA) routine presented in section 8.2.2. The spectra needed for the material extraction were calculated analytically using the TASMIP code [4] according to manufacturer's specification of the CT x-ray tube. Beam hardening in the 32 cm diameter phantom and in high density materials was taken into account (see section 8.2.2).

Subsequently, the mass density maps of the phantom were produced using two approaches: the conventional approach with a calibration curve (ρ_{single}) and the

DECT approach (ρ_{dual}). The calibration curve was created on the basis of the measured 100 kVp CT numbers and the known ρ of the RMI inserts. The DECT ρ_{dual}-map was produced from the DECT ρ_{e}-map and a linear relationship between ρ_{e} and ρ obtained from table 8-2.1.

9.2.2 Material extraction of a canine subject

The pelvis of an anesthetized canine subject was scanned at 100 and 140 kVp on the ACQSim CT using 300 mAs. ρ_{e} and Z-maps were extracted from the CT images by the procedure previously described and used on the phantom. ρ-maps were then produced by the conventional single-energy CT approach (ρ_{single}) using a calibration curve and the DECT approach (ρ_{dual}).

9.2.3 Reduction of streaking artifacts caused by brachytherapy seeds and their effect on Monte Carlo dose calculations: a phantom study

An ultrasound prostate phantom (CIRS, Norfolk, VI, figure 9-2.1) with 45 dummy brachytherapy seeds was scanned in the ACQSim CT scanner at 100 and 140 kVp with 400 mAs. For DECT, the images were resampled from $(0.5\times0.5\times3)\,\text{mm}^3$ to $(1.0\times1.0\times3)\,\text{mm}^3$. ρ_{single} and ρ_{dual}-maps of the entire phantom were derived.

Both sets of images suffer from metal streaking artifacts caused by the presence of the seeds. As noticed in chapter 8, streaking artifacts between two high-Z tissue-equivalent materials were reduced in the ρ_{dual}-map. The effect of DECT on metal streaking artifacts caused by brachytherapy seeds was examined in this study.

Brachytherapy Monte Carlo dose calculations for the implanted phantom were performed using the MCNPX code [5], version 2.5.0. The dummy seeds were considered as the 6711 model ^{125}I seeds and their positions were determined on the basis of the 140 kVp CT images. The 45 iodine seeds were modeled using a phase-space file

Figure 9-2.1: Ultrasound phantom with brachytherapy seeds.

scored on a sphere around the seeds, as described in the paper by Furstoss *et al.* [6]. In all MC simulations, the interseed attenuation effect was therefore included.

Both ρ_{single} and ρ_{dual}-maps were discretized, as required by the MCNPX code, to the bin size of $0.1\,\text{g/cm}^3$. A human tissue-like segmentation scheme was used for material assignment, as listed in table 9-2.1. The phantom was segmented into air and soft tissue and adipose tissue of different mass densities. By this means, the effects of tissue mis-assignment due to streaking artifacts for permanent implant brachytherapy patients was studied.

Table 9-2.1: ρ-ranges for material segmentation for phantom MC dose calculations.

ρ-range [g/cm^3]	assigned as ρ [g/cm^3]	material
<0.65	0.001	air
$[0.65 : 0.75]$	0.7	adipose
$[0.75 : 0.85]$	0.8	adipose
$[0.85 : 0.95]$	0.9	soft tissue
$[0.95 : 1.05]$	1.0	soft tissue
$[1.05 : 1.15]$	1.1	soft tissue
>1.15	1.2	PMMA

9.2.4 Reduction of streaking artifacts caused by brachytherapy seeds and their effect on Monte Carlo dose calculations: a patient study

CT images of four prostate patient with permanent ^{125}I brachytherapy seeds were acquired at 90 and 140 kVp on a Brilliance Big Bore scanner (Philips, Eindhoven, The Netherlands). Since the two scans were not taken simultaneously, minor patient motion occurred for three out of the four patients. Therefore, DECT could directly be performed on one prostate patient. The DECT algorithm on the Brilliance scanner was also tested with the RMI phantom.

Due to the noise in the patient scans, especially in the 90 kVp images, the CT images were resampled from 512×512 matrices with a voxel size of $(0.35\times0.35\times2)\,\mathrm{mm}^3$ to 128×128 matrices with a voxel size of $(1.4\times1.4\times2)\,\mathrm{mm}^3$. The DECT extraction was applied to the 90 kVp and 140 kVp images which, after a ρ_e to ρ conversion, resulted in dual-energy CT mass density maps of the patient, ρ_{dual}. The single-energy CT density maps, ρ_{single}, were calculated on the basis of a calibration curve created with the RMI phantom and the 90 kVp scan.

The dose distributions D_{single} and D_{dual} based on the seed locations and the patient ρ_{single} and ρ_{dual}-maps, respectively, were calculated with the MCNPX code. Similarly to the phantom dose calculations, the 6711 model was used for the patient MC dose calculations. Absolute dose values were calculated using the actual air kerma strength of the seeds on the day of implantation, as described in the paper by Furstoss *et al.* [6]. Tissues were segmented on the basis of ρ_{single} and ρ_{dual}-ranges listed in table 9-2.2.

Table 9-2.2: ρ-ranges for tissue segmentation for prostate patient MC dose calculations.

ρ-range [g/cm^3]	assigned as ρ [g/cm^3]	tissue type
<0.65	0.001	air
[0.65 : 0.75]	0.7	adipose
[0.75 : 0.85]	0.8	adipose
[0.85 : 0.95]	0.9	soft tissue
[0.95 : 1.05]	1.0	soft tissue
[1.05 : 1.15]	1.1	soft tissue
[1.15 : 1.25]	1.2	soft bone
[1.25 : 1.35]	1.3	soft bone
[1.35 : 1.45]	1.4	bone
[1.45 : 1.55]	1.5	bone
[1.55 : 1.65]	1.6	bone
>1.65	1.7	bone

9.2.5 A new scanning technique with a moving filter: a MC simulation study

Due to the problems of patient motion in the previous study, a new scanning setup for patient motion reduction in DECT is proposed. Our scanning technique is based on keeping the x-ray tube voltage at a certain value (e.g. 140 kV) and a fast insertion and retraction of a filter below the tube as the tube rotates in the gantry. This way, a soft spectrum (without the filter or unfiltered) and a hard spectrum (with the filter) are produced. Depending on the filter material and thickness, the differences in the number of photons reaching the detector ring from the two different spectra will enable to distinguish the signals from the soft and the hard beams. If an optimum frequency of the filter motion is found, two good quality CT images can possibly be reconstructed at a single tube rotation.

Copper was chosen as the filter material and an optimum filter thickness was investigated. Simulations of the ACQSim CT geometry are performed in BEAM [7] and a modified version of the DOSXYZnrc [8] code. For more details about the geometry of the MC simulations, see section 7.2.2.

First, an optimum filter thickness was determined using the SRS-78 analytic program that generates x-ray spectra [9]. A compromise between the mean energy difference of the two spectra and the output of the hard spectrum was found. Then the x-ray beams were modeled by MC and the resulting phase-space files were used for the full CT geometry simulation. CT images of two 13 cm diameter cylindrical solid water phantoms with 10 RMI inserts (phantoms A and B from figure 7-2.2c) were simulated with the filtered and unfiltered x-ray beams. DECT material extraction was applied to the simulated CT images using the MC simulated x-ray spectra.

9.3 Results

9.3.1 Material extraction of an RMI phantom

The results of the ρ_e and Z extraction using the mean value of a region of interest of 17 RMI materials scanned in the ACQSim CT are shown in figure 9-3.2. A good agreement between the calculated and actual ρ_e and Z was found with the mean error on the ρ_e and Z extraction being 1.8% and 3.2%.

The differences in ρ-assignment using the conventional single-energy CT approach and the DECT approach were evaluated. The single-energy CT ρ-map (ρ_{single}) was calculated on a pixel-by-pixel basis using a calibration curve. ρ_e and Z values of the RMI phantom were also extracted on a pixel-by-pixel basis and the ρ_e-map

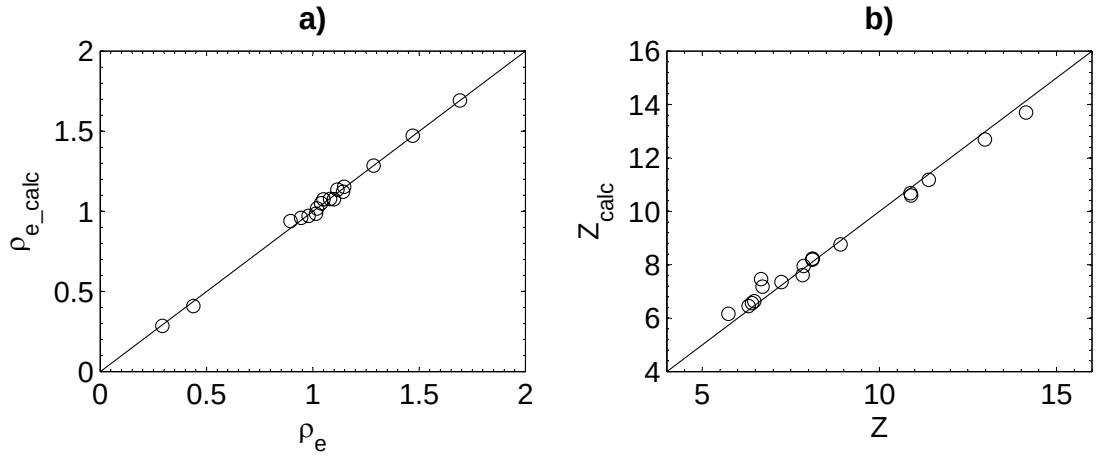

Figure 9-3.2: Calculated $\rho_{\text{e\_calc}}$ and Z_{calc} versus the actual ρ_{e} and Z of 17 RMI materials (a, b).

was converted to a ρ-map using the following relationship: ρ_{dual}=1.079ρ_{e}-0.050. Figure 9-3.3 presents the exact ρ-map (ρ) and the ratios of the exact ρ-map to ρ_{single} and ρ_{dual}.

The ratios $\rho_{\text{single}}/\rho$ and ρ_{dual}/ρ indicate that the ρ for soft bone tissue equivalent materials IB3 and B200 is overestimated using the single-energy approach by 10% and 8%, respectively. The ρ of the polyethylene cylinder is underestimated by 6%. The ρ-assignment accuracy with the DECT method is within 2% with the exception of the low density adipose cylinder where the ρ is overestimated by 4%. The large ρ-assignment errors in IB3 and B200 can be a source of material mis-assignment and MC dose miscalculations, as described in section 8.3.2.

The good results of DECT material extraction on the ACQSim CT were encouraging and therefore, dual-energy material extraction was applied to CT images of a canine subject.

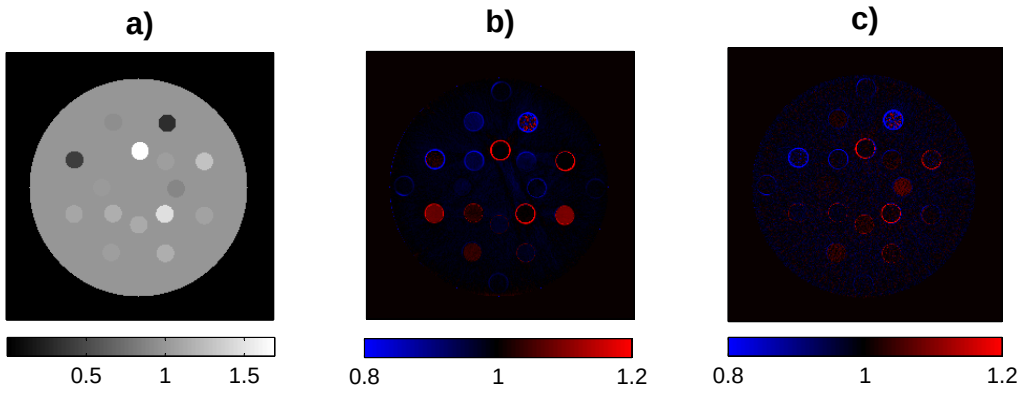

Figure 9-3.3: The exact ρ-map (ρ) of the RMI phantom (a) and the ratios $\rho_{\text{single}}/\rho$ (b) and ρ_{dual}/ρ (c).

9.3.2 Material extraction of a canine subject

CT images of a canine subject were acquired in two subsequent helical scans. Even though the canine was anesthetized, certain object motion occurred between the two subsequent scans, mostly in the intestines. As a result, the material extraction suffers from motion artifacts caused by mis-registration of the 100 and 140 kVp scans. The results from the canine study are summarized in figure 9-3.4.

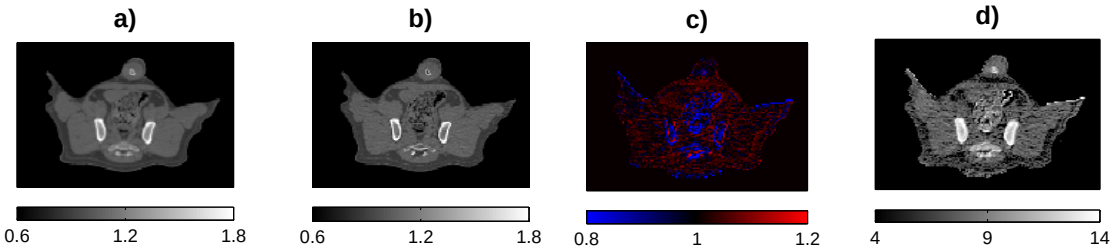

Figure 9-3.4: The ρ-map using the single-energy CT approach (a) and the DECT approach (b) and the ratio $\rho_{\text{dual}}/\rho_{\text{single}}$ for the same slice (c). The extracted Z-map (d).

The DECT assigned ρ_{dual}-map (figure 9-3.4b) is noisier than the ρ_{single}-map (figure 9-3.4a) which is partially due to the noise in the original CT images and partially due to the subject motion between the two scans. Disregarding the motion artifacts in the legs and in the intestines, the ratio of the two maps indicates a density overestimation of inner bone (spongiosa) with the single-energy approach, which is in agreement with the phantom study (figure 9-3.4c). The relatively noisy extracted Z-map is shown in figure 9-3.4d where Z of spongiosa agrees with the published ICRU-44 values [10].

9.3.3 Reduction of streaking artifacts caused by brachytherapy seeds and their effect on Monte Carlo dose calculations: a phantom study

DECT was used for reduction of streaking artifacts caused by brachytherapy seeds in a phantom. The results are summarized in figure 9-3.5. A 90 kVp image of the phantom is presented in figure 9-3.5a with an indicated region of interest (ROI) where the artifacts are the most pronounced. ρ_{single}-map created by the single-energy CT approach is displayed in figure 9-3.5b and the DECT ρ_{dual}-map is shown in figure 9-3.5c. A visual comparison of the artifact reduction makes it clear that the streaking artifacts are significantly reduced when the DECT material extraction is used. In the Z-map (figure 9-3.5d), however, the streaking artifacts are magnified. Also note, that the ρ_{dual}-map is noisier than the ρ_{single}-map which is directly related to the nature of the DECT material extraction.

Figure 9-3.5c demonstrates that in the presence of streaking artifacts, Z-maps cannot be used for material segmentation. However, ρ-assignment can be done on the basis of the ρ_{dual}-maps where reduction of seed artifacts is expected. Consequently, a

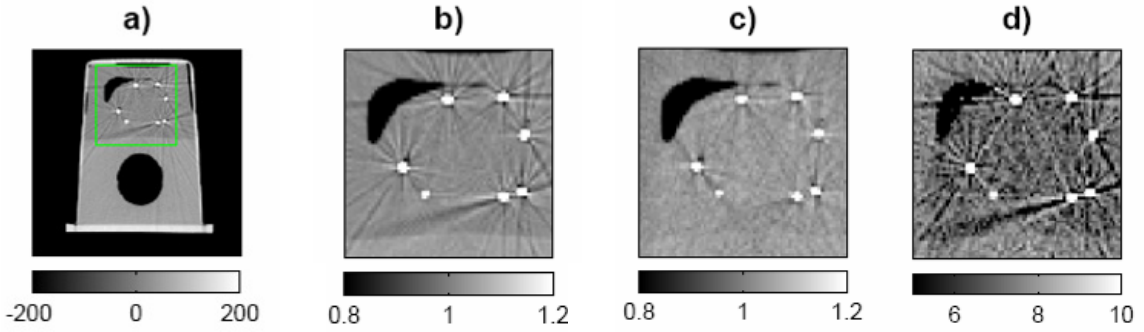

Figure 9-3.5: 100 kVp CT image of the phantom with a marked ROI for DECT (a), the single-energy CT ρ_{single}-map (b) and the DECT ρ_{dual}-map (c). The extracted Z-map of the ROI (d).

more accurate material segmentation based on ρ differences could be expected. With reduced artifacts, prostate contouring by the physician is also expected to be easier.

The results of CT and DECT tissue segmentation of the prostate phantom with brachytherapy seeds are presented in figure 9-3.6a and 9-3.6b, respectively. Due to the streaking artifacts caused by the seeds, some of the soft tissue voxels are mis-assigned to adipose tissue when single-energy CT is used. However, using DECT, fewer voxels are incorrectly assigned, as illustrated in figure 9-3.6b.

Tissue assignment plays an important role for MC dose calculations with low energy photons, as explained earlier. ^{125}I MC dose distributions based on single-energy CT and DECT, D_{single} and D_{dual}, are presented in figure 9-3.6c. The D_{single} isodose lines agree with the D_{dual} isodose lines well with the exception of a number of segments affected by the streaking artifacts. Figure 9-3.6d represents the $D_{\text{single}}/D_{\text{dual}}$ ratio calculated on a pixel-by-pixel basis. The ratio in the incorrectly assigned voxels to adipose is 1.7, indicating that the dose calculation error in these voxels can be

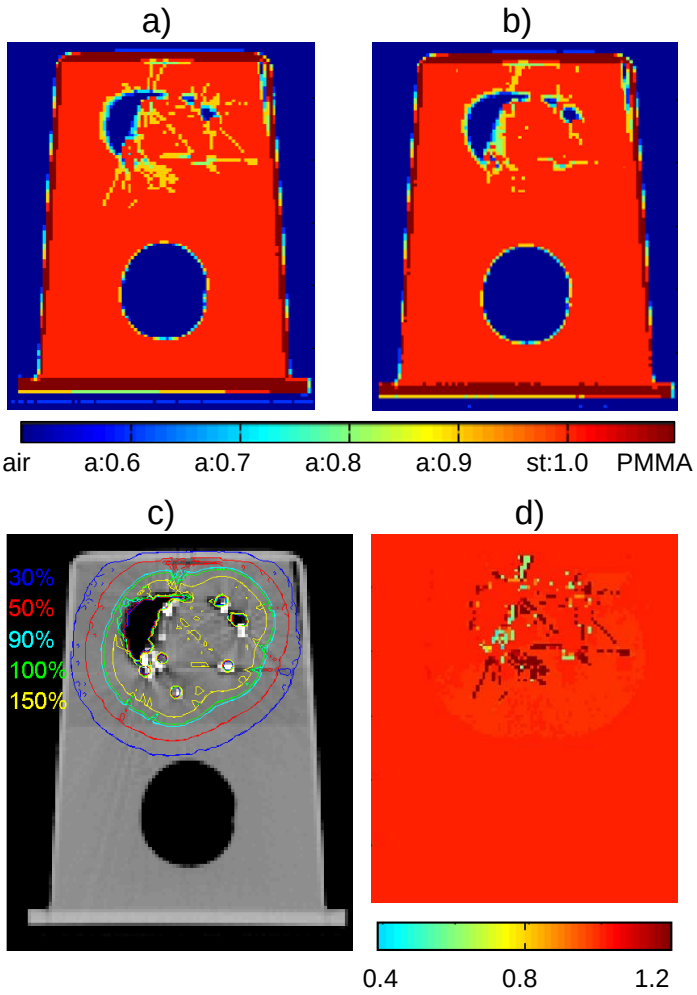

Figure 9-3.6: Material segmentation for MC dose calculations (a:0.6-adipose tissue with 0.6 g/cm^3, st-soft tissue) based on ρ_{single} (a) and ρ_{dual}-maps (b). Comparison of D_{single} (solid line) and D_{dual} (dashed line) dose distributions (c) and the $D_{\text{single}}/D_{\text{dual}}$ ratio (d).

as high as 70%. This is in the agreement with the difference in the mass energy absorption coefficient for adipose and soft tissue at 28 keV, the mean energy of ^{125}I.

The dosimetric relevance of DECT on MC dose calculations could not be studied reliably, because the arrangement of the brachytherapy seeds in the prostate phantom is not necessarily realistic. Therefore, DECT was also applied to CT images of permanent implant prostate patients and the effect of DECT streaking artifact reduction on dosimetric parameters was investigated.

9.3.4 Reduction of streaking artifacts caused by brachytherapy seeds and their effect on Monte Carlo dose calculations: a patient study

The DECT material extraction results from the patient study are summarized in figure 9-3.7. In figure 9-3.7a and 9-3.7b, the ρ_{single}-map and ρ_{dual}-map are displayed. Similarly to the prostate phantom study, the metal streaking artifacts due to the brachytherapy seeds are reduced in the ρ_{dual}-map. On the other hand, the ρ_{dual}-map is noisier than the ρ_{single}-map. This is due to the low mAs setting for the 90 kVp scan which was the same as for the 140 kVp scan. The lower voltage of the x-ray tube causes a lower photon output which results in significantly higher noise in the 90 kVp images (18 HU) than in the 140 kVp images (10 HU). Ideally, for the lower energy scan the mAs setting should be increased in order to obtain two sets of images with similar noise properties.

Figure 9-3.7c displays the $\rho_{\text{dual}}/\rho_{\text{single}}$ ratio. The figure demonstrates that similarly to the canine study, the density of spongiosa (or the inner bone) is overestimated by more than 20% when the single-energy CT approach for density assignment is used. The bone-tissue boundaries appear to be sharper in the ρ_{dual}-map. The motion of the intestines and the reduction of artifacts are also reflected in figure 9-3.7c.

The Z-map is shown in figure 9-3.7d. It is also greatly affected by the noise in the 90 kVp image. In order to extract materials in patient DECT images with a

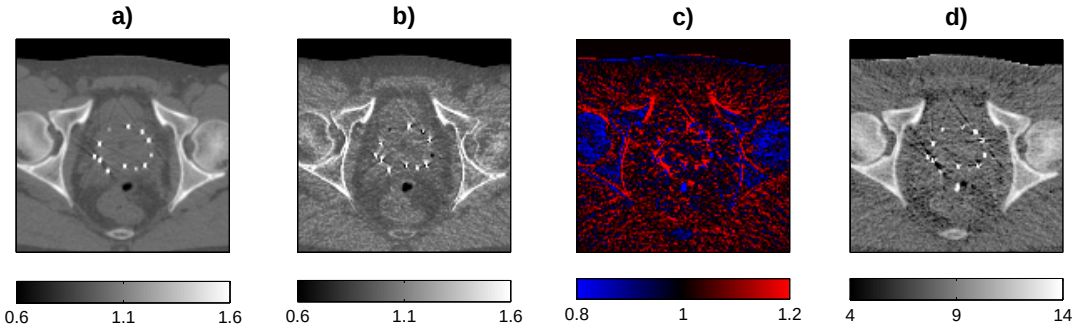

Figure 9-3.7: The patient ρ-map using the single-energy CT approach (a) and the DECT approach (b) and the ratio $\rho_{\text{dual}}/\rho_{\text{single}}$ for the same slice (c). The extracted Z-map (d).

high accuracy, a compromise between patient dose, or the mAs setting and the image quality has to be found.

The ρ_{single} and ρ_{dual}-maps were converted into tissues according to the scheme presented in table 9-2.2 and ^{125}I MC dose calculations with MCNPX were performed. The comparison of D_{single} and D_{dual} dose distributions for two CT slices is shown in figure 9-3.8. Except for the 150% isodose line that encompasses a smaller volume for D_{dual}, a good agreement between D_{single} and D_{dual} was found.

The two dose distributions calculated on the basis of single-energy CT and DECT tissue segmentations were also compared by means of dosimetric parameters D_{90}, D_{50}, V_{150} and V_{100} (table 9-3.3). The largest discrepancy between D_{single} and D_{dual} is found for V_{150} where the difference between the two dose distributions is 3.8%, V_{150} being higher for D_{single}. For this particular patient, the differences between D_{single} and D_{dual} are not significant, however, depending on the seed density and the extent of the streaking artifacts, D_{single} might be affected by tissue mis-assignment.

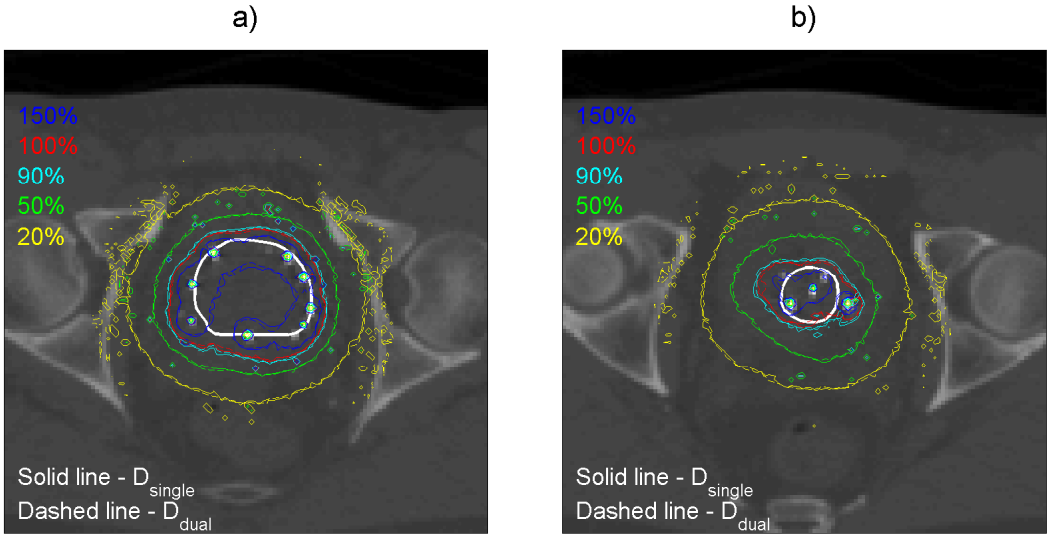

Figure 9-3.8: Comparison of dose distributions D_{single} (solid line) and D_{dual} (dashed line) for two CT slices. 100% isodose line corresponds to 144 Gy prescription dose. The bold white line delineates the PTV.

As demonstrated in the patient study, image noise and patient motion between the two different kVp scans are an important issue in DECT material extraction. CT image noise can be decreased by increasing the number of photons emitted from the x-ray tube. However, higher mAs settings result in higher CT doses and should be avoided. Another possible approach for noise reduction are various denoising techniques. They can be applied directly on CT images [11–13] or using sinograms [14].

Table 9-3.3: Dosimetric parameters and their differences Δ calculated on the basis of D_{single} and D_{dual} dose distributions.

	D_{single}	D_{dual}	$\Delta(\%)$		D_{single}	D_{dual}	$\Delta(\%)$
$D_{90}(\%)$	118.5	115.5	2.6	$V_{150}(\%)$	69.1	66.6	3.8
$D_{50}(\%)$	175.0	168.9	3.6	$V_{100}(\%)$	97.7	97.3	0.4

A solution for patient motion suppression for DECT done on single-source CT scanners is proposed in the next section.

9.3.5 A new scanning technique with a moving filter: a MC simulation study

For the new scanning technique with a moving copper filter, the optimal thickness of copper filtration was first determined using the SRS-78 analytical program. The inherent x-ray tube filtration as given by the manufacturer is 1.5 mm of aluminum. For the 140 kV tube voltage, this results in a beam with 61.2 keV mean photon energy. An additional 2 mm copper filter hardens the beam to 93.0 keV mean photon energy with a nine fold lower output. The 22 keV separation in mean energies is considered to be sufficient for DECT material extraction and the significantly lower output allows to differentiate the signal of the two spectra in the scanner raw data.

The results of chapter 7 suggest that hard beams should be used for DECT material extraction. Note that significant beam hardening occurred only for the low energy beam where the mean energy of an unfiltered 100 kVp beam is approximatively 50 keV. An additional 10 mm Al filter shifts the mean energy of 100 kVp beam to 60 keV, the same mean energy as for the suggested unfiltered 140 kVp beam. Such a beam was already proven to suppress beam hardening effects in DECT and is expected to be suitable for the new scanning technique.

Both 140 kVp x-ray beams were simulated in the BEAM code and used to simulate CT images of the two small phantoms with 10 RMI inserts using a modified version of the EGSnrc/DOSXYZnrc code. DECT extraction was applied to the MC simulated images and the results are presented in figure 9-3.9. The soft spectrum

CT image (without the copper filter) is shown in figure 9-3.9a and the extracted ρ_e and Z are plotted in figure 9-3.9b and figure 9-3.9c, respectively. The mean error of the extraction is 1.8% in ρ_e and 3.6% in Z.

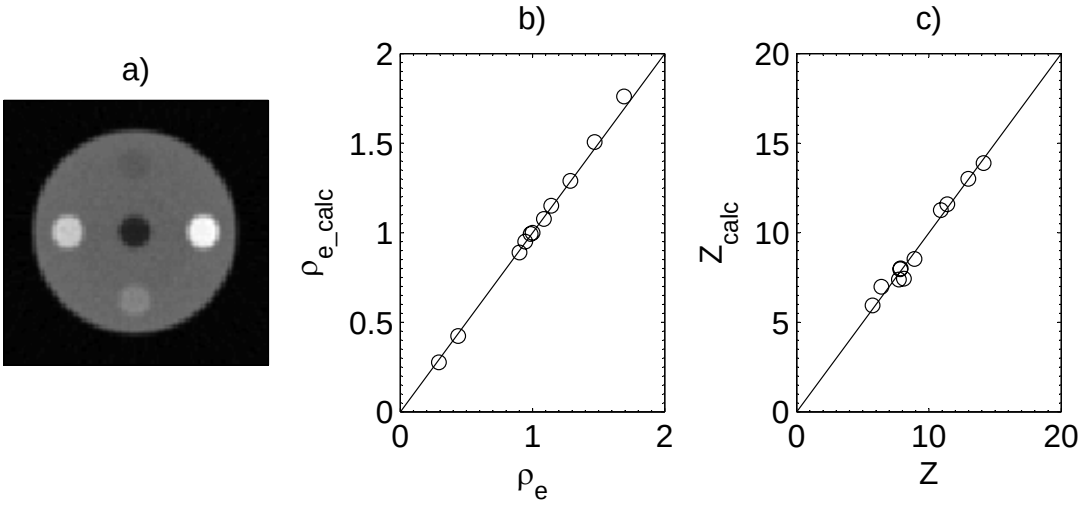

Figure 9-3.9: MC simulated CT image of a phantom with 5 RMI inserts (a), the calculated ρ_{e_calc} and Z_{calc} versus the actual ρ_e and Z (b and c).

By means of MC simulations, it was verified that a 2 mm copper filter is sufficient for DECT material extraction with a 140 kVp beam. It can be therefore concluded that the unfiltered 140 kVp is relatively hard and does not cause significant beam hardening effects in DECT material extraction.

9.4 Conclusions

It has been demonstrated that dual-energy CT-based material extraction can be used for a more accurate density assignment for Monte Carlo dose calculations compared to the conventional technique with single-energy CT images and a calibration

curve. It has been shown that the DECT method works well with animal and human tissues. It has also been demonstrated that dual-energy CT significantly reduces streaking artifacts caused by permanent brachytherapy implants in both phantoms and patients.

Phantom and patient Monte Carlo dose calculations with ^{125}I brachytherapy seeds were performed using single-energy CT and dual-energy CT density assignments. Due to the presence of streaking artifacts caused by the seeds and consequent mis-assignment of soft tissue to adipose, local dose calculation errors up to 70% were reported. However, the fraction of voxel affected by mis-assignment is relatively low and therefore the isodose lines and most of the dosimetric parameters are not significantly affected by the streaking artifacts. This conclusion, however, depends on the extent of streaking artifacts, i.e. the number and the arrangement of the seeds.

With the current standard scanning techniques using single-source CT scanners, patient motion is an important issue for DECT material extraction which was demonstrated in the canine and the patient study. We propose a new scanning method with a single tube voltage and a rotating copper filter. With MC simulations, we have shown that the use of a 2 mm copper filter is feasible for DECT material extraction.

REFERENCES

[1] T.G. Flohr. First performance evaluation of a dual-source CT (DCST) system. *Eur. Radiol.*, 16:256–68, 2006.

[2] W.A. Kalender. *Computer Tomography.* New York: Wiley, 2 edition, 2005.

[3] W.A. Kalender, W.H. Perman, J.R. Vetter, and E. Klotz. Evaluation of a prototype dual-energy computed tomographic apparatus. I. Phantom studies. *Med. Phys.*, 13:334–339, 1986.

[4] J.M. Boone and J.A. Seibert. An accurate method for computer-generating tungsten anode x-ray spectra from 30 to 140 kV. *Med. Phys.*, 24:1661–1670, 1997.

[5] J.F. Briesmeister. MCNP–A General Monte Carlo N-Transport code. *Version 4C, Los Alamos National Laboratory report LA-12625*, 1993.

[6] C. Furstoss, B. Reniers, M.-J. Bertrand, E. Poon, J.-F. Carrier, B. Keller, J.-P. Pignol, L. Beaulieu, and F. Verhaegen. Monte Carlo study of LDR seed dosimetry with an application in a clinical brachytherapy breast implant. *submitted to Med. Phys.*, 2008.

[7] D.W.O. Rogers, B.A. Faddegon, G.X. Ding, C.M. Ma, J. Wei, and T.R. Mackie. BEAM: A Monte Carlo code to simulate radiotherapy treatment units. *Med. Phys.*, 22:503–524, 1995.

[8] B.R.B. Walters and D.W.O. Rogers. DOSXYZnrc Users Manual. *NRCC Report No. PIRS 794 rev B*, 2007.

[9] K. Cranley, B.J. Gilmore, G.W.A. Fogarty, and L. Desponds. IPEM Report 78: Catalogue of Diagnostic X-ray Spectra and Other Data. *York: The Institute of*

Physics and Engineering in Medicine, 1997.

[10] ICRU Report No. 44. *Tissue Substitutes in Radiation Dosimetry and Measurement*. ICRU, Bethesda, MD, 1989.

[11] W.A. Kalender, E. Klotz, and L. Kostaridou. An algorithm for noise suppression in dual energy CT materialdensity images. *IEEE T. Med. Imaging*, 7:218–224, 1988.

[12] P. Sukovic and N.H. Clinthorne. Penalized weighted least-squares image reconstruction for dualenergy X-ray transmission tomography. *IEEE T. Med. Imaging*, 19:1075–1081, 2000.

[13] R.J. Warp and J.T. Dobbins III. Quantitative evaluation of noise reduction strategies in dual-energy imaging. *Med. Phys.*, 30:190–198, 2003.

[14] A. Borsdorf, R. Raupach, and J. Hornegger. Separate CT-reconstruction for 3D wavelet based noise reduction using correlation analysis. *Nuclear Science Symposium Conference Record, 2007. NSS'07. IEEE*, 4, 2007.

CHAPTER 10
Conclusions

10.1 Summary

Radiation therapy planning using Monte Carlo (MC) dose calculations was investigated thoroughly in this thesis. More specifically, the conversion step from patient computed tomography (CT) images into MC geometries was studied extensively and inaccuracies of the conventional conversion scheme were reported.

In chapter 4, the effect of metal streaking artifacts on MC dose calculations was studied. It was found out that in order to calculate MC dose accurately, CT images of patients with hip prostheses or other metallic implants have to be corrected before they are converted into MC geometry files. A MC simulation study showed that scattered photons are a major cause of metal streaking artifacts.

Chapter 5 further developed the topic from chapter 4 by investigation of the magnitude of streaking artifacts caused by real hip prostheses. As a result of this study, patients with bilateral prostheses made of Co-Cr-Mo alloy are expected to show the most severe artifacts and MC dose miscalculations.

A MC model of a CT x-ray tube was presented in chapter 6. The model was validated with the standard half-value layer measurements and with more challenging spectral measurements using a Compton scatter setup. This model of the x-ray tube can further be used for an accurate assessment of patient dose in CT, for scatter and possibly beam hardening corrections in CT and most importantly for dual-energy

CT-based (DECT) material extraction, the topic of the next three chapters of the thesis.

DECT material extraction for improved tissue segmentation in MC dose calculations was first mentioned in chapter 7. A feasibility study for DECT done on a commercial CT scanner was presented by means of MC simulations. It was concluded that in order to minimize beam hardening effects in DECT, especially the lower energy x-ray beam has to be filtered to shift the mean energy of the beam toward higher energies.

Chapter 8 applied the conclusions from the previous chapter in practice. DECT was applied to CT images of a phantom acquired on a single-slice single-source CT scanner. The extracted material properties were used in the novel DECT tissue segmentation scheme resulting in more accurate dose calculations, especially for soft bone tissue-equivalent materials. Expected improvements in MC dose calculations for human tissues were discussed. This novel tissue segmentation technique can play a very important role in dose calculations for the expanding field of proton/hadron therapy.

Reduction of metal streaking artifacts caused by brachytherapy seeds and DECT material extraction in vivo were presented in chapter 9. A phantom study showed that streaking artifacts due to seed implants can be reduced, however, isodose lines were not significantly affected by these artifacts. A patient study revealed the issues of image noise and patient motion during DECT scanning. A novel method for patient motion suppression in DECT on a single-source CT scanner was proposed and investigated by means of MC simulations.

10.2 Future work

This thesis answered many questions regarding the conversion of CT images into MC geometry files. At the same time, however, the research provokes new questions related to CT imaging and Monte Carlo dose calculations. These questions should be the topic of future research.

The conclusions drawn about scatter in the metal artifact study could result in a new artifact reduction algorithm. If scatter is the main contributor to metal artifacts, its removal from sinograms would lead to artifact suppression. For this purpose, the magnitude of scatter and possibly its spatial distribution have to be determined. MC simulations would be the tool of choice.

Future work in DECT should start with employing various noise reduction techniques. Decreasing the noise levels in DECT images will allow for a more accurate material assignment for patient MC dose calculations. Ideally, an automated tissue segmentation technique based on DECT material extraction would be implemented.

Streaking artifact reduction using DECT looks very promising. It should be studied in more detail and the explanation of the results should be found. Taking into account sharper edges in DECT density maps, the possibility of counting brachytherapy seeds when they are clustered should be explored. DECT for metal artifact reduction could also be implemented on metallic objects larger than seed implants.

The canine and patient DECT studies showed that subject motion during the two consecutive scans can severely affect the accuracy of material extraction. In the thesis, a novel DECT scanning technique with a moving copper filter was proposed.

The ideal filter motion frequency to ensure an adequate image quality should be found. A device that holds the 2 mm copper filter enabling fast filter motion could then be carefully mounted on a commercial CT scanner. As a result, it will be possible to apply DECT in routine clinical practice.

List of Abbreviations

2D: Two-dimensional

3D: Three-dimensional

BVM: Basis vector model

CBCT: Cone beam computed tomography

CH: Condensed history

CPU: Central processor unit

CT: Computed tomography

CTDI: Computed tomography dose index

CTV: Clinical target volume

DBS: Directional Bremsstrahlung splitting

DECT: Dual-energy computed tomography

DICOM: Digital Imaging and Communications in Medicine

DVH: Dose volume histogram

EGS: Electron-Gamma-Shower

FBP: Filtered back-projection

FOV: Field of view

GTV: Gross target volume

HP-Ge: High-purity germanium

HU: Hounsfield unit

HVL: Half value layer

ICRU: International Commission on Radiation Units and Measurements

IEC: International Electrotechnical Commission

IMRT: Intensity modulated radiotherapy

kV: Kilovoltage

LDR: Low dose rate

Linac: Linear accelerator

MAR: Metal artifact reduction

MC: Monte Carlo

MCTP: Monte Carlo treatment planning

MDCT: Multi-detector computed tomography

MLC: Multi-leaf collimator

MRI: Magnetic resonance imaging

MV: Megavoltage

NIST: National Institute of Standards and Technology

NTCP: Normal tissue complication probability

OAR: Organ at risk

PC: Personal computer

PDD: Percentage depth dose

PE: Polyethylene

PET: Positron emission tomography

PFM: Parametric fit model

phsp: Phase-space

PTV: Planning target volume

RMI: Radiation Measurements Incorporated

ROI: Region of interest

SPECT: Single photon emission computed tomography

SW: Solid water

TCP: Tumor control probability

TPS: Treatment planning system

US: Ultrasound